Master Thesis

Aerothermal Analysis of Re-usable First Stage during Rocket Retro-propulsion

Franziska Zilker, B. Sc.

January 2018

Adviser:
Tobias Ecker, PhD (DLR)
Prof. Dr.-Ing. Jens von Wolfersdorf (ITLR)

Universität Stuttgart
Institut für Thermodynamik der Luft- und Raumfahrt (ITLR)
Direktor: Prof. Dr.-Ing. habil. Bernhard Weigand

Abstract

Re-usable launch vehicles have a potential to significantly change the launch service market once low refurbishment costs and high reliability are guaranteed. Therefore, DLR conducted a system analysis testing a re-usable launch system capable of bringing 7 t to GTO. One concept is a retro-propulsion decelerated vertical landing vehicle. The idea is to decelerate the returning first stage by providing thrust in the opposite direction of motion. The retro-propulsion maneuver is carried out between 70 and 36 km and covers a Mach number range from 9.5 to 5.1. The thrust is provided by re-igniting three of the nine main engines.

In this study, steady RANS simulations with DLR TAU are conducted at specific points along the retro-propulsion trajectory and for a point during landing. The influence of different flow and engine configurations on the thermal loads are examined. The wall temperature evolution and integral heating over the retro-propulsion maneuver are investigated by coupling a heat flux database with a simple structural model.

The sidewall heat loads are mainly affected by the hot exhaust plume impinging on the surface. The maximum heat loads occur at the impingement area and increase as the first stage descends reaching up to 20 kW/m^2. Over the retro-propulsion maneuver the sidewall temperature rises by about 100 K to a maximum temperature of 400 K depending on the sidewall thickness distribution. This temperature increase is also supported by NASA infrared images of SpaceX Falcon 9 that showed a maximum sidewall temperature of 450 K after the retro-propulsion maneuver. The baseplate heat loads are caused by a "base-impinging plume jet" which results from the interaction shocks of the plumes exhausting from the three active nozzles. The maximum heat load of 70 kW/m^2 is reached at the beginning of the maneuver and decreases with deceasing altitude as the interaction shocks become weaker. The temperature evolution on the baseplate along the SRP trajectory revealed only a minor increase by approximately 20 K depending on the baseplate thickness.

From the results it can be concluded, that during the supersonic retro-propulsion maneuver the heat loads are redistributed compared to the non-propulsive phase before and after. With deactivated engines the heat loads are concentrated around the aft of the first stage. During the retro-propulsion maneuver the baseplate and aft are protected by the plume, which in turn causes higher thermal loads on the upper part. This means that the amount of TPS needed is significantly reduced for the retro-propulsion re-entry.

Zusammenfassung

Wiederverwendbare Trägersysteme könnten den Raumtransportmarkt stark verändern, wenn eine kostengünstige Aufbereitung der Trägersysteme und eine hohe Zuverlässigkeit gewährleistet werden können. Aus diesem Grund führte das DLR eine Systemstudie durch, die ein wiederverwendbares Transportsystem untersucht, das 7 t in den GTO bringen kann. Ein untersuchtes Konzept ist ein senkrecht landendes Fahrzeug, das mit Gegenschub (retro-propulsion, d.h. Schuberzeugung entgegen der Bewegungsrichtung) abgebremst wird. Das Gegenschubmanöver wird in 70 bis 36 km Höhe ausgeführt und bremst das Fahrzeug von M = 9.5 auf 5.1 ab. Der Schub wird durch Wiederzünden von drei der neun Haupttriebwerke erzeugt.

In dieser Arbeit werden stationäre RANS-Simulationen mit DLR TAU an ausgewählten Punkten der Gegenschubtrajektorie und an einem Punkt während des Landeanflugs durchgeführt. Dabei wird der Einfluss verschiedener Strömungs- und Triebwerkskonfigurationen auf die thermischen Lasten untersucht. Die Wandtemperaturentwicklung und die integrale Wärmelast über das Gegenschubmanöver werden ermittelt, indem eine Wärmestromdichtedatenbank mit einem einfachen Strukturmodel gekoppelt wird.

Die Wärmelasten auf die Seitenwand werden hauptsächlich vom Auftreffen der heißen Abgaswolke beeinflusst. Die maximalen Wärmelasten treten an dieser Auftrefffläche auf und steigen mit sinkender Höhe bis zu 20 kW/m^2 an. Die Temperatur an der Seitenwand steigt über das Gegenschubmanöver um 100 K auf eine maximale Wandtemperatur von 400 K an und hängt von der Dickenverteilung der Seitenwand ab. Dieser Anstieg wird von NASA-Infrarotaufnahmen von SpaceX' Falcon 9 bestätigt, die eine maximale Seitenwandtemperatur von 450 K nach dem Gegenschubmanöver zeigen. Die thermischen Lasten der Bodenplatte werden vor allem durch die Stoßwechselwirkungen der Abgasstrahlen der drei aktiven Triebwerke beeinflusst, wodurch ein Teil des Abgases auf die Bodenplatte umgelenkt wird. Die maximale Wärmelast beträgt dadurch 70 kW/m^2 am Anfang des Manövers und nimmt mit sinkender Höhe ab, da die Stoßwechselwirkung der Abgasstrahlen schwächer wird. Die Temperatur auf der Bodenplatte erhöht sich über die Gegenschubtrajektorie um 20 K geringfügig, wobei sie von der Plattendicke abhängt.

Aus den Ergebnissen lässt sich schließen, dass während des Gegenschubmanövers, im Vergleich zu den passiven Flugphasen davor und danach, eine Umverteilung der thermischen Lasten stattfindet. Mit abgeschalteten Triebwerken konzentrieren sich die Wärmelasten auf den unteren Bereich der ersten Stufe. Während des Manövers wird der untere Bereich und v.a. die Bodenplatte durch die Abgaswolke geschützt. Im Gegenzug erhöht die Abgaswolke die thermischen Lasten auf den oberen Bereich der ersten Stufe. Das bedeutet für das Konzept der erste Stufe mit Gegenschubmanöver, dass beim Wiedereintritt nur ein einfaches Thermalschutzsystem benötigt wird.

Contents

List of Figures

List of Tables

List of Symbols

Latin Symbols

b	m	Wall thickness
Bi	$-$	Biot number
c_p	$\mathrm{J/(kg\,K)}$	Heat capacity at constant pressure
c_v	$\mathrm{J/(kg\,K)}$	Heat capacity at volume
C	$-$	Grid cell
C_{T}	$-$	Thrust coefficient
D	m	Diameter
e	$\mathrm{J/kg}$	Total energy per unit mass
E	J	Total energy
g^{+}	depends	Volumetric density of generic flow property
G	depends	Generic flow property
h	m	Altitude
h	$\mathrm{J/kg}$	Enthalpy per unit mass
h	$\mathrm{W/(K\,m^2)}$	Heat transfer coefficent
I	$\mathrm{(kg\,m)/s}$	Momentum
J	depends	Generic diffusive flux
k	$\mathrm{W/(m\ K)}$	Thermal conductivity
k	$\mathrm{J/kg}$	Turbulent kinetic energy
K	m	Domain edge
Kn	$-$	Knudsen number
L	m	Length
m	kg	Mass
M	$-$	Mach number
$\vec{n}$	m	Normal vector
p	$\mathrm{N/m^2}$	Pressure
p_{t}	$\mathrm{N/m^2}$	Total pressure
Pr	$-$	Prandtl number
$\dot{q}$	$\mathrm{W/m^2}$	Heat flux
$\dot{Q}$	W	Heat flow rate

Q	J	Heat
R	$\mathrm{J/(kg\,K)}$	Perfect gas constant
R	m	Radius
Re	$-$	Reynolds number
$s_{i,j}$	$1/\mathrm{s}$	Rate of strain tensor
S	$\mathrm{m^2}$	Surface
t	s	Time
$t_{i,j}$	$\mathrm{kg/(m\,s^2)}$	Favre-averaged Reynolds-stress tensor
T	K	Temperature
T_t	K	Total temperature
u	$\mathrm{J/kg}$	Internal energy per unit mass
u, v, w	$\mathrm{m/s}$	Velocities along x, y and z
$\vec{v}$	$\mathrm{m/s}$	Velocity vector
V	$\mathrm{m^3}$	Volume
w	$-$	Mass fraction
x, y, z	m	Coordinates
$\vec{x}$	m	Location vector

Greek Symbols

α	$^\circ$	Angle of attack
α	$\mathrm{m^2/s}$	Thermal diffusivity
β	$^\circ$	Yaw angle
γ	$-$	Numerical flux
$\delta_{i,j}$	$-$	Kronecker delta
Δ	$-$	Difference
∂	$-$	Domain boundary
∂	$-$	Partial derivative
ϵ	$\mathrm{J/(kg\,s)}$	Rate of dissipation of turbulence energy
ζ	$^\circ$	Circumferential angle
κ	$-$	Heat capacity ratio
λ	m	Mean free path
μ	$\mathrm{kg/(m\,s)}$	Dynamic viscosity
ν	$\mathrm{m^2/s}$	Kinematic viscosity
ϕ	depends	Generic Total flux
ρ	$\mathrm{kg/(m^3)}$	Density
$\tau_{i,j}$	$\mathrm{N/(m^2)}$	Shear stress in i,j plane
ω	$1/\mathrm{s}$	Specific rate of dissipation

Indices

b	Baseplate
c	Centerline

db	Database
e	Exit
esc	Escape
i	Counter
j	Counter
k	Counter
orb	Orbital
rel	Relative
sim	Simulation
sub	Suborbital
sup	Superorbital
t	Turbulent
t	Total condition
w	Sidewall
∞	Ambient conditions

Superscript Indices

$\tilde{}$	Favre average
$\bar{}$	(Reynolds) average
$''$	Favre fluctuations
$'$	Reynolds fluctuations
$\vec{}$	Vector
n	Temporal counter

Acronyms

A	Combustion chamber configuration $T_t = 3900$ K
AUSM	Advection Upstream Splitting Method
B	Combustion chamber configuration $T_t = 3700$ K
CEA	NASA Chemical Equilibrium with Applications
CFD	Computational Fluid Dynamics
DLR	German Aerospace Center
EARSM	Explicit Algebraic Reynolds Stress Mode
NASA	National Aeronautics and Space Administration
NPARC	National Program for Applications-oriented Research in CFD
GTO	Geostationary Transfer Orbit
LH2	Liquid hydrogen
LOx	Liquid oxygen
LU-SGS	Lower-upper Symmetric-Gauss-Seidel Method
MUSCL	Monotonic Upwind Scheme for Conservation Laws
OVERFLOW	NASA CFD code

RANS	Reynolds Averaged Navier Stokes Equation
SGS	Symmetric-Gauss-Seidel Method
SRP	Supersonic Retro-propulsion
SSME	Space Shuttle Main Engine
SST	Shear Stress Transport
TAU	DLR compressible flow solver
THETA	DLR incompressible flow solver
TPS	Thermal Protection System
$1-7$	Trajectory points 1 to 7
8	Landing
7Baoa	Angle of attack at trajectory 7 for configuration B
7Bya	Yaw angle at trajectory 7 for configuration B
7Bnr	Thermal nozzle radiation at trajectory 7 for configuration B
2Bdbv	Database validation at trajectory 2 for configuration B
7Bntp	Nozzle temperature profile at trajectory 7 for configuration B
1Off	Deactivated engines at trajectory 1

Chapter 1

Introduction

This work presents a part of a DLR preliminary design study investigating a retro-propulsion decelerated vehicle similar to SpaceX' Falcon 9. The objective of this thesis is to analyze the heat loads during the re-entry and landing retro-propulsion maneuver. The focus is on examining the effects of the retro-propulsion flow phenomena on the wall heat fluxes.

1.1 What is Retro-Propulsion?

Figure 1.1. SpaceX Falcon 9's first stage during landing retro-boost instants before touch down [1].

Retro-propulsion decelerates a vehicle by providing thrust opposing the vehicle's direction of motion. So far, it has been mostly used on spacecrafts for de-orbit maneuvers (e.g. Space Shuttle Orbiter [2]), to slow the final landing approach (e.g. Viking [3], Mars

Science Laboratory [4]) and to cushion the landing impact (e.g. Soyuz [5]). A very recent application of retro-propulsion is to decelerate the hyper- and supersonic re-entry phase of a space vehicle, known as supersonic retro-propulsion (SRP). Up to date only the privately owned space company SpaceX uses supersonic retro-propulsion to slow down the hypersonic re-entry phase (re-entry burn as they name it) of the returning first stage of their carrier system Falcon 9 (cf. figure 1.2 for the re-entry burn and figure 1.3 for Falcon 9).

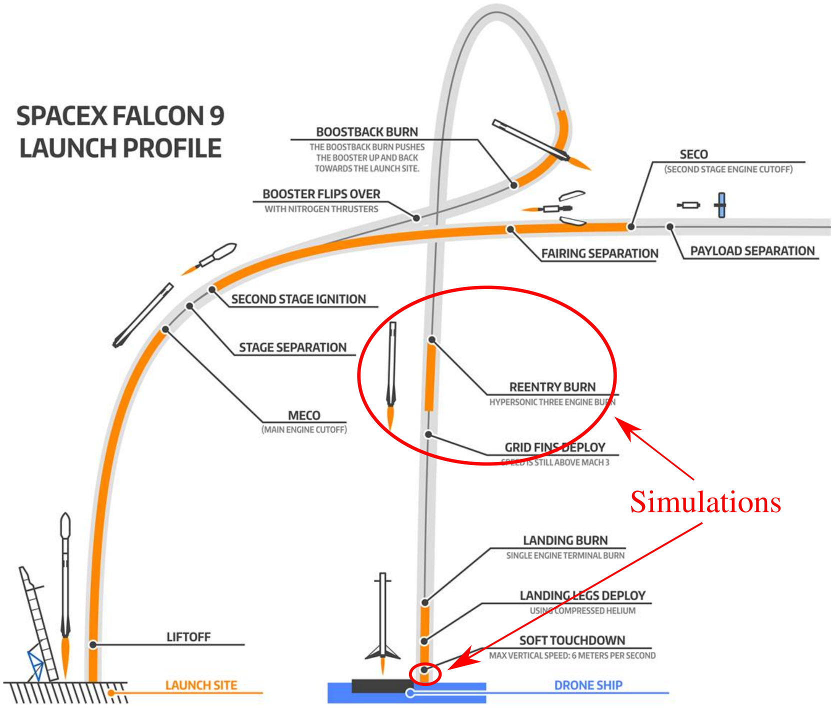

Figure 1.2. Launch profile of the SpaceX Falcon 9 [6].

A typical launch profile of SpaceX Falcon 9 is presented in figure 1.2. After lift-off, the Falcon 9 ascends till around 80 km, where the main engines are cut-off (MECO). Then the first and second stage separate: The second stage ignites and continues to its target orbit, whereas the first stage prepares for re-entry. It flips over using nitrogen thrusters and redirects to the launch site by igniting three of its nine main engines (boost back burn). This ignition of the main engines is the first out of three retro-propulsion maneuvers the first stage is conducting on its way back to Earth. After the boost back burn, the first stage describes a loop, reaches its peak altitude and starts its passive, ballistic re-entry. At high altitude (70 - 50 km depending on mission) the three engines are re-ignited to perform the second retro-propulsion maneuver, the re-entry burn. The re-entry burn is conducted in order to decrease the re-entry velocity. Therefore, the loads on the vehicle are reduced when entering into denser atmosphere layers. After approximately 30 s, the engines are switched off and the first stage continues its ballistic descent. Shortly before the ground, the central engine is ignited to brake and direct the stage to its landing site, where it touches down. The final approach before touch down of the first stage is depicted in figure 1.1.

1.2 Background and Objectives

Since the beginning of space travel, the multistage expendable launch vehicle has been state of the art for bringing payload into orbit. Although it has been a reliable approach, discarding parts or even the entire vehicle after every mission has led to enormous launch costs, thus restricting the commercial, scientific and military activities in space [7]. Therefore, re-usable vehicles present a economical and ecological approach, since the vehicles return back to their launch site to be refurbished and reused. However, previous experiences with re-usable vehicles such as Space Shuttle or Buran exhibit challenges and difficulties in finding a viable operational case [8].

New space companies, like SpaceX or Blue Origin, aim to reduce the launch costs significantly by re-introducing re-usable launch vehicles to the launch service market [7]. With the successful flights and re-flights of SpaceX Falcon 9's first stage and Falcon Heavy the interest in re-usable rocket-powered first stages for orbital launches has increased significantly.

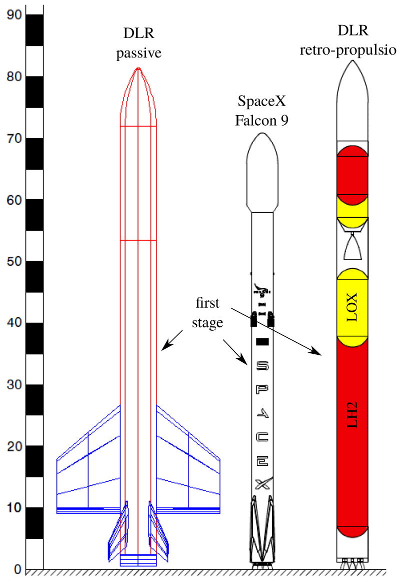

Figure 1.3. DLR reusable launcher configurations compared to SpaceX Falcon 9 [9, 10].

DLR has been evaluating different re-usable first stage concepts for some time (e.g. liquid fly-back boosters) [11]. The aim of the DLR study is to identify the most reliable and efficient concept for returning and re-using a launch system. This launch system must be capable of inserting a seven ton payload into the geostationary transfer orbit (GTO). With respect to the successful flights of SpaceX, DLR's current system analysis for this GTO mission, presented by Sippel et al. [8], focuses on identifying a technically feasible and efficient design by comparing the characteristics of a winged gliding stage with those of a retro-propulsion decelerated vertical landing vehicle. These two concepts are presented in figure 1.3 together with SpaceX Falcon 9. To compare and characterize these two re-usable launch vehicle concepts, multidisciplinary pre-design is necessary that generates a reliable dataset for evaluation [8].

The DLR retro-propulsion concept is very similar to the approach of SpaceX. The DLR first stage also uses nine circularly clustered engines for launch and ascend, three of the nine for the re-entry burn and one for the landing boost. The launch profile of Falcon 9 described in figure 1.2 can also be applied for the DLR configuration. However, some major differences are listed below:

	SpaceX Falcon 9 [12]	DLR retro-propulsion [9]
Propellants	RP1[1] & LOx	LH2 & LOx
Boost back burn	3 engines	Optional depends on mission
h_{peak} [km]	200	130
h at beginning of re-entry burn [km]	54	70
v at beginning of re-entry burn [km/s]	1.66	2.8
t re-entry burn [s]	30	35
Thrust T of single engine [kN]	756	1270
Vacuum thrust T of single engine [kN]	827	1380
L_{total} [m]	70	83
$L_{\mathrm{first\,stage}}$ [m]	47	58
$D_{\mathrm{first\,stage}}$ [m]	3.7	6.4
Carrier system lift-off mass [t]	550	800
First stage descent mass [t]	80	130
Descent propellant mass [t]	55	50

[1] Refined Petroleum-1

Table 1.1. Differences of SpaceX Falcon 9 and DLR retro-propulsion configuration.

This work is part of the pre-design process for the retro-propulsion decelerated vertical landing first stage. The general idea of this retro-propulsion approach is very similar to the concept of SpaceX: decelerate the returning first stage with a retro-propulsion maneuver at high altitudes ($\approx$ 70 km; upper red circle in figure 1.2). The first stage is then already relatively slow, when reaching denser atmosphere layers and the thermal and structural loads caused by friction are significantly reduced compared to the passively gliding vehicle. However, the retro-propulsion maneuver immerses the vehicle in a huge fireball of its own hot exhaust plume as depicted in figure 1.4 and exposes it to gas temperatures of several 1000 K. The atmosphere during the retro-propulsion maneuver is still thin. Thus, it is of practical interest to determine whether the vehicle walls demand a thermal protection system (TPS) due to the heat loads from the impinging hot plume. Two DLR studies started investigating this question. Ecker et al. [12] conducted LES and RANS simulations with DLR TAU for a Falcon-9-like configuration (vehicle and trajectory). They created a heat flux database from the RANS simulations and coupled it with a structural model in order to estimate the sidewall temperature increase of the first stage during the re-entry burn. Dumont et al. [9] based their investigations on the methodology of Ecker et al. and adapted it to the launch vehicle configuration of the DLR retro-propulsion approach. They also conducted RANS simulations to create a heat flux database for the sidewall. The heat loads to the first stage's sidewall are determined during the re-entry burn by coupling the heat flux database with a simpler structural modeling approach than Ecker et al. [12].

Figure 1.4. The re-entry burn of SpaceX Falcon 9's first stage [13].

The objective of this work is to better understand the impact of the flowfield on the heat transfer and to extend the investigations of Dumont et al [9]. Steady state RANS simulations with DLR TAU are conducted to establish a database for a different combustion chamber configuration than in [9]. Additionally to the sidewall, the heat loads to the baseplate are considered. Different flow (angle of attack, yaw angle) and vehicle conditions (implications of combustion chamber conditions, inactive engines, thermal nozzle radiation) are investigated as well as the thermal loads during landing boost.

1.3 Thesis Outline

This thesis is composed of five chapters describing the work performed and a final chapter summarizing the results and giving an outlook for future work.

Chapter 2 provides a literature review of supersonic retro-propulsion. The flowfield phenomena of a first stage during retro-propulsion are described together with occurring heat fluxes to the walls.

Chapter 3 presents the governing equations for the RANS simulations and gives a brief overview of their implementation in DLR TAU.

Chapter 4 describes preliminary studies on nozzle and plume flows to asses the modeling approach.

Chapter 5 describes the numerical setup for the SRP flowfield simulations. Furthermore, it shows and discusses the aerothermal effects of the SRP flowfield to the sidewall and baseplate heat fluxes for different flow situations.

Chapter 6 presents the aerothermal heating of the first stage's sidewall and baseplate over the re-entry burn from the heat flux database coupled with the structural model.

Chapter 7 summarizes the conclusions of this thesis with respect to the necessity of a thermal protection system for the first stage and presents recommendations for future works.

Chapter 2

Previous Work

This chapter describes the physical phenomena encountered by a re-entering first stage using retro-propulsion to decelerate its descent back to Earth. The focus is on the flowfield phenomena that contribute to the heat flux on the first stage walls during supersonic retro-propulsion.

2.1 Entering a Planet's Atmosphere

Entering a planet's atmosphere poses a fundamental challenge in spaceflight [14]. Depending on the mission of the space vehicle, the vehicle enters the atmosphere at sub-orbital, near-orbital or super-orbital velocities, v_{rel}, relative to the atmosphere. These velocities are much larger than the speed of sound of the atmosphere. Figure 2.1 illustrates the different orbits and corresponding entries to a planet's surface. The orbital velocity represents the velocity a vehicle needs to orbit a planet (v_{orb}; black, entry in green). Sub-orbital velocities (v_{sub}) refer to velocities that are not sufficient to enter an orbit around the planet, but result in a parabolic flight back to the planet (blue). Super-orbital velocities correspond to velocities larger than the orbit velocity v_{sup} (red) including the velocity a vehicle must have to leave the gravitational field of the planet, escape velocity v_{esc} . A

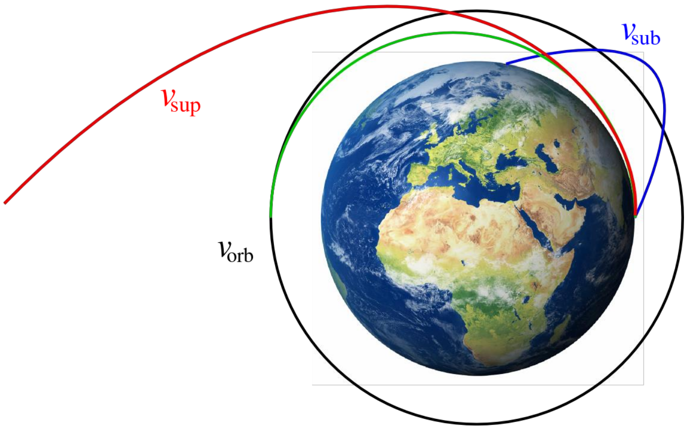

Figure 2.1. Earth orbits and corresponding relative velocities [15].

vehicle entering a planet has a kinetic energy proportional to the relative velocity squared. Transferring this relation to enthalpy and considering only hypersonic velocities ($M > 5$) yields the following approximation [16]:

$$h_{\mathrm{t}} \approx \frac{v_{\mathrm{rel}}^2}{2} \tag{2.1}$$

Inserting the three different orbital velocities of the Earth give an idea of the enthalpy levels h involved:

	v_{rel} [km/s]	h [MJ/kg]	Entry missions
Sub-orbital	2 - 7.9	$h(v_{\mathrm{sub}} = 2\,\mathrm{km/s}) = 2$	SHEFEX, first stage SpaceX Falcon 9
Orbital	7.9	31	MIRKA, Soyuz, Space Shuttle
Super-orbital	> 7.9	$h(v_{\mathrm{esc}} = 11.2\,\mathrm{km/s}) = 63$	Apollo, Hayabusa, Stardust

Table 2.1. Velocities and enthalpies at Earth entry [15].

In order to return and land safely on a planet's surface, the vehicle's kinetic energy must be dissipated during entry. Examples for successfully returned vehicles are listed in table 2.1.

As a vehicle enters the atmosphere from space, it traverses three different flow regimes. The Knudsen number Kn characterizes these three regimes by the ratio of the mean free path of atmospheric molecules to the characteristic length of the space vehicle (cf. appendix A). At high altitudes (> 100 km), atmospheric density is very low and the interaction of the vehicle and the surrounding atmosphere is characterized by free molecular flow. The mean free path between molecules is very large, thus they are rarely colliding with each other. As the vehicle descends into more denser atmosphere parts, the inter-molecule collisions become more frequent and contribute to the vehicle aerodynamics. This is defined as transitional regime which defines the transition from free molecular flow to continuum flow. Descending further, the vehicle enters the continuum regime which continues till the planetary surface and where the Navier-Stokes equations are valid. At this entry stage the importance of aerodynamics forces and heating rates increase rapidly [17]. These loads primarily result from the pressure- and friction-based drag (deceleration) and the hypersonic air compression at the bow shock (thermal loads) [15]. This phase is the most critical, in which the peak loads are reached. Once the vehicle is decelerated to low supersonic and finally subsonic speeds, the final descent to the surface is outside any critical condition. As seen with the examples for Earth entries, the higher the vehicle's speed the higher the energy that needs to be dissipated and consequently the higher the loads the vehicle is exposed to.

In order to avoid destroying the vehicle during entry, it is protected by a thermal protection system (TPS). The TPS shields the heat from the vehicle by ablation processes (burning up) or by radiation cooling (i.e. emitting the absorbed heat from the flow via thermal radiation). The Space Shuttle Orbiter, for example, was cooled radiatively. While Apollo or Soyuz capsules have ablators that burn up during the critical entry phase [14, 15].

Traditionally, the space vehicle decelerates most of the entry trajectory passively, i.e. the shape of the vehicle and the surrounding atmosphere causing enough friction to slow down the vehicle without destroying it. Active deceleration is applied only to initiate the entry phase and after the critical phase to slow down the landing. Most vehicles initiate the entry by performing a de-orbit maneuver: retro-propulsion is applied to slow down and leave the orbit maneuvering towards the entry point. The final approach after the critical phase is actively decelerated either with parachutes (e.g. Gemini, Apollo) [14] or a combination of parachutes and retro-rockets (e.g. Soyuz, Mars Science Laboratory) [5, 4]. Figure 2.2 shows the landing Soyuz capsule which employs a parachute and retro-rockets for the final landing approach and touch down.

Figure 2.2. Soyuz capsule ignites retro-rockets to cushion the landing impact [18].

Actively controlling and decelerating the entry of a vehicle has been investigated since the 1950s [19, 3]. Retro-propulsion presents one method for active deceleration. It has often been discussed to be used more extensively for entering vehicles but has re-surfaced only recently for various applications. NASA is planning to land heavier payloads (i.e. > 10 t) on Mars [3]. DLR intends to decelerate a returning first stage of a future launch vehicle with retro-propulsion [8] and SpaceX currently retrieves the first stages of Falcon 9 by using retro-propulsion [20].

Korzun gave a detailed overview of available research on retro-propulsion in her work [3], focusing on aerodynamics of blunt, capsule-like body configurations. However, current studies on slender bodies of revolution, such as a first stage, are very limited. Love [21] investigated the boundary layer behavior and total drag, when a small counterflowing jet exhausts from the nose of a slender body into a low supersonic freestream. He found an earlier transition to turbulent flows due to the jet and large reductions in forebody pressure drag. Venkatachari et al. [22] investigated drag reduction of a long penetration counterflowing jet. The available research data on heat transfer investigations is listed in section 2.2.4.

2.2 Physics of Supersonic Retro-Propulsion

This section describes the physics and phenomena occurring in a supersonic retro-propulsion flowfield step by step. Starting with a supersonic jet flow, then adding an opposing supersonic freestream around a blunt body, we arrive at the supersonic retro-propulsion flowfield: a counterflowing jet in a supersonic freestream.

2.2.1 Supersonic Jet and Plume Flow

During the supersonic retro-propulsion maneuver three engines are activated to provide the necessary thrust to decelerate the first stage. Therefore, the flowfield of a supersonic jet exhausting from a nozzle is described and then the interaction of clustered jet flows is examined. The flowfield of a supersonic jet is also important for the conducted preliminary studies in chapter 4.

Single Jet Flow A supersonic jet exhausting into a quiescent medium is displayed in figure 2.3. The jet perfectly expands into the surrounding, i.e. the jet pressure at the nozzle exit p_e equals the ambient pressure p_∞ ($p_\mathrm{e} = p_\infty$) [23]. The jet layer, the line of constant ambient pressure, separates the jet fluid from the surrounding medium [24]. The formation of (hot) jet exhaust gases outside the nozzle is called plume [25]. Starting from the nozzle exit a shear layer evolves (along the jet boundary) due to the velocity difference between the supersonic jet and the quiescent surrounding. At the beginning the shear layer is still negligible and the jet can maintain its exit velocity for several exit diameters (inviscid or potential core region). As the jet propagates further, these velocity gradients contribute more significantly to the mixing of the plume with the surrounding fluid causing the jet velocity to decay (potential core break down) [26, 27].

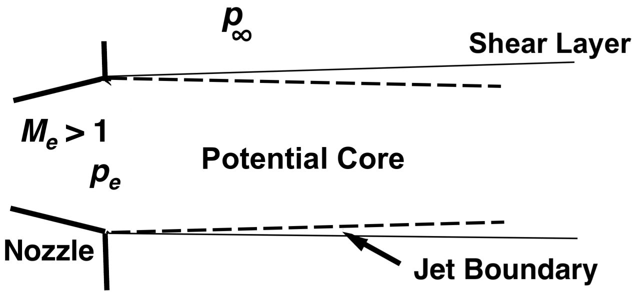

Figure 2.3. Schematic diagram of perfectly-expanded jet adapted from [3].

Besides the perfect plume expansion, there exist two other expansion conditions for supersonic nozzle flows: over-expanded and under-expanded. These conditions depend only on the nozzle pressure ratio, i.e. nozzle exit pressure over local ambient pressure (p_e/p_∞). Figure 2.4 illustrates their basic structures. Over-expanded jet flows (figure 2.4a) have a lower jet static pressure at the nozzle exit than the local ambient pressure, $p_\mathrm{e} < p_\infty$. Oblique Compression waves (shocks) form at the nozzle exit to raise the jet exit pressure

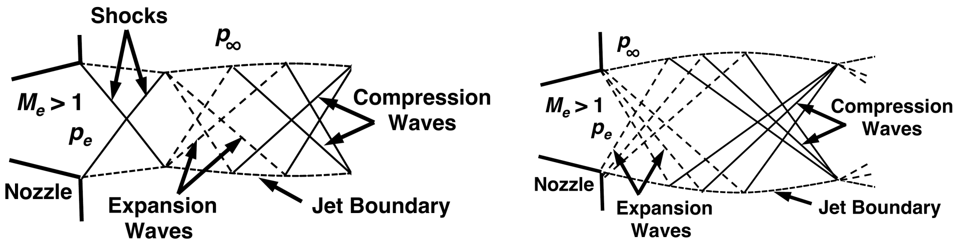

(a) Over-expanded **(b)** Under-expanded

Figure 2.4. Jet structures for over-expanded and under-expanded conditions adapted from [3].

to the surrounding ambient pressure. These shocks intersect and are reflected at the opposite jet boundary as expansion waves. These expansion waves are then themselves reflected at the boundaries as compression waves. This pattern is repeated consecutively until mixing along the jet boundaries with the ambient fluid dissipates the plume structure [3, 23].

For under-expanded jet flows (figure 2.4b) the nozzle exit pressure is higher than the local ambient pressure, $p_\mathrm{e} > p_\infty$. As a result, Prandtl-Meyer expansion waves form at the nozzle exit to lower the jet exit pressure to the ambient pressure. These expansion waves are reflected at the opposite jet boundary as compression (oblique shock) waves. This pattern, similar to the over-expanded jet flow, continues until the jet flow dissipates [3, 23].

In a rocket nozzle during ascent, the nozzles are mostly operated at conditions at which the atmospheric pressure is significantly lower than the nozzle exit pressure, $p_\infty \ll p_\mathrm{e}$. Thus, the engines are running at highly under-expanded conditions. The plume exiting the nozzle at these conditions is several times larger than the vehicle and contracts when reaching lower altitudes [25]. The aforementioned expansion and compression patterns for under-expanded flows form a slightly different flowfield due to the huge pressure difference between nozzle exit and ambient conditions, i.e. huge nozzle pressure ratio. Figure 2.5 depicts the general structure. At the nozzle lip the flow undergoes a Prandtl-Meyer expansion and continues to expand, forming the inviscid supersonic inner core. The arising expansion waves reflect from the jet boundary (constant pressure streamline)

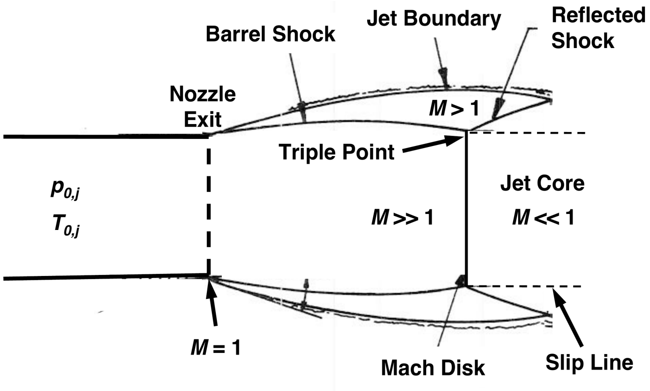

Figure 2.5. Schematic diagram of highly under-expanded jet [3].

as compression waves, subsequently coalescing to form the barrel shock [28]. The barrel shock separates the expanding plume (inner core) from the ambient flow, whereas outside a high-velocity shear layer evolves along the jet boundary. The supersonic inner core passes through the Mach disk, a strong normal shock. At the intersection of Mach disk and barrel shock (triple point) an oblique reflected shock forms. Flow passing through the Mach disk becomes subsonic, while flow traversing the barrel shock and the oblique reflected shock remains at lower supersonic speed. [3, 25].

The majority of the fluid exiting the nozzle is at high supersonic speeds. However, the boundary layer consists of a subsonic region near the wall and a supersonic layer on top of the subsonic layer. At the nozzle lip, the supersonic part of the boundary layer can only be reflected up to a certain angle, whereas the subsonic layer can be deflected up to 180°. Although the subsonic boundary layer represents only a small portion of the overall nozzle mass flow, it nevertheless lets the exhaust gases flow backward on the outside of the nozzle. This backflow impinges on the baseplate and causes heating of the vehicle base and propulsion system parts [25].

Plume Flows of Clustered Nozzle Configurations The first stage's engines are clustered very narrowly, similar to SpaceX Falcon 9's first stage engines (see figure 2.6a). In this case, the separate plumes interact with each other at under- and highly under-expanded conditions. This interaction of multi-nozzle (mostly four forming a square) plumes has been investigated over decades [29, 30, 31, 32]. Figure 2.6b shows a schematic sketch of the occurring flowfield. For highly under-expanded jet flows the plume continues to expand after the nozzle exit. Therefore, the individual expanding plumes mutually impinge on each other generating oblique shocks. On impingement some of the low-energy gas within the mixing region of plume is unable to overcome the pressure rise by the shock. Consequently it is deflected onto the base, forming a base-impinging reverse jet. The impinging flow is then turned radially outward between the engines as it re-accelerates to ambient pressure. The amount of flow that is deflected strongly depends on the nozzle pressure ratio. The higher the nozzle pressure ratio (i.e. the higher the altitude) the more flow is reversed until a choked condition is reached. Then the base flow

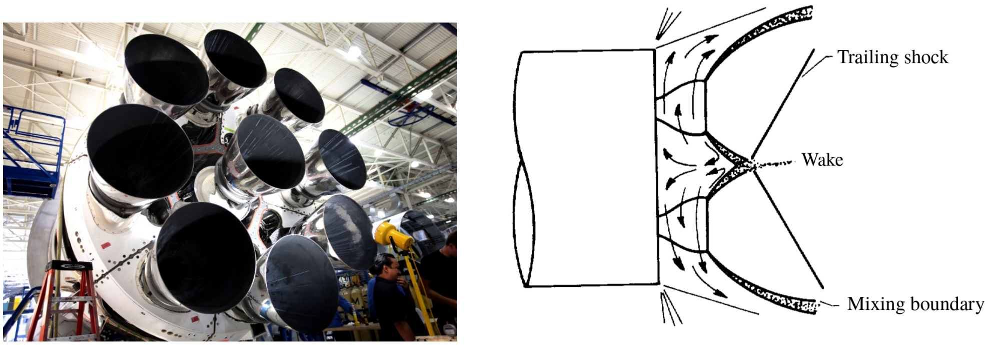

(a) Merlin Engines of SpaceX Falcon 9's first stage [33].

(b) Baseflow for highly-underexpanded plume flows of clustered nozzles adapted from [30].

Figure 2.6. Clustered nozzle configuration and their plume interactions.

parameters are the highest and become independent of further increases in altitude [30]. The part of the plume having enough energy to traverse the shocks continues to expand and coalesce into one plume forming all the afore described plume phenomena [34] (see also multiple nozzles in section 2.2.3).

Plume-Ground Interaction The plume-ground interaction becomes important during the final landing approach as depicted in figure 1.1. The hot jet and plume exhausting from the nozzle impinge on the landing surface. The phenomena of a supersonic impinging jet have widely been investigated, e.g. [35, 36], but mostly for nozzle pressure ratios below 10 [37]. The interaction between plume, ground and vehicle has mostly been in focus for Lunar or Martian landers [38, 37]. Investigations for terrestrial applications can be found for subsonic plume flows of vertical take-off planes [39, 40, 35].

2.2.2 Bow Shock

A vehicle, such as a returning first stage, obstructs a supersonic flow. The flow reacts by forming a bow shock in order to decelerate itself in front of the vehicle [41]. Figure 2.7 shows the detached bow shock of the returning DLR first stage with deactivated engines. A normal shock forms in front of the nozzles and turns in an oblique shock at the borders. In the case of the supersonic re-entry flow in this thesis, the freestream air heats to several 1000 K over the shock at high velocities. The temperature jump decreases as the vehicle decelerates. The velocity is reduced to subsonic speeds over the normal shock portion and to lower supersonic speeds over the oblique part. Furthermore, an increase in (static) density and (static) pressure is observed [23].

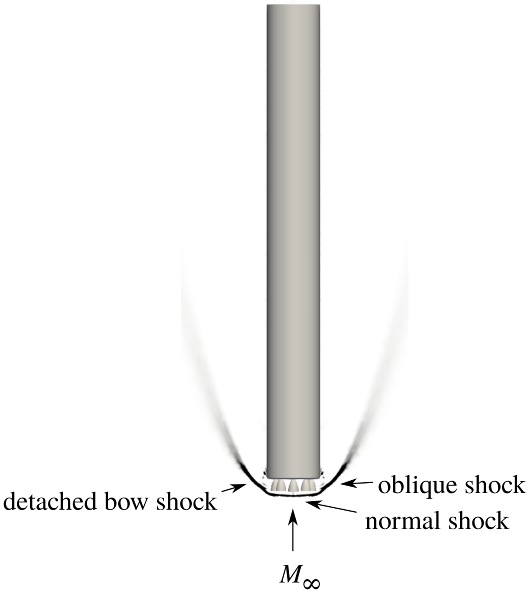

Figure 2.7. Simplified supersonic re-entry flow around the returning DLR first stage.

2.2.3 Supersonic Retro-propulsion Flowfield

To arrive at the description of the supersonic retro-propulsion flowfield we put together the afore described phenomena:

- Supersonic freestream
- Opposing supersonic jet flow

and arrive at a vehicle firing its engines against a supersonic freestream. The detached bow shock forces the exhausting plume to decelerate and turn around the vehicle. Whereas, the plume pushes the bow shock further downstream from the vehicle acting as an additional obstruction, to which the freestream adapts. Thus, the aerodynamics of the vehicle are affected by the engine thrust level as well as the interaction between the jet flow and the bow shock [41] and are suggested to be highly unsteady [3].

Single Nozzle Figure 2.8 illustrates the general structure of a supersonic retro-propulsion flowfield with a single central nozzle. After passing the bow shock, the freestream flow is deflected by the contour of the effective obstruction of plume and vehicle, the contact surface. The highly under-expanded plume exhausting from the nozzle decelerates through the Mach disk to subsonic conditions or through the barrel shock to lower supersonic conditions and turns to flow axisymmetrically back around the vehicle [41]. A shear layer (with sub- and supersonic regions) evolves along the outer jet boundary due to large velocity gradients between the flow behind the bow shock and the opposing plume flow.

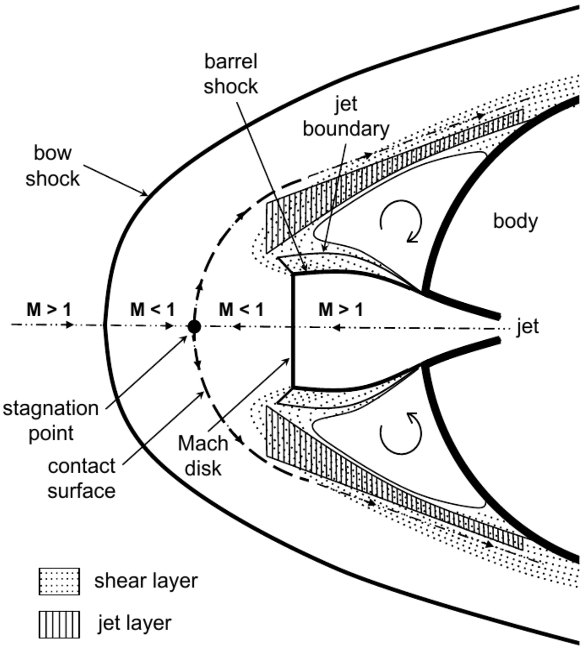

Figure 2.8. Supersonic retro-propulsion flowfield around a capsule with a single, central nozzle [3].

The flow in shear layer together with the jet layer flow are drawn towards regions of low pressure near the nozzle exit, forming recirculation zones [3].

Multiple Nozzles During the retro-boost maneuver of the returning first stage three engines are ignited in-line. Berry et al. [42, 43], Gilles [44] and Schauerhammer et al. [45] investigated the interaction of plumes exhausting from different multiple nozzle configurations both experimentally and numerically. Their nozzles were not arranged in-line but the occurring flow phenomena can be transferred. Figure 2.9a shows a time averaged Schlieren image from [43] with three active nozzles spaced 120° apart forming a triangle. In the experiments the nozzles were far apart from each other, thus forming separate plumes. The "V"-like structure represents the internal plume boundary of the barrel shocks of the two closest jet plumes [43, 45]. The jet termination structure and the detached bow shock are clearly visible. For nozzles in close proximity of each other, figure 2.9b illustrates plume coalescence into a single effective plume. The plumes impinge on each other and form intersecting shock waves [44].

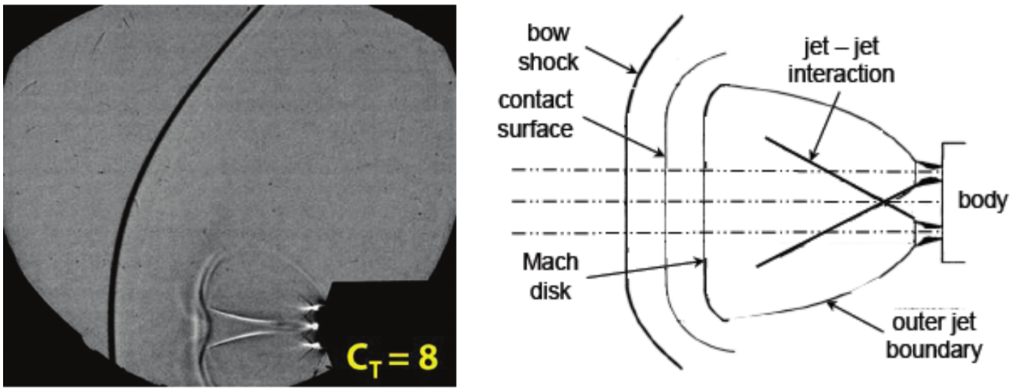

(a) Averaged Schlieren image of trinozzle conifguration at $M_\infty = 2.4$ [43].

(b) Schematic sketch of plume coalescence of four clusterd nozzles into a single effective plume [41, 44].

Figure 2.9. Plume structures of multiple nozzle in a supersonic retro-propulsion flowfield.

In numerical investigations of twin-nozzle rocket plume phenomenology without opposing freestream by Ebrahimi et al. [34], interacting plumes forming shocks on impingement were observed.

The intersection shock of the plume-plume interaction were also captured in the RANS simulations of the returning first stage (see section 5.3.2) and are also visible in simulations of SpaceX Falcon 9 [46].

Returning First Stage The SRP flowfield of the returning DLR first stage at the beginning of the breaking maneuver in figure 2.10 shows all the phenomena described in the previous sections: A detached bow shock forms in front of the plume exhausting from three engines. Compared to the passive re-entry in figure 2.7, the plume significantly obstructs the oncoming flow by displacing the bow shock by 120 m upstream. After passing the shock, the freestream is deflected by the oncoming jet plume creating the contact surface. The plume forms the barrel shock at the sides and the Mach disk in front and is heated up to 4000 K over the shocks. The sonic line indicates the subsonic region after the normal shocks and frames the supersonic shear layer. The shear layer in this case stems from the velocity gradients between the flow traveling over the barrel shock and interacting with the reversed plume flow coming from further downstream. Due to the three plumes coalescing into one, the recirculation region is pushed away from the base impinging on the sidewall. The area of plume impingement depends highly on the nozzle pressure ratio (cf. section 5.3.2). The plume-plume interaction shocks are also very faintly visible near the nozzle exits.

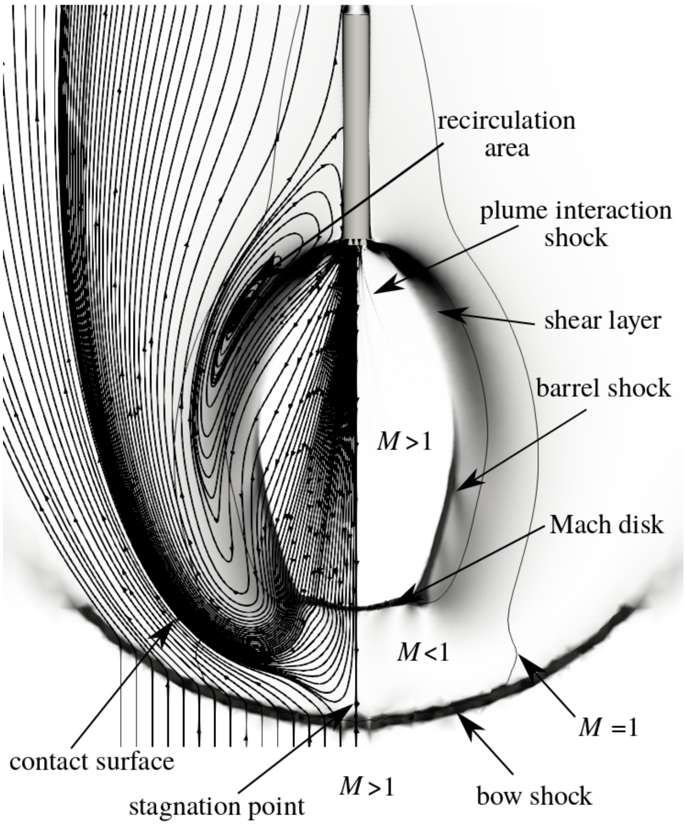

Figure 2.10. Supersonic retro-propulsion flowfield around returning DLR first stage from simulations. Streamlines only on the left side in order to display the other phenomena more clearly.

2.2.4 Heat Transfer

To date the research on heat transfer for supersonic retro-propulsion or more generally counterflowing jets in supersonic freestream has only concentrated on sphere-like and blunt compact bodies (capsules). Darso et al. [19] gave an extensive review of counterflowing jets in supersonic freestreams. Counterflowing jets belong to the "active flow control" concepts and has been a topic of research since the 1950s. The idea is to modify the external flowfields of vehicles traveling at transonic to hypersonic speeds, in order to reduce wave drag and aerothermal loads and for spacecrafts deceleration. The investigations in Darso's review showed i.a. that the jet mass flow rate [47, 48, 49, 50], the nozzle pressure ratio or the Mach number [51] strongly influence the flowfield as well as the heat transfer. The general finding was that a counterflowing jet can significantly reduce the (stagnation) heat transfer.

The first stage ignites three of her nine engines during the SRP maneuver. Therefore, a cluster of counterflowing jets and the interactions of their plumes need to be considered. The plume-plume interaction (cf. section 2.2.1) produces a base-impinging reverse jet, that can lead to severe heating on the base [29, 30, 31, 32]. The base heating strongly depends on the amount of flow that is deflected towards the base. The most significant parameter is the nozzle pressure ratio. The base heating raises with increasing nozzle pressure ratio. At a high pressure ratio the flow reaches choked conditions at the base and the base heating arrives at its maximum becoming independent of further increases in nozzle pressure ratio [30].

The interest in investigating the heat transfer to slender cylinder-shaped geometries in supersonic retro-propulsion flowfields has surfaced only recently: Successful re-entries of SpaceX Falcon 9's first stages and the aforementioned DLR study on assessing the most efficient approach to retrieve a first stage of a future launch vehicle [8]. SpaceX hardly publishes any relevant data. Only in collaboration with NASA some data was made public. NASA observed a SpaceX Falcon 9 during ascend and the supersonic retro-propulsion maneuver with infrared cameras in order to demonstrate their imaging capability and gain insight into the flight conditions during SRP. Their imaging estimated the surface temperature of the first stage before and after the maneuver concluding surface heating to a maximum temperature of 450 K after the maneuver [13]. NASA also validates their numerical flow solvers for SRP with SpaceX Falcon 9 data from retro-propulsion maneuvers [46].

In the course of the DLR study on future launch vehicles, two numerical studies [12, 9] were conducted on investigating the thermal loads and heating of the returning first stage during SRP. They carried out numerical simulations to examine the occurring heat loads of a generic SpaceX Falcon 9 geometry on the Orbcomm OG2 mission [12]. They found that the plume extension has significant influence on the wall heat flux. However, the heating of the first stage's wall by around 100 K over the breaking maneuver to a maximum of 400 K is insignificant. Furthermore, DLR investigated the retro-propulsion configuration of the launcher study (see figure 1.3 on the right), a geometrically similar configuration to SpaceX Falcon 9 but with different engines and re-entry trajectory (see table 1.1 and figure 5.1a for details). The main results shows that the heat loads of the SRP maneuver are lower than in the re-entry phase afterwards with deactivated engines. Moreover, the chosen trajectory has significant influence on the occurring heat loads [9].

One objective of this thesis is to contribute to the better understanding of the heat transfer of slender bodies in a supersonic retro-propulsion flowfield. Therefore, some preliminary studies on plume flows where conducted in this thesis in order to asses the modeling approach for the returning first stage (cf. chapter 4).

Chapter 3

Governing Equations and Numerical Method

This chapter covers the mathematical description of the re-entry flow with retro-propulsion via the Reynolds-averaged Navier-Stokes (RANS) equations, as well as the DLR TAU finite volume flow solver, which was applied to solve them.

3.1 Governing Equations: Compressible RANS

This section briefly describes the derivation of the Reynolds-averaged Navier-Stokes equations for a compressible fluid flow using the control volume approach in the Eulerian reference frame. The physical principles and assumptions to model a supersonic re-entry flow with Navier-Stokes equations are presented, as well as the Reynolds and Favre-averaging approach necessary for the compressible RANS equations.

3.1.1 Physical Principles and Balance Equations

In order to derive the Navier-Stokes equations, balance equations for the fundamental principles of a fluid flow through a control volume are established. The control volume is fixed in space and the fluid flows through it, as depicted in figure 3.1. The control volume allows to describe the temporal variation of the fluid flow at this specific location in space (Eulerian reference frame).

The equations to describe the fluid motion are based on the following three fundamental physical principles [23]:

1) Conservation of mass

2) Newton's second law: Force $\equiv$ Variation of momentum in time

3) First law of thermodynamics: Conservation of energy

Together with the three primary flow variables for a compressible flow, pressure p, density ρ, and velocity $\vec{v}$, they form the basis for describing any fluid flow. In order to express their variation in time inside the control volume, balance equations are used.

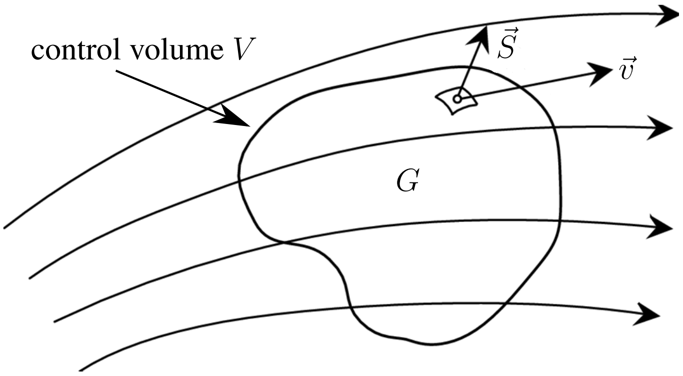

Figure 3.1. Fluid flowing through a control volume fixed in space adapted from [52].

The variation in time of a generic flow property G (either vector or scalar) inside the control volume can be described by its interaction with the surroundings plus its production/destruction inside the control volume [53]:

$$\frac{\partial g^+}{\partial t} = -\frac{\partial \vec{\phi_G}}{\partial x_i} + \dot{g}^+ \tag{3.1}$$

where g^+ stands for the volumetric density of G, i.e. G per unit volume and

$$\vec{\phi_G} = g^+\,\vec{v} + \vec{J_G} \tag{3.2}$$

indicates the convective ($g^+\,\vec{v}$, related to mass transport) and diffusive ($\vec{J_G}$) fluxes over the control volume boundaries.

Conservation of Mass: Continuity Equation Replacing the flow property G by the mass m, its volumetric density ρ and taking into account that there is no diffusive mass flux and internal production of mass, we can re-write (3.1) as [54]

$$\frac{\partial \rho}{\partial t} + \frac{\partial}{\partial x_i}(\rho v_i) = 0. \tag{3.3}$$

Momentum Balance Equation The momentum balance equation characterizes the flow property momentum $\vec{I} = m\vec{v}$. From the generic balance equation (3.1) we can replace the following expressions (by neglecting the production term):

$$G = I = m\,\vec{v}, \qquad g^+ = \rho\,\vec{v}, \qquad \vec{\phi_I} = \rho\,\vec{v}\,\vec{v} + \vec{J_I}. \tag{3.4}$$

The diffusive flux $\vec{J_I}$ is defined via Newton's second law. The temporal variation of fluid momentum equals the sum of external forces acting on the fluid (particle). The external forces can be divided into surface forces, which are acting per contact and body forces (e.g. gravitational force), which are acting from a distance (and correspond to the production term). The surface forces transfer momentum to the control volume surface via surface stresses (normal and tangential) and therefore define the diffusive momentum fluxes.

The stresses normal to the surface are related to the pressure p. The tangential stresses (shear stresses) can be described via Newton's hypothesis, that the flux of a variable is proportional to its spatial gradient and Stokes' assumption that the volumetric viscosity is negligible [54]

$$\tau_{i,j} = \mu \left(\frac{\partial v_i}{\partial x_j} + \frac{\partial v_j}{\partial x_i} \right) - \frac{2}{3} \mu \frac{\partial v_k}{\partial x_k} \delta_{i,j} \tag{3.5}$$

where μ indicates the dynamic or molecular viscosity, a fluid property, and $\delta_{i,j}$ the Kronecker delta . The first term in brackets is often referred to the rate of strain tensor $s_{i,j}$.

The expression for the diffusive flux of momentum (shear stress) together with the other expressions, yield the balance equation for the flow property momentum, also referred as Navier-Stokes equation [54]

$$\frac{\partial}{\partial t}(\rho v_i) = -\frac{\partial}{\partial x_j}(\rho v_j v_i) - \frac{\partial p}{\partial x_i} + \frac{\partial \tau_{i,j}}{\partial x_j}. \tag{3.6}$$

Energy Conservation Equation The third principle, conservation of energy, determines that the total energy E is preserved, i.e. energy can neither be destroyed nor created ($\dot{g}^+ = 0$). From the generic balance equation (3.1), (3.2) the following expressions can be replaced by:

$$G = E, \qquad g^+ = \rho\, e, \qquad \vec{\phi_E} = \rho\, \vec{v}\, e + \vec{J_E} \tag{3.7}$$

where $e = E/m$ stands for the specific total energy. Considering only specific internal energy u and specific kinetic energy $v_i^2/2$, the diffusive flux of E, $\vec{J_E}$, consists of work and heat. Work represents the diffusive flux of kinetic energy and can be derived from the shear stresses, i.e. work $\equiv -v_i \tau_{i,j}$. The diffusive flux of internal energy is understood as heat. Fourier, following the same hypothesis as Newton for the shear stresses, suggested that the flux of heat is proportional to its spatial gradient, i.e. specific heat $\dot{q}_j = -k\, \frac{\partial T}{\partial x_j}$. k stands for the thermal conductivity, a fluid property.

Introducing the specific enthalpy $h = e + p/\rho$ (to account for pressure), the total energy conservation equation can be written as ([54]):

$$\frac{\partial}{\partial t}\left[\rho \left(u + \frac{1}{2} v_i\, v_i\right)\right] + \frac{\partial}{\partial x_j}\left[\rho\, v_j \left(h + \frac{1}{2} v_i\, v_i\right)\right] = \frac{\partial}{\partial x_j}(v_i\, \tau_{i,j}) - \frac{\partial \dot{q}_j}{\partial x_j}. \tag{3.8}$$

An equation of state is necessary to relate p, ρ and T. For a thermally perfect gas, as used in the simulations, the perfect gas law

$$p = \rho R T \tag{3.9}$$

is applied. $R = c_p - c_v$ is the perfect gas constant. In a thermally perfect gas the specific heat capacities (c_p and c_v) are only a function of T and are e.g. available in the CEA thermodynamic and transport database [55]. Thus, e and h can be expressed as

$$e = c_v(T)\, T \qquad h = c_p(T)\, T. \tag{3.10}$$

3.1.2 Prerequisite for Compressible RANS

This section introduces the limits in which the governing equations are valid and defines the Reynolds, as well as the Favre averaging method.

Area of Validity for the Compressible RANS Equations

The supersonic re-entry flow with retro-propulsion was assumed to follow the continuum hypotheses [9, 12]. In the continuum regime a linear relation between shear stress and velocity gradients and isotropic pressure are assumed, as well as for the heat flux and the spatial temperature gradient (except within shocks) [17].

The following requirements have to be met in order to model a fluid flow with the Navier-Stokes equations [53, 56]:

- Continuum hypothesis ($Kn \leq 0.01$)
- Local thermodynamic equilibrium (equation of state)
- Newtonian fluid, i.e. linear relation between shear stress and velocity gradients

If reacting flows are considered, additional balance equations for the involved chemical species have to be established [56].

Reynolds Averaging

In engineering applications, it is often sufficient to know the overall, average behavior of a fluid flow. Reynolds introduced a time averaging approach, which is suitable for stationary flows, i.e. turbulent flows, that on the average, do not vary in time. In these flows every instantaneous flow quantity is expressed as $g(\vec{x}, t)$. Reynolds decomposed the instantaneous flow quantity $g(\vec{x}, t)$ into its fluctuating $g'(\vec{x}, t)$ and its time-averaged quantity $\bar{g}(\vec{x})$ [54]

$$g(\vec{x}, t) = \bar{g}(\vec{x}) + g'(\vec{x}, t). \tag{3.11}$$

The time average, $\bar{g}(\vec{x})$, is given by

$$\bar{g}(\vec{x}) = \lim_{T \to \infty} \frac{1}{T} \int_{t}^{t+T} g(\vec{x}, t) \mathrm{d}t. \tag{3.12}$$

For the derivation of the Reynolds averaged Navier-Stokes equation it is necessary to introduce the following averaging rules:

$$\bar{g'} = 0 \qquad \bar{\bar{g}} = \bar{g} \qquad \overline{g'\bar{g}} = 0 \qquad \overline{g'g'} \neq 0. \tag{3.13}$$

Favre Averaging

In compressible flows, Reynolds averaging introduces density, temperature, velocity and pressure fluctuations. In order to reduce the amount of fluctuating terms, when time-averaging the balance equations, Favre suggested a density-weighted averaging procedure. The flow variable $g(\vec{x}, t)$ can be again decomposed into a mean part $\widetilde{g}(\vec{x})$ using the density weighted average [54],

$$\widetilde{g}(\vec{x}) = \frac{1}{\bar{\rho}} \lim_{T\to\infty} \frac{1}{T} \int_{t}^{t+T} \rho(\vec{x}, t)\, g(\vec{x}, t) \mathrm{d}t \tag{3.14}$$

in which $\bar{\rho}$ stands for the Reynolds-averaged density, and a fluctuating part $g''(\vec{x}, t)$. Auxiliary relations include

$$\overline{\rho g''(\vec{x}, t)} = 0 \qquad \overline{\rho \widetilde{g}(\vec{x})} = \bar{\rho}\widetilde{g}(\vec{x}) = \overline{\rho g(\vec{x})} \qquad \overline{g''(\vec{x}, t)} \neq 0. \tag{3.15}$$

3.1.3 Compressible RANS

For the compressible RANS equations the flow properties of the balance and conservation equations, as well as of the equation of state must be decomposed into their mean and fluctuation part.

The properties p, ρ and q_j are decomposed using the Reynolds averaging procedure, whereas v_i, h, e and T follow the Favre averaging. The continuity equation [54]

$$\frac{\partial \bar{\rho}}{\partial t} + \frac{\partial}{\partial t}(\bar{\rho}\widetilde{v}_i) = 0 \tag{3.16}$$

is identical to its instantaneous counterpart in equation (3.3). The balance momentum equation [54]

$$\frac{\partial}{\partial t}(\bar{\rho}\widetilde{v}_i) + \frac{\partial}{\partial x_j}(\bar{\rho}\widetilde{v}_j\widetilde{v}_i) = -\frac{\partial \bar{p}}{\partial x_i} + \frac{\partial}{\partial x_j}\left[\bar{\tau}_{i,j} - \overline{\rho v_i'' v_j''}\right] \tag{3.17}$$

differs only by the appearance of the Favre-averaged Reynolds-stress tensor $t_{i,j}$

$$\bar{\rho}\, t_{i,j} = \overline{\rho v_i'' v_j''}. \tag{3.18}$$

This is the time-averaged rate of momentum transfer due to turbulence.

The mean balance energy equation for total energy i.e. the sum of internal energy, mean-kinetic energy and turbulent kinetic energy, yields [54]

$$\begin{aligned}\frac{\partial}{\partial t}\left[\bar{\rho}\left(\widetilde{u} + \frac{\widetilde{v}_i\widetilde{v}_i}{2}\right) + \frac{\overline{\rho v_i'' v_i''}}{2}\right] + \frac{\partial}{\partial x_j}\left[\bar{\rho}\,\widetilde{v}_j\left(\widetilde{h} + \frac{\widetilde{v}_i\widetilde{v}_i}{2}\right) + \widetilde{v}_j\frac{\overline{\rho v_i'' v_i''}}{2}\right] \\ = \frac{\partial}{\partial x_j}\left(-\bar{\dot{q}}_j - \overline{\rho v_j'' h''} + \overline{\tau_{i,j}\, v_i''} - \overline{\rho v_j'' \tfrac{1}{2} v_i'' v_i''}\right) \\ + \frac{\partial}{\partial x_j}\left[\widetilde{v}_i\left(\bar{\tau}_{i,j} - \overline{\rho v_i'' v_j''}\right)\right].\end{aligned} \tag{3.19}$$

Numerous additional terms appear, each standing for a physical process or property.

- $\frac{1}{2}\overline{\rho v_i'' v_i''}$ kinetic energy per unit volume of turbulent fluctuations
- $\overline{\rho v_j'' h''}$ turbulent transport of heat
- $\overline{\tau_{i,j}\, v_i''}$ molecular diffusion (dissipation)
- $\overline{\rho v_j'' \frac{1}{2} v_i'' v_i''}$ turbulent transport of kinetic energy

The Favre averaged perfect gas law:

$$\bar{p} = \bar{\rho} R \widetilde{T} \tag{3.20}$$

3.2 Turbulence Modeling

A turbulence model consists of an algebraic formula or a set of differential equations which allows the determination of the unknown Reynolds stresses and turbulent energy fluxes arising from the averaging process [54].

3.2.1 Closure Problem

The time-averaging process of the fluid motion equations introduces unknown turbulent terms. In order to compute all mean-flow properties of the turbulent flow, a description for those unknowns is needed. Since the number of unknowns exceeds the number of equations, the system of equations can not be closed, i.e. solved. In order to be able to solve the set of RANS equations a turbulence model is needed, which relates the unknown turbulent quantities to known variables of the mean flow [54].

3.2.2 Eddy Viscosity Approach

Eddy viscosity models are based on Boussinesq's analogy: Modeling the Reynolds stresses as linearly proportional to the mean rate of strain tensor. Thereby, the turbulent quantities are linked to the mean velocity gradients.

$$-\overline{\rho v_i'' v_j''} = 2\overline{\rho}\nu_\mathrm{t}\left(\bar{s}_{i,j} - \frac{1}{3}\frac{\partial v_k}{\partial x_k}\delta_{i,j}\right) - \frac{2}{3}\overline{\rho v_i'' v_i''}\delta_{i,j} \tag{3.21}$$

where ν_t is called eddy or turbulent viscosity.

The turbulent heat flux is modeled analogously by linking it to the averaged temperature gradient

$$\overline{\rho v_j'' h''} = -\overline{\rho c_p}\alpha_\mathrm{t}\,\frac{\partial \overline{T}}{\partial x_j}. \tag{3.22}$$

α_t stands for the turbulent diffusivity of heat [53].

Depending on the turbulence model, additional closure approximations may be needed [54]. The turbulent viscosity and turbulent diffusivity are linked via the turbulent Prandtl number

$$Pr_{\mathrm{t}} = \frac{\nu_{\mathrm{t}}}{\alpha_{\mathrm{t}}}. \tag{3.23}$$

Thereby, the unknown turbulent quantities are deferred into a single unknown quantity, the eddy viscosity. The task of the turbulence model is to determine this quantity in every point of the flowfield.

Analogously to the molecular viscosity, the turbulent viscosity is assumed to be proportional to a velocity and a length scale, representing the large scale turbulent motion. All eddy viscosity turbulence models are based on this definition for the turbulent viscosity. They are characterized by the number of differential transport equations they use to represent the eddy viscosity. Zero-equation models use a simple algebraic relation for the eddy viscosity (e.g mixing length models). One-equation models, such as the Spalart-Allmaras model [57], use one transport equation and an algebraic relation to account for the velocity and length scale. Two-equations models present velocity and length scale via transport equations, e.g. Menter-SST model [58].

Spalart-Allmaras One-equation Model

The Spalart-Allmaras [57] model directly solves a transport equation for an effective eddy viscosity rather then deriving it from the velocity or time scale. The model was developed for aerodynamic applications such as the flow past a wing, where it performs well for mixing layers and far wakes. However, it is less suitable for applications involving jet-like free shear regions [54] and lacks sensitivity to transport processes in rapidly changing flows [59]. Nevertheless, it was chosen for modeling the supersonic retro-propulsion flowfield, since it is numerically robust and converges fast, which are desired properties in a preliminary design study.

Menter Shear Stress Transport (SST) Two-equation Model

The Menter-SST model [58] combines the modeling advantages of the k-ω (near-wall region) and the k-ϵ model (freestream independence). Further, it introduces an improved transport of turbulent shear stresses. It uses a transport equation for the turbulent kinetic energy as the velocity scale and a combination of ω and ϵ for the length scale [60]. The SST model leads to a significant improvement for all flows involving adverse pressure gradients. The model is also capable of accurately predicting pressure-induced separation and the resulting viscous-inviscid interaction [58]. However, the model demands more computational time and showed convergence problems for the simulation of the Space Shuttle Main Engine (cf. section 4.2).

3.3 Finite Volume Method and DLR TAU

The DLR Tau-code is a three-dimensional finite volume scheme solving the Reynolds-averaged Navier-Stokes equations.

3.3.1 Finite Volume Method

The finite volume method is a suitable approach to approximate the integral balance and conservation equations [61]. Writing the generic balance equation (3.1) in its integral form for a control volume V yields

$$\frac{\partial}{\partial t}\int_V g^+ \mathrm{d}V = -\int_{\partial V} \vec{\phi}_G \cdot \vec{n}\,\mathrm{d}S + \int_V \dot{g}^+ \mathrm{d}V. \tag{3.24}$$

For simplicity reasons the finite volume approach is derived for the conservation equation ($\dot{g}^+ = 0$) in one dimension. In order to approximate the integral conservation equation the spatial domain has to be discretized. The finite volume method allows a very general grid concept , i.e various shapes like triangles, squares or any other polygon [61].

Re-writing the integral balance equation for an arbitrary grid cell C_i, integrating over the time interval $[t_n, t_{n+1}]$ by introducing the integral mean values at time t_n, $(g_i^+)^n$, and t_{n+1}, $(g_i^+)^{n+1}$ and replacing the cell boundary ∂C_i by the k_i borders K_j with adjacent cells gives the evolution of the integral mean value in the cell:

$$(g_i^+)^{n+1} = (g_i^+)^n - \frac{1}{|C_i|}\int_{t_n}^{t_{n+1}} \sum_{j=1}^{k_i} \int_{K_j} \phi_G \cdot n\,\mathrm{d}S. \tag{3.25}$$

The integral mean value at t_{n+1} results from the value at t_n and the integral flux over the cell borders k_i. This equation represents the basis for constructing the finite volume method.

The key element of a finite volume method is the numerical flux, which is used to approximate the flux over the cell borders. Herein results one difficulty of the finite volume approach: The method uses integral mean values, but demands local values at the borders to calculate the flux over the border. Thus, a finite volume method consists of two steps: Reconstructing the local values at the borders from the integral mean values and the flux calculation.

In order to arrive at the finite volume method in one dimension, an equidistant discretization is introduced with increments Δt and Δx. The grid interval in space is defined as $\Delta x \equiv [x_{i-1/2}, x_{i+1/2}]$, where $x_{i+1/2}$ is the mean value between x_i and x_{i+1}. Integrating equation (3.25) over x and t and introducing the abbreviations $(g_i^+)^n$ for the spatial integral mean value of (g_i^+) over Δx at t_n and $(\phi_G)_{i+1/2}$ for the temporal integral mean value of ϕ_G over Δt at $x_{i+1/2}$ results in the evolution equation of temporal and spatial integral mean values. For the one dimensional finite volume method, the fluxes $(\phi_G)_{i-1/2}$ and $(\phi_G)_{i+1/2}$ are approximated by the numerical fluxes $(\gamma_G)_{i-1/2}$ and $(\gamma_G)_{i+1/2}$ respectively:

$$(g_i^+)^{n+1} = (g_i^+)^n - \frac{\Delta t}{\Delta x}\left[(\gamma_G)_{i+1/2} - (\gamma_G)_{i-1/2}\right]. \tag{3.26}$$

Thereby $(\gamma_G)_{i+1/2}$ is the integral mean flux value of time interval $[t_n, t_{n+1}]$ at point $x_{i+1/2}$. The main task for constructing a finite volume method consists of finding a suitable approximation for the flux function γ [61].

3.4 DLR TAU

The DLR TAU-code is a CFD platform for simulating viscous and inviscid flows. It can be applied to complex geometries and covers the low subsonic to hypersonic flow regime. The TAU-code is split into three independent modules: a preprocessing module, the solver and the grid adaptation module [62, 63].

Grid

The spatial discretization in TAU is based on a dual-grid, cell-vertex scheme. The flow quantities are stored on the vertices of the primary grid, which makes the solver independent of the primary grid element types. For the finite volume discretization, a secondary grid cell is constructed around each vertex of the primary grid as shown in figure 3.2. The control volumes are constructed by connecting the midpoints of the edges, the face centers and, in 3-D, the centers of the primary elements.

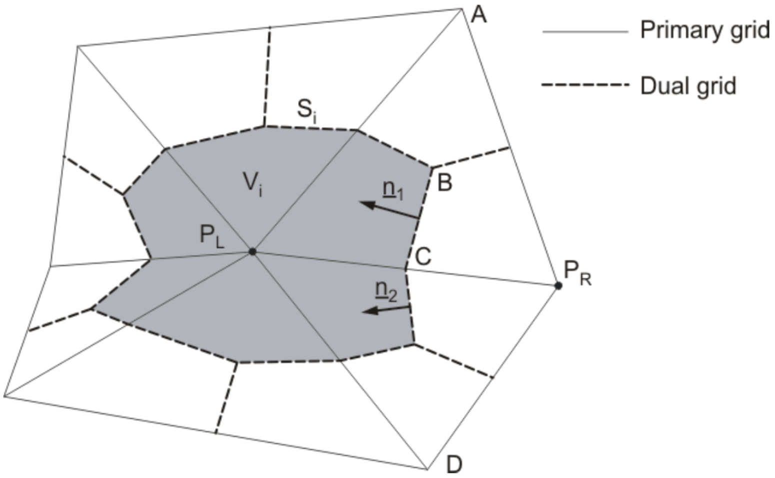

Figure 3.2. Dual cell structure for spatial discretization in TAU [62].

TAU allows (block-) structured and hybrid unstructured grids composed of hexahedrons, prisms, tetrahedrons and pyramids. The first two element types are usually used in semi-structured layers above surfaces for a better resolution of boundary layers. Tetrahedrons fill the computational domain, allowing local refinement without hanging nodes. The pyramids are needed for transitions between elements with quadrilateral and triangular faces.

For parallel computations, subsets of the dual grids are created by domain decomposition in the preprocessing step. The communication between the sub-domains is based on MPI. TAU includes the adaptation and the deformation module as means for grid modification.

Flow Solver

The flow solver module computes inviscid fluxes by employing either a second-order central scheme or a variety of upwind schemes, using linear reconstruction for second-order spatial accuracy. Viscous fluxes are generally computed with second-order central differences. The time-accurate three-dimensional Navier-Stokes equations are marched in time towards steady state by a Runge-Kutta time stepping method or a backward Euler implicit scheme solved with LU-SGS or SGS iterations. For time accurate calculations a dual-time stepping approach is implemented that is accurate up to third order.

Convergence to steady state is accelerated by local time stepping, residual smoothing and multigrid. The coarse grids in the multigrid approach are provided by agglomeration, i.e. merging fine grid control volumes.

The RANS turbulence models implemented in the solver include linear as well as non-linear eddy viscosity models covering one- and two-equation model families. Non-linear explicit algebraic Reynolds stress models (EARSM) are integrated and it is further possible to perform Detached Eddy Simulations and Large Eddy Simulations [62].

High enthalpy (re-entry) flows are modeled as (reacting) thermally perfect gases. A transport equation is solved for each individual species. The properties of the reacting gas mixture are computed from the thermodynamic properties of the individual species using the Wilke mixture rules for viscosity and the rule by Herning and Zipperer for heat conductivity. Modeling of fully catalytic and non-catalytic walls is also possible. The species diffusion fluxes are modeled using Fick's law. Thermal non-equilibrium is computed by solving an additional transport equation for the vibrational energy of each molecule in non-equilibrium [62].

TAU-THETA Radiation Tool

The TAU-THETA radiation tool [64] allows the determination of radiative heat fluxes emitted from gas particles or surfaces via the Monte-Carlo method or the Discrete Transfer Radiation Method. In this thesis the Discrete Transfer Radiation Method was used to determine the radiative heat flux from the nozzle walls to the baseplate.

The Discrete Transfer Radiation Method, like the Monte Carlo Method, is based on the transfer of independent radiative energy particles (photons), which are emitted from each point in the system. The Discrete Transfer Radiation Method is limited to a finite number of discrete directions.

Chapter 4

Plume Flow Studies

A main feature of supersonic retro-propulsion is the plume exhausting from the nozzles. Therefore, the different modeling aspects of the SRP flowfield around the first stage are assessed by investigating supersonic jet flows into quiescent air from literature cases.

The impact of the turbulence model on the plume structure is investigated by conducting simulations with Spalart-Allmaras and Menter SST turbulence models and comparing them to experiments from Seiner et al. [27] and simulations by NPARC [65]. The gas modeling is also tested via the Seiner experiment and the corresponding simulation by Yoder et al. [66]. Finally, the numerical setup and modeling of the first stage retro-propulsion flowfield is tested by simulating a Space Shuttle main engine nozzle flow and comparing the results to simulations presented by Wang [67]. An overview of the conducted simulations is given in table 4.1.

	Seiner [27]		Wang [67]
	NPARC [65]	Yoder [66]	
Plume structure and turbulence modeling	x	x	x
Gas modeling		x	x
First stage modeling			x

Table 4.1. Conducted 2D nozzle and plume flow simulations.

4.1 Seiner – Plume Structure and Gas Modeling

Seiner et al. [27] conducted experiments on an ideally expanding, heated, $M = 2$ jet flow into quiescent air. The nozzle used was axisymmetric, convergent-divergent and cooled with an exit radius of $R_{\mathrm{exit}} = 4.572$ cm (cf. figure 4.1). During the experiments the jet was heated to total temperatures of $T_{\mathrm{t,\,jet}} = 313$ K to 1534 K.

This experiment has subsequently been used to validate CFD codes. Two TAU simulations of the experiment are used to compare to literature values by:

- NPARC Alliance Validation Archive test case [65] ($T_{\mathrm{t,\,jet}} = 313$ K) for comparing the plume structure of the two different turbulence models

- Yoder et al. [66] ($T_{\mathrm{t,jet}} = 1366$ K) to assess the influence of the gas modeling (also on the plume structure).

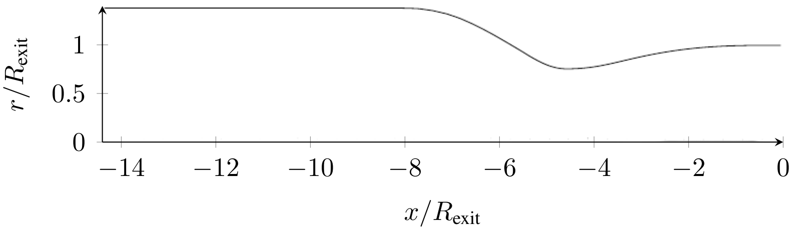

Figure 4.1. Sketch of the axisymmetric Seiner nozzle adapted from Yoder [66].

4.1.1 NPARC Alliance Validation Archive Test Case ($\mathrm{T}_{\mathrm{t,jet}} = 313$ K)

NPARC Alliance Validation Archive [65] provides RANS simulations of the Seiner experiment with various turbulence models on a structured grid using the Wind-US flow solver. The grid and applied boundary conditions, as well as the simulation results of the Wind-US code were published. The axisymmertric nozzle used in the experiments allowed the reduction to a 2D axisymmetric problem. The structured grid (see figure 4.2a) provided by the NPARC website was adapted for the TAU solver. The structured grid (see figure 4.2a) provided by the NPARC website was adapted for the TAU solver. The grid

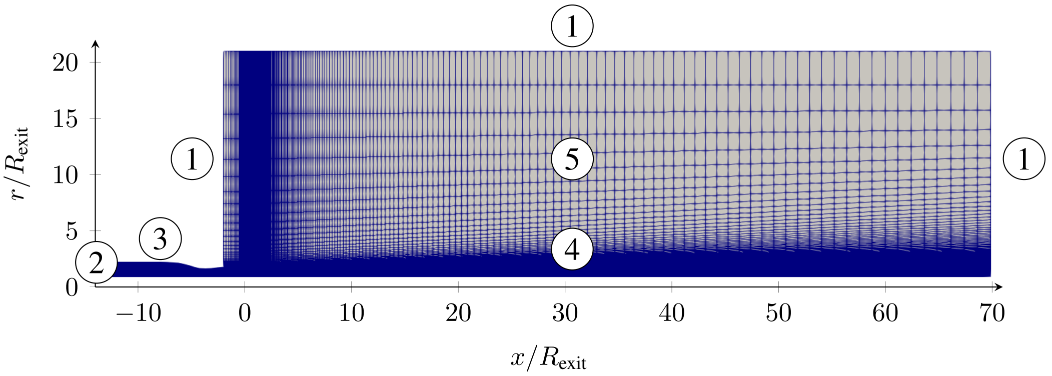

(a) 2D structured grid for Seiner nozzle simulation from [65].

Boundary conditions	Marker	p_{t} [bar]	T_{t} [K]	M
Freestream	①	1.015	294.4	0.01
Inflow	②	7.93	313	–
Viscous and adiabatic wall	③			
Symmetry axis	④			
Inviscid wall	⑤			

(b) Boundary conditions from NPARC set in TAU.

Figure 4.2. Boundary conditions and grid of NPARC simulation.

is 3.4 m long in streamwise direction and 1 m high and consists of 110,000 points. The corresponding boundary conditions are listed below in table 4.2b.

As the nozzle wall temperature could not be determined from literature, an adiabatic nozzle wall was assumed. Air was used as working fluid and presumed as an ideal gas (cf. table 5.5 for composition), with the properties being independent of temperature ($\kappa = 1.4$ and $R_{\text{air}} = 287$ J/(kg K)). The air was heated to 313 K, then accelerated in the nozzle till $M = 2$ and ideally expanded into quiescent air. The numerical setup is identical to the setup for the first stage (cf. section 5.2.1). In addition to the Spalart-Allmaras turbulence model, the Menter-SST model was applied.

The Mach number contours of the simulation with Menter SST are displayed in figure 4.3. The jet maintains the exit Mach number over the whole cross-section for approximately 3 nozzle exit radii. From there on, the turbulent mixing with the surrounding starts to become stronger. The jet inviscid core region (dark red) diminishes by the growing shear layer. The potential core is maintained till approximately $x/R_{\text{exit}} = 20$. After this distance the mixing between jet and the surrounding causes the jet core to break down and to dissipate.

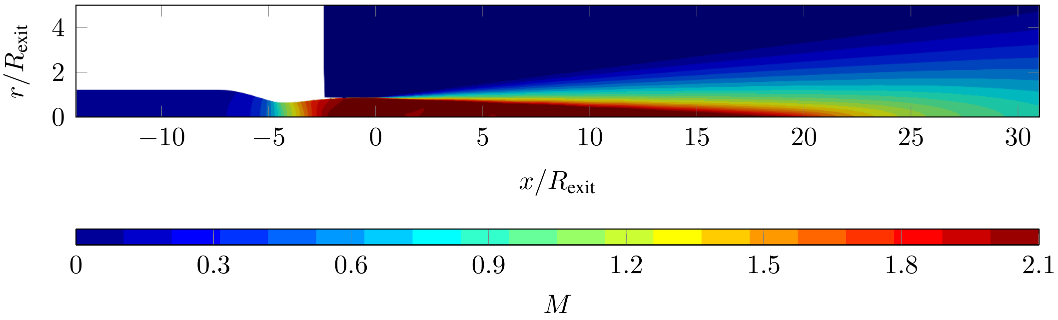

Figure 4.3. Mach number contours of simulations with Menter-SST.

The velocity decay of the jet velocity on the centerline (v_{c}) is depicted in figure 4.4. The simulations with the Menter SST and Spalart-Allmaras turbulence model are compared to the experiment of Seiner ($T_{\text{t, jet}} = 313$ K) and a Menter-SST simulation from the NPARC Alliance Validation Archive. In the experiment the jet potential core region was measured till $x/R_{\text{exit}} = 21$. The two simulations with Menter SST are a little shorter than the observations from the experiment ($x/R_{\text{exit, TAU}} = 19$, $x/R_{\text{exit, NPARC}} = 18$), whereas the Spalart-Allmaras simulation produces a significantly shorter core region ($x/R_{\text{exit}} = 14$). The shock and expansion patterns in the core region are clearly visible and do not strongly vary between the different simulations. The most significant difference between experiment and simulations is the steeper decline of the simulation centerline velocity. This is a general shortcoming of the eddy viscosity approach. The steeper velocity slope is caused by a substantially higher turbulent mixing rate in the simulations. The jet velocities of the simulations, after the core break down, are between 40 and 50 % smaller than the experiment. Thus, the jet and its surrounding mix much more thoroughly in the simulations than they do in reality.

Overall, the Menter SST simulation reproduces the jet flow more accurately than the Spalart-Allmaras simulation, but is computational more expensive and less sturdy. For 1

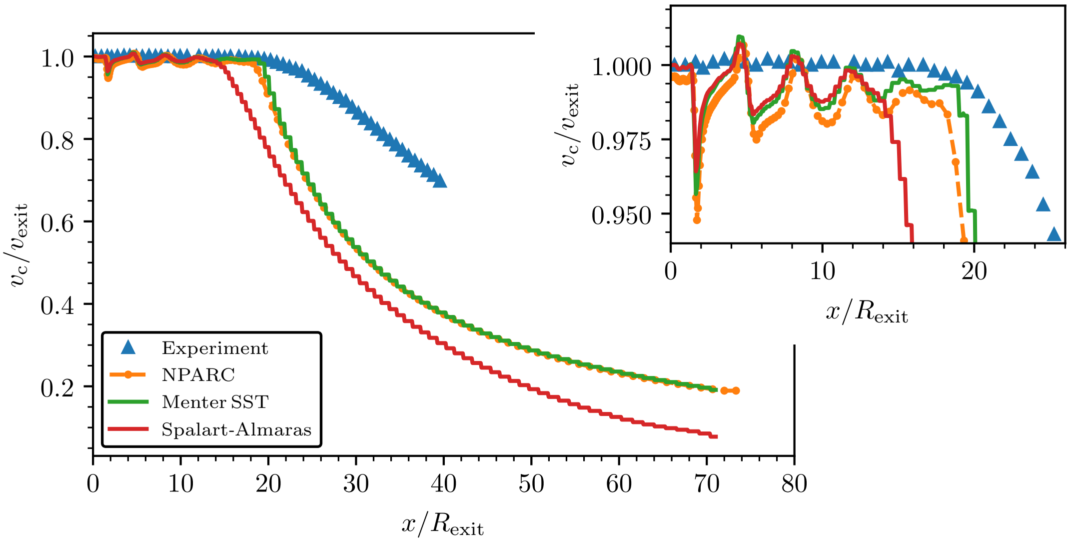

Figure 4.4. Jet velocity decay on centerline for different turbulence models compared to Seiner experiment and NPARC simulationss.

million iterations the Menter-SST calculations took 5 h, whereas Spalart-Allmaras a little under 4 h.

4.1.2 Yoder ($T_{t,\,jet} = 1367$ K)

Yoder et al. [66] investigated the effects of gas modeling on the nozzle performance numerically with the Wind-US CFD code (version 2). They conducted RANS simulations with the Menter SST turbulence model of the Seiner experiment at a total jet temperature of $T_{t,jet} = 1367$ K. The working fluid was modeled as air mixed with combustion products from the heating process (see table 4.2 for mixture composition). The mixture was then assumed to be a thermally perfect, frozen gas expanding over the nozzle into quiescent air. Yoder et al. used almost identical boundary conditions as NPARC. The only difference, apart from the jet total temperature, was the freestream Mach number, set to $M = 0.2$.

Species i	N_2	O_2	CO_2	H_2O
w_i [%]	78.07	15.61	15.61	2.79

Table 4.2. Frozen exhaust composition in mass fractions w_i [66].

For the RANS simulations with TAU the NPARC grid was used with Menter SST turbulence model and the boundary conditions from Yoder et al. The modeling of the exhaust gas and air followed the gas modeling process with CEA described in section 5.2.2.

The static temperature decay (normalized by $T_{t,jet}$) of the exhausting jet and plume along the centerline is illustrated in figure 4.5. The overall flow pattern is similar to the NPARC case (figure 4.3). The jet potential core length is still under-predicted and the higher turbulent mixing of the simulations causes a stronger decay in temperature than in the experiment. However, the jet core region shows that the simulations capture the shock-expansion pattern adequately and agree in temperature profile.

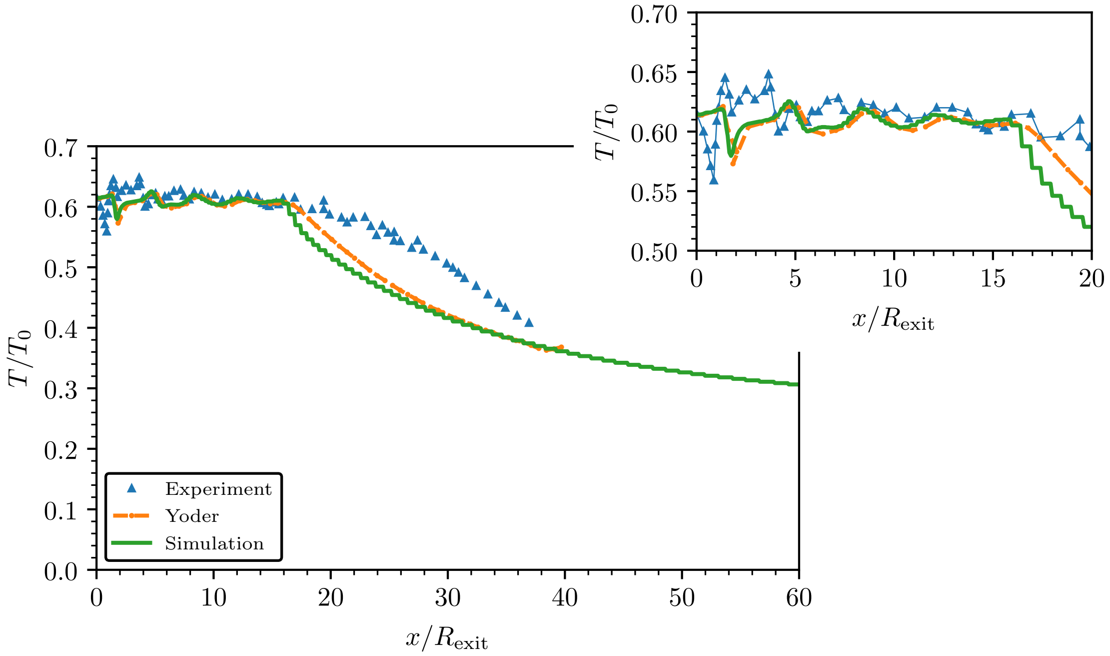

Figure 4.5. Comparison of centerline temperature decay to Seiner experiment [27] and simulations from Yoder [66].

4.2 Wang – Assessing the Modeling Approach

Wang conducted numerical studies [67] to develop a strategy for computing rocket engine design parameters such as axial thrust and convective and radiative wall heat fluxes through parametric investigations. His computational methodology is based on the finite-volume, chemically reacting, pressure-based formulation UNIC. He applied it on simulations of the regeneratively cooled Space Shuttle Main Engine (SSME) thruster hot-firing at sea level, using an extended k-ϵ turbulence model. The simulations are conducted on a 2D axisymmetric hybrid grid with 17,000 points (see bottom figure 4.7, which displays a refined version of the grid (point number was not indicated by Wang)). For the gas modeling he used a seven-species (H_2, O_2, H_2O O, H, OH ,N_2), nine-reaction mechanism to describe the finite-rate H_2/O_2 afterburning kinetics.

A sketch of the SSME nozzle together with the boundary condition markers is displayed in figure 4.6a, for the applied boundary conditions see table 4.6c.

The nozzle wall was set to the isothermal temperature profile from figure 4.6b. This temperature profile was also applied to the nozzle walls of the first stage for the simulation 7Bntp (cf. section 5.5.4).

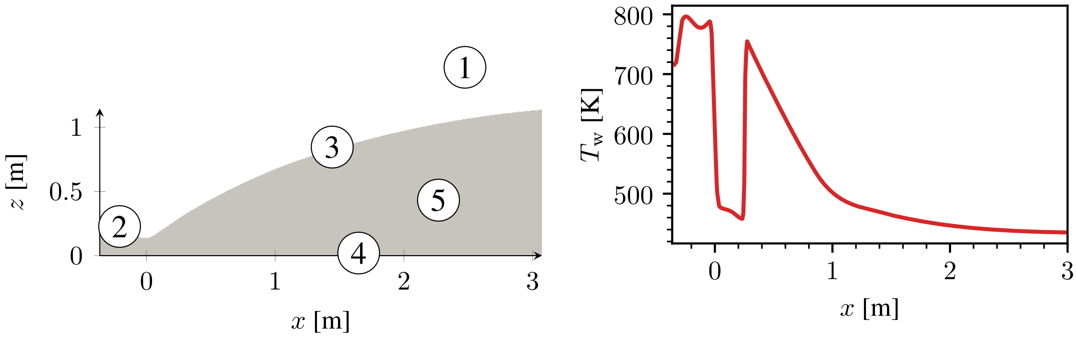

(a) Sketch of SSME nozzle with boundary condition markers of table 4.6c.

(b) Temperature profile of nozzle wall.

Boundary conditions	Marker	p_t [bar]	T_t [K]	M	m_{O_2}/m_{H_2}
Freestream	①	1.01325	288.15	0.06	
Combustion Chamber	②	202.41	3639	–	6
Viscous and isothermal wall	③				
Symmetry axis	④				
Inviscid wall	⑤				

(c) Boundary conditions of SSME simulations [67].

Figure 4.6. Nozzle geometry and boundary conditions of Wang's SSME simulation.

For the TAU simulations the numerical setup for the first stage simulations was used (cf. section 5.2.1) together with the boundary conditions provided by Wang. The grid for the nozzle was reverse engineered from the pictures and information Wang provided. It is also 2D axisymmetric structured/unstructured and consists of 100,000 points (cf. figure 4.7 top). The significant higher point number stems from the considerably finer boundary layer and near wall grid. The exhaust gas, as well as the surrounding air were modeled as a thermally perfect and frozen gas following the procedure from section 5.2.2 using the chamber and species conditions Wang provided.

The evolution of the Mach number is depicted in figure 4.7 for the TAU simulations at the top and Wang's simulation on a refined grid at the bottom. The M contours show a highly over-expanded nozzle flow ($p_{\mathrm{exit,c}} \approx 1000$ Pa) that produces oblique shocks at the nozzle lip and a Mach disk in the inner core. The Mach disk of the TAU simulations is curved and occurs further downstream, but the general flow features are captured. A comparison of the nozzle flow properties showes a very good agreement between the Wang and the TAU results. As an example for the nozzle flow properties, the convective nozzle wall heat flux (figure 4.8) is given. The heat flux reaches its maximum of 160 MW/m^2 in the nozzle throat and reduces to 3 MW/m^2 in the diverging part.

TAU simulations with Menter-SST were also conducted, but not presented due to convergence issues.

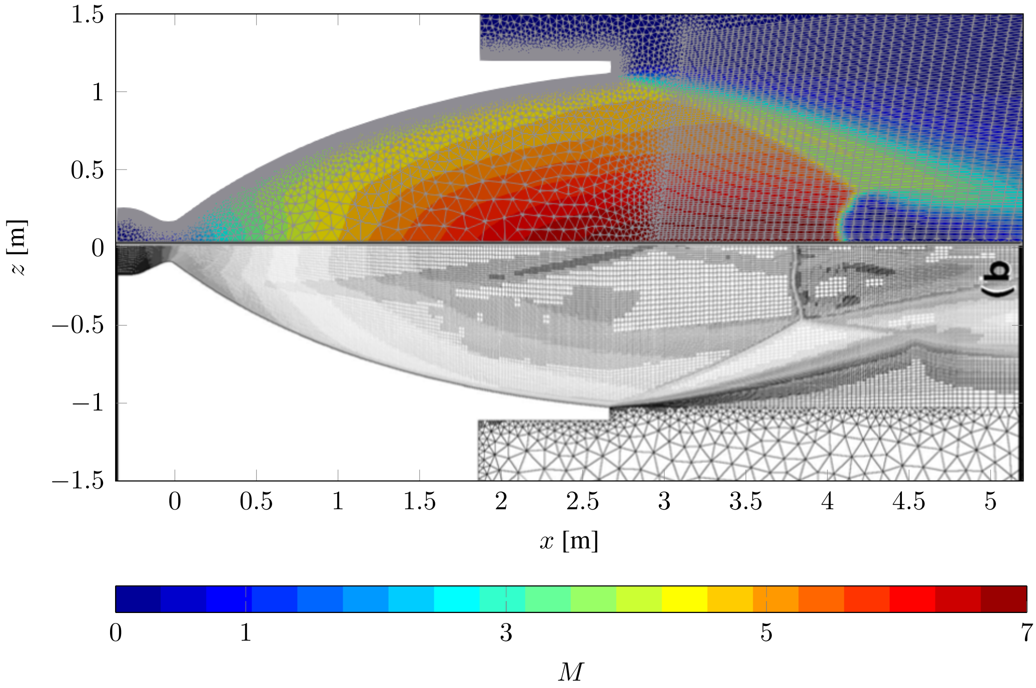

Figure 4.7. Mach number contour comparison of TAU simulations and Wang [67] together with grids.

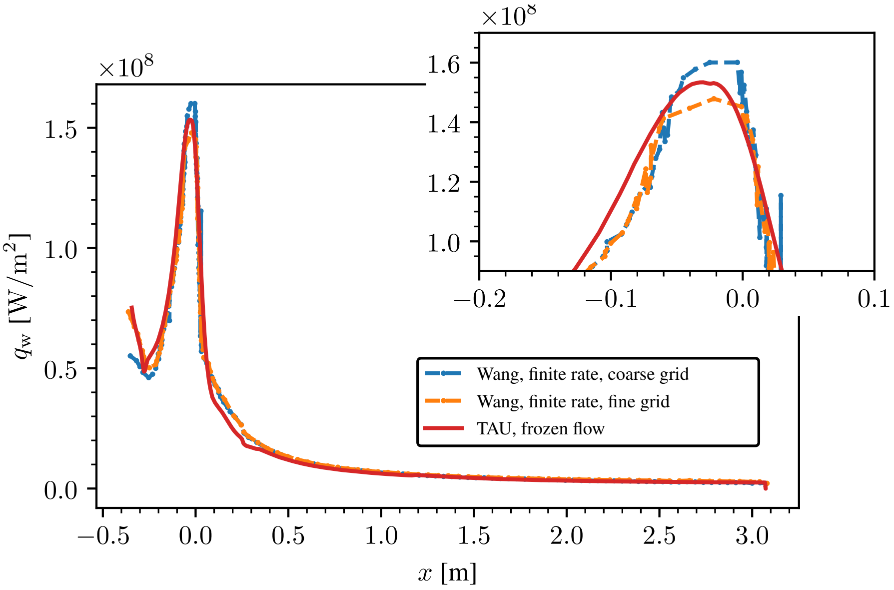

Figure 4.8. Wall heat flux compared to simulations from Wang.

4.3 Oberservations and Conclusion

The turbulence and gas modeling approach of the first stage SRP simulations were examined by comparing TAU results to experimental data from Seiner and to numerical results from NPARC and Yoder. Additionally, a SSME nozzle flow simulation provided by Wang was investigated.

The reproduction of the shock-expansion in the plume structure from the Seiner experiment conditions are in general good agreement with literature. However, the Spalart-Allmaras model predicted the jet potential core length about 30 % shorter than in reality. This is due to the elevated turbulent mixing from the turbulence model.

The simulations of the SSME reproduced the nozzle flow very well, but differed in the jet and plume structure. Simulations with Menter SST showed convergence issues.

Implications on the first stage simulations are:

- Higher turbulent mixing due to one-equation Spalart-Allmaras model, but reduced computational effort and more stable (only one transport equation to solve) than a two-equation model.
- Gas model showed good agreement with literature.

Chapter 5

Aerothermal Analysis of Re-entry and Landing Boost

The important aspects for the preliminary design of the thermal protection systems consist in determining the peak heat loads and the integral heating along the re-entry trajectory. This chapter presents the numerical methodology and the results from the supersonic retro-propulsion simulations of the returning first stage together with the final landing boost. The focus is thereby on linking the flow phenomena to the wall heat flux distribution of the first stage. Additionally, the modeling drawbacks are briefly summarized.

5.1 Trajectory

As discussed in the introduction, the general approach of the DLR retro-propulsion con-

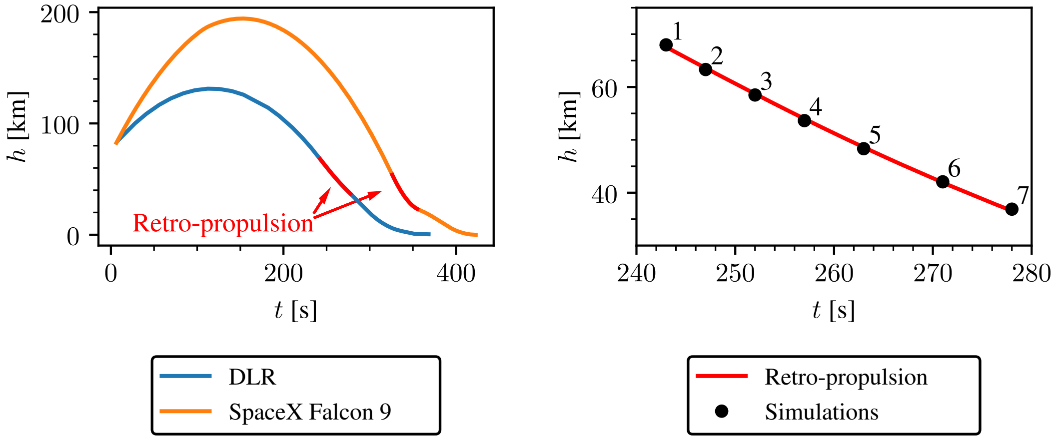

(a) Comparision of SpaceX Falcon 9 and DLR trajectories after stage separation.

(b) Supersonic retro-propulsion trajectory of DLR configuration with simulation points.

Figure 5.1. Re-entry trajectories of SpaceX Falcon 9 and DLR retro-propulsion configuration [12, 9].

figuration and SpaceX Falcon 9 are similar concerning the overall launch profile. As discussed in the introduction, the general approach of the DLR retro-propulsion configuration and SpaceX Falcon 9 are similar concerning the overall launch profile. However, the re-entry trajectories differ in altitude and the region, in which the re-entry burn is conducted as contrasted in figure 5.1a. The DLR first stage has a significantly lower peak altitude (130 km) than Falcon 9 (200 km) and starts the re-entry retro-propulsion maneuver at around 70 km compared to the 50 km of Falcon 9. Both maneuvers take around 30 s.

The DLR retro-propulsion maneuver decelerates the first stage from $M = 9.45$ to 5.09. The trajectory is modeled as seven discrete points, at which a steady flow state was assumed. The re-entry burn trajectory and the simulation points are shown in figure 5.1b. The corresponding atmospheric conditions are introduced in table 5.1. Point 8 refers to the retro-boost at the landing and is therefore not indicated in the supersonic retro-propulsion trajectory.

Traj. point	t [s]	h [km]	M	$Re \times 10^5$	p_∞ [Pa]	T_∞ [K]	ρ_∞ [kg/m^3]
1 (Start SRP)	243	68.0	9.45	0.212	6.32	223.05	$9.87 \cdot 10^{-5}$
2	247	63.3	8.73	0.361	12.7	236.21	$1.88 \cdot 10^{-4}$
3	252	58.5	8.0	0.595	25	249.65	$3.49 \cdot 10^{-4}$
4	257	53.6	7.27	0.952	48	263.37	$6.35 \cdot 10^{-4}$
5	263	48.3	6.54	1.604	94.1	270.65	$1.21 \cdot 10^{-3}$
6	271	42.1	5.82	3.456	209	256.93	$2.84 \cdot 10^{-3}$
7 (End SRP)	278	36.9	5.09	6.461	426	242.37	$6.13 \cdot 10^{-3}$
8 (Landing)	368	$5.1 \cdot 10^{-3}$	$1 \cdot 10^{-4}$	0	$1.01 \cdot 10^5$	288.15	1.22

Table 5.1. Freestream boundary conditions at retro-propulsion trajectory points.

5.2 Numerical Methodology and Boundary Conditions

The methodology of the RANS simulations is based on the procedures of Ecker et al. [12] and Dumont et al. [9]. First the numerical setup in TAU is described, followed by the gas model for the rocket exhaust gas and surrounding air. Finally, the boundary conditions of the computational domain along the retro-propulsion trajectory are specified.

5.2.1 Numerical Setup in DLR TAU

The SRP flowfield along the retro-propulsion trajectory was simulated on seven discrete points (see figure 5.1), assuming a steady flowfield at each point. Therefore, all simulations were performed using the steady RANS approach on a hybrid structured/unstructured grid provided by [9] (see figure 5.3). For turbulence modeling the Spalart-Allmaras one-equation model [57] was used. The AUSMDV flux vector splitting scheme was applied together with the MUSCL gradient reconstruction to achieve second order spatial accuracy [9].

The simulations were considered sufficiently converged, when the density residual was smaller than 10^{-4} and the flowfield did not change any longer in time [68]. A further criterion was the convergence of the heat flow rate [69].

5.2.2 Thermodynamics and Gas Modeling

In the context of the preliminary design study of the DLR retro-propulsion approach, the transport and thermodynamic gas property description were modeled for the exhaust gas mixture and air. The exhaust gas flow in the nozzle was simulated separately and introduced as a Dirichlet boundary condition to the retro-propulsion flowfield simulations.

Thermodynamics

The exhaust gas from the first stage and the surrounding air, as well as their mixture are modeled as non-reacting (frozen), thermally perfect gases. Thus, the gases follow the perfect gas law and their properties (e.g. c_p, c_v, energy and enthalpy) are a function of the temperature only. The gas properties necessary for the modeling in TAU (c_p, enthalpy) are derived from the CEA thermodynamic and transport database [55]. All gases are modeled as mixtures by applying the Wilke mixture rules to the components [12].

By assuming a frozen flow all occurring chemical and non-equilibrium effects are ignored. In return, a frozen flow assures a fast and robust convergence of the RANS simulations, which was desired in the preliminary design study.

Rocket Exhaust Gas Modeling

The exhaust gas modeling process follows the procedure introduced by the previous DLR studies on the retro-propulsion configurations [12, 9]. The propellant combination of LH2 and LOx and the combustion chamber parameters for the first stage were set in the study by Dumont et al. [9]. This study by Dumont uses a 200 K higher total combustion chamber temperature (3900 K) than the present investigation (3700 K). However, since the trajectory and other vehicle data are coincident, the results of [9] are used to extend the present study. The combustion chamber configuration of [9] is labeled as "A". The configuration of the present study as "B". An overview over the parameters is given in table 5.2.

Configuration	p_t [bar]	T_t [K]	ρ_t [kg/m^3]
A	120	3900	5.5
B	120	3700	5.9

Table 5.2. Engine parameters of configurations A and B [9].

The engine exhaust gas is model as a equilibrium mixture of gaseous O_2 and H_2 with mixture ratio of 5.8 at combustion chamber conditions of B. The relevant properties of the O_2-H_2 mixture at these conditions are extracted from CEA [55]. After exiting the combustion chamber the exhaust gas is expanded isentropically to the nozzle throat using

Cantera [70]. At the throat, the exhaust gas is composed of the following species:

Species i	H_2	H	O	O_2	OH	H_2O	HO_2	H_2O_2
w_i [%]	2.29	0.196	0.615	2.04	6.53	88.3	$1.53 \cdot 10^{-2}$	$4.37 \cdot 10^{-3}$

Table 5.3. Exhaust gas composition at nozzle throat in mass fractions w_i [9]

This gas composition is then used to create a thermally perfect pseudo gas. This pseudo gas is applied to the separate calculations of the nozzle flow and to simulations of the retro-propulsion flowfield [9].

Nozzle Flow Simulations

The thermally perfect and frozen exhaust engine flow was simulated in a 2D axisymmetric converging-diverging nozzle (figure 5.2a). The nozzle is 2.3 m long and has a exit diameter of 1.3 m. All chemical and non-equilibrium effects happening while expanding the flow through the nozzle are ignored. The simulations were performed using the identical numerical setup in TAU as for the first stage's retro-propulsion flowfield simulations (section 5.2.1). The following boundary conditions were set:

- Nozzle inlet flow set to the combustion chamber conditions (cf. table 5.2)
- Nozzle wall as viscous and isothermal at 1000 K
- Nozzle outflow, i.e. exit plane, to 0.7 bar (ideal expansion)

The evolution of Mach number, temperature and pressure along the nozzle are illustrated in figure 5.2. Both simulations of configurations A (lower half) and B (upper half) are displayed. The flowfields do not differ significantly in Mach number or pressure. The temperature evolution shows the biggest difference, resulting in a 130 K lower averaged exit temperature for B, i.e. 1450 K. The exit velocity and temperature profiles of B are shown in figure 5.2d and an overview of the averaged flow properties at the exit is given in table 5.4. A further implication of the reduced combustion chamber temperature is a 3 % reduced specific impulse I_sp of B compared to A. The effect on the nozzle thrust, however, is small.

Configuration	$\overline{M}_\mathrm{exit}$	$\overline{T}_\mathrm{exit}$ [K]	$\overline{p}_\mathrm{exit}$ [bar]	$\dot{m}$ [kg/s]	I_sp [s]	$I_\mathrm{sp,vac}$ [s]
A	3.75	1580	0.60	336	372	401
B	3.77	1450	0.59	347	360	387

Table 5.4. Averaged flowfield properties at nozzle exit of configurations A and B [9].

The nozzle flow exit profile is extracted and applied to the first stage retro-propulsion flow simulations. The exit profile is imposed as a Dirichlet boundary condition to the active first stage's nozzle exit planes (red planes in figure 5.3).

This nozzle flow simulation was conducted by my supervisor Tobias Ecker.

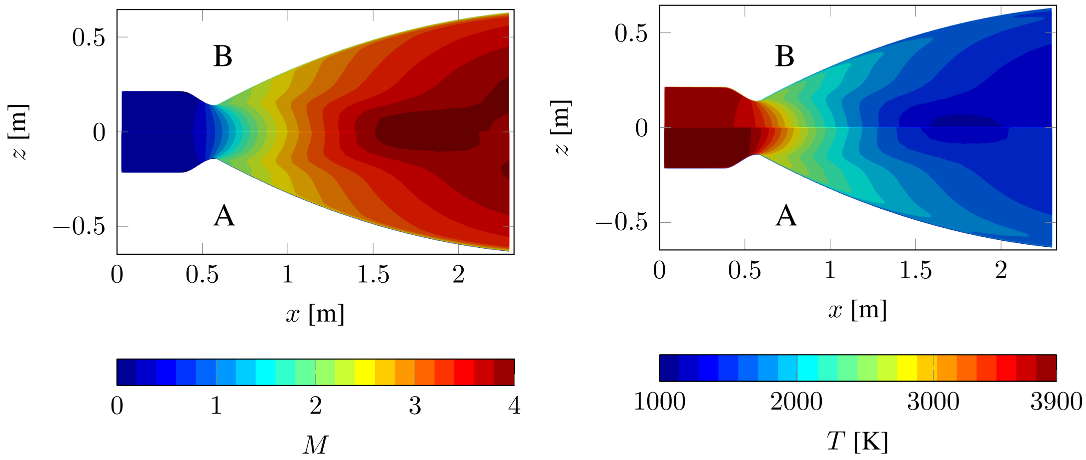

(a) Mach number; B top, A bottom. **(b)** Flow temperature; B top, A bottom.

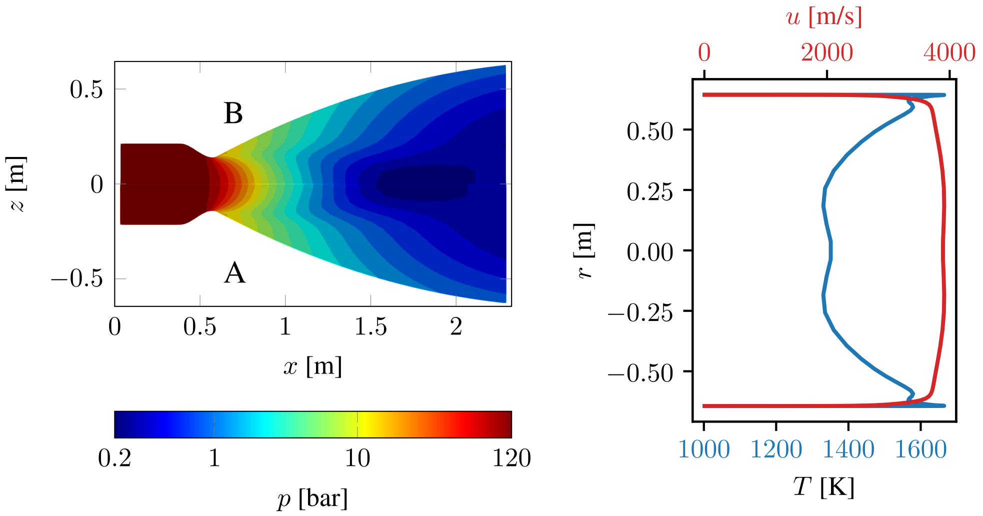

(c) Flow pressure; B top, A bottom. **(d)** Exit profile configuration B.

Figure 5.2. Nozzle flow parameters of engine configurations A (bottom) and B (top).

Air Modeling

The air for the atmospheric re-entry flow is also modeled as a thermally, frozen perfect gas. The properties are derived from CEA [55]. The constant composition is given below in table 5.5:

Species i	N_2	O_2	Ar	CO_2
w_{i} [%]	78.08	20.95	0.93	0.04

Table 5.5. Air composition in mass fractions w_{i} [9].

Computational Domain and Boundary Conditions

For the simulations the computational domain was chosen to be a quarter (i.e. 90°) segment of the actual first stage (grid generated by [9]). An extract of the domain is presented in figure 5.3. The domain consists of a hybrid (structured sidewall grid, rest unstructured) grid with 3 million points. The grid dimensions are 1.5 km in streamwise (x) direction and 300 m in the lateral directions y and z. The x-z and x-y edge planes of the domain are set to mirror planes in order to account for the remaining 270° degrees of the first stage. The atmospheric conditions of table 5.1 are set as the freestream (farfield) boundary conditions. All walls of the first stage are defined as viscous walls. The wall heat flux is calculated via the Fourier law. The red planes in figure 5.3 indicate the active engines during the SRP maneuver, to which the nozzle exit profiles from the 2D nozzle simulation were applied as Dirichlet boundary conditions. The remaining nozzles are closed by applying a viscous wall boundary condition to their exit planes. For the generation of the heat flux database two simulations per trajectory point are necessary. For these two simulations the first stage's walls were set to uniform temperatures (isothermal wall) of 300 K and 400 K respectively (details in section 6.1.1).

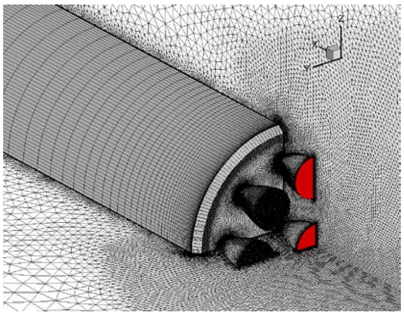

Figure 5.3. Detail of computational domain. Red planes indicate ignited engines [9].

An overview of the considered heat fluxes to the first stage, as well as the activated engines and flow angles is given in figure 5.4.

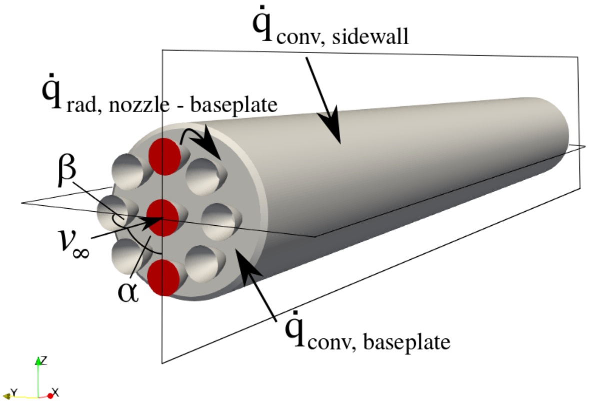

Figure 5.4. Considered heat fluxes and flow angles during the SRP maneuver.

5.3 Supersonic Retro-Propulsion during Re-entry

The heat fluxes from the SRP flowfield to the vehicle walls along the given retro-propulsion trajectory points (cf. figure 5.1b) are presented in this section. Different possible influences on the flowfield were investigated and are summarized in table 5.6: The trajectory point (1B - 7B, i.e. atmospheric density) and implications on the plume flows, the flow angle (7Baoa, 7Bya) and the effect of the two different combustion chamber conditions (comparison of A and B). Furthermore, the occurring heat fluxes when engines are switched off (1Off, 7Off) are examined, as well as thermal radiation from the nozzle walls to the baseplate (7Bnr). The nozzle wall temperature profile from Wang (cf. section 4.2) (7Bntp) was applied to asses modeling error from imposing uniform wall temperatures.

Trajectory point	Engines firing							Engines off
	A	B						
	by [9]	B	$\alpha = 5\,^\circ$	$\beta = 5\,^\circ$	Radiation	$T_{\mathrm{w,\,db}}$	T_{nozzle}	
1 (Start SRP)	1A	1B						1Off
2	2A	2B				2Bdbv		
3	3A	3B						
4	4A	4B				4Bdbv		
5	5A	5B						
6	6A	6B						
7 (End SRP)	7A	7B	7Baoa	7Bya	7Bnr	7Bdbv	7Bntp	7Off
8 (Landing)		8B						

Table 5.6. Conducted 3D simulations.

Note that in this section the colorbar for heat flux plots exploits the whole range of colors to display the findings and patterns more clearly. However, when it was possible the plots are scaled to uniform colorbars. Additionally, the three ignited engines are always displayed parallel to the centerline, (z axis) as indicated in figure 5.4.

An overview of the plume flowfield of the returning first stage at the beginning of the SRP maneuver (trajectory point 1) is indicated in figure 5.5. The plume contour is drawn at an exhaust gas mass fraction of $w_{\mathrm{exhaust}} = 0.6$. The three separate jets, exhausting from the nozzles, coalesce into one plume that expands unequally due to the three plumes interacting with each other (see paragraph "Plume-Plume Interaction" in 5.3.2). The bow shock and barrel shock are indicated in gray scale via div$\vec{v}$. The streamlines originate from the nozzles and freestream and are plotted to indicate the velocity field. Following the streamlines, the freestream is heated up by the bow shock from 223 K to 3700 K and deviates due to the opposing plume flow. The plume exhausts the nozzles at a temperature of approximately 1500 K. The plume temperature drops to around 200 K as the plume continues to expand (better visible in figure 5.11). Traversing the barrel shock and the Mach disk, the plume is heated up to 3700 K, depending on the shock strength. At the beginning of the breaking maneuver the atmospheric density is still low and the plume flow can expand up to several 100 m, fully immersing the first stage.

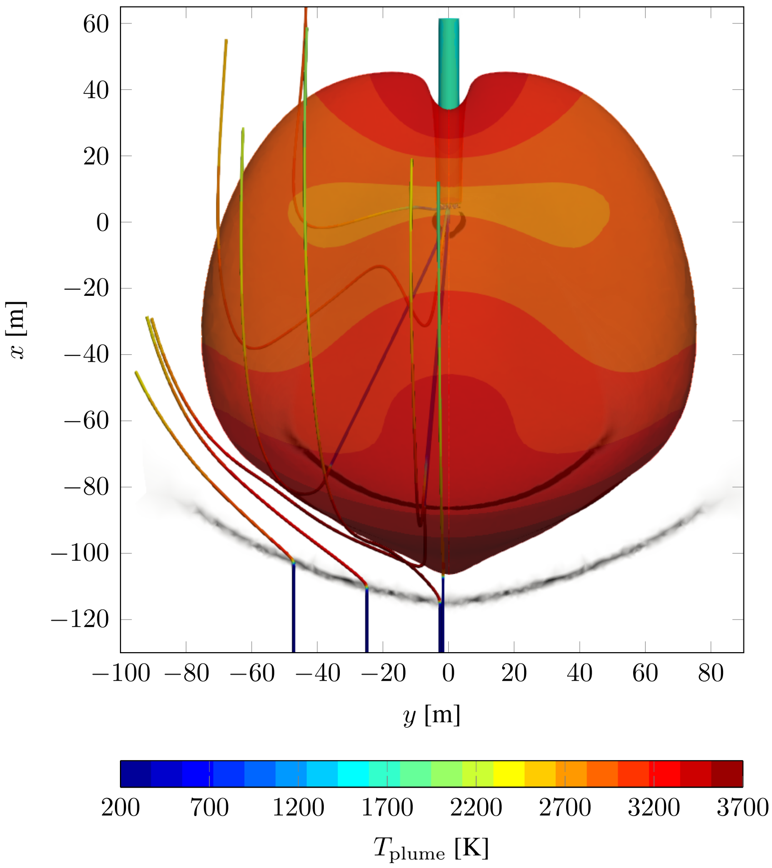

Figure 5.5. Start SRP (trajectory point 1): $T_\text{w} = 300$ K, $h = 68$ km, $M = 9.45$. Plume contour at exhaust mass fraction $w_{\text{exhaust}} = 0.6$ with streamlines and vehicle wall colored in T_{plume}. Shocks indicated via div$\vec{v}$ in gray scale. Streamlines originate from freestream and nozzle exits. Active engines along z axis (normal to viewing plane).

5.3.1 Along the Retro-propulsion Trajectory (1B - 7B)

This section gives an overview of the plume flow dimensions and evolution along the retro-propulsion trajectory.

The development along the seven points of the retro-propulsion trajectory is illustrated in figure 5.6. As mentioned previously, the high altitude allows the plume to expand strongly. As the first stage descends, the denser atmosphere causes the plume to contract and retract to the aft of the first stage. Thus, the plume size reduces significantly from about 100 m to several 10 m, allowing the shocks to move closer to the vehicle. The gas temperature near the vehicle's sidewall follows the plume retraction and increases with decreasing altitude. The area of highest surface gas temperature (light green at the beginning $\approx 1700K$, yellow at the end $\approx 2200K$) moves to the aft of the vehicle and changes position. The area of highest temperatures moves from parallel to the active engines (z axis) at the beginning to perpendicular to the active engines (y axis) at the end.

The complete immersion of the first stage in its plume is illustrated in figure 5.7. The contour of $w_{\text{exhaust}} = 0.3$ represents the contact surface between the bow shock and the

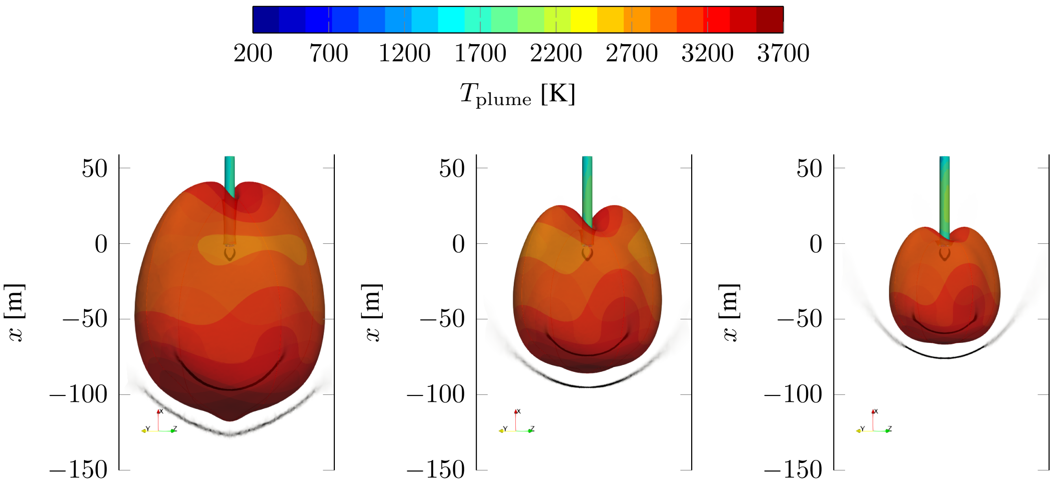

(a) Trajectory point 1 **(b)** Trajectory point 2 **(c)** Trajectory point 3

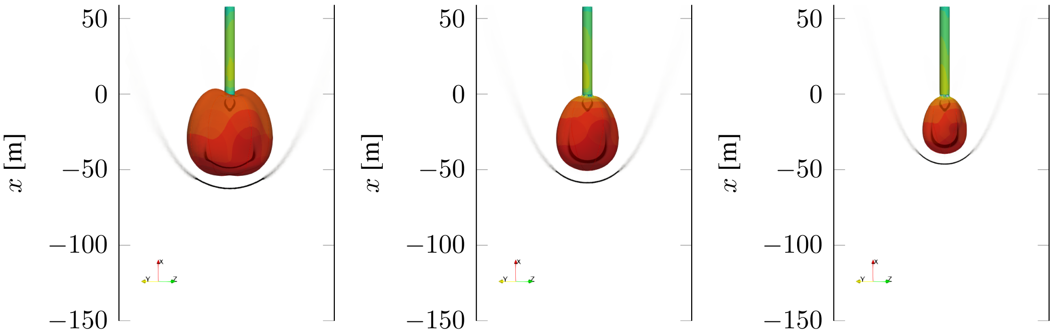

(d) Trajectory point 4 **(e)** Trajectory point 5 **(f)** Trajectory point 6

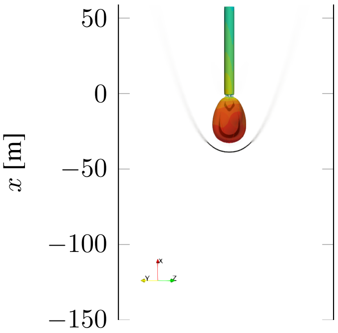

(g) Trajectory point 7

Figure 5.6. Evolution of supersonic retro-propulsion plume flow along trajectory for exhaust mass fraction $w_{\text{exhaust}} = 0.6$. Active engines along z axis (green).

opposing plume flow. The contraction of the plume is clearly discernible, ranging from a complete immersion of the first stage to only partly coverage at the end of the trajectory.

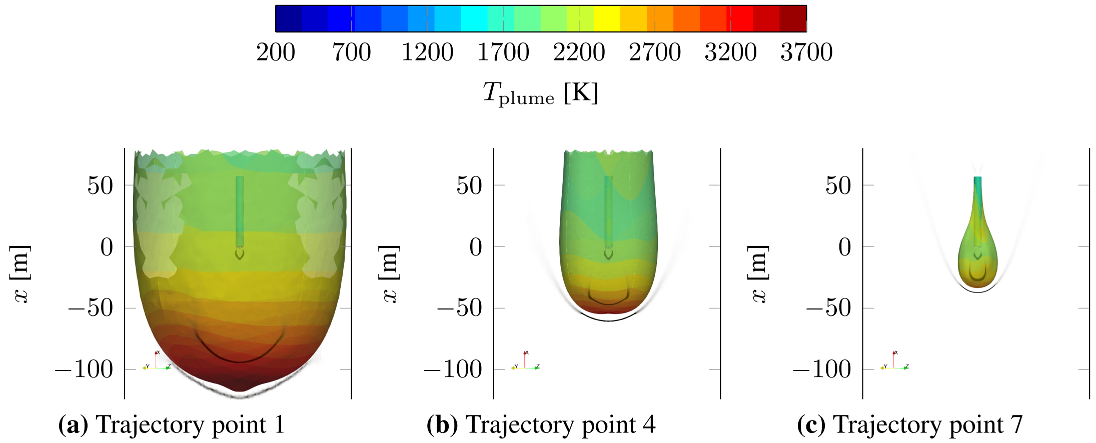

(a) Trajectory point 1 **(b)** Trajectory point 4 **(c)** Trajectory point 7

Figure 5.7. Evolution of supersonic retro-propulsion plume flow along trajectory for exhaust mass fraction $w_{\text{exhaust}} = 0.3$. Active engines along z axis (green).

5.3.2 Plume Interaction

The phenomena of the interacting plumes exiting from the three nozzles and their coalescence into one plume are described in this section.

Plume-Plume Interaction

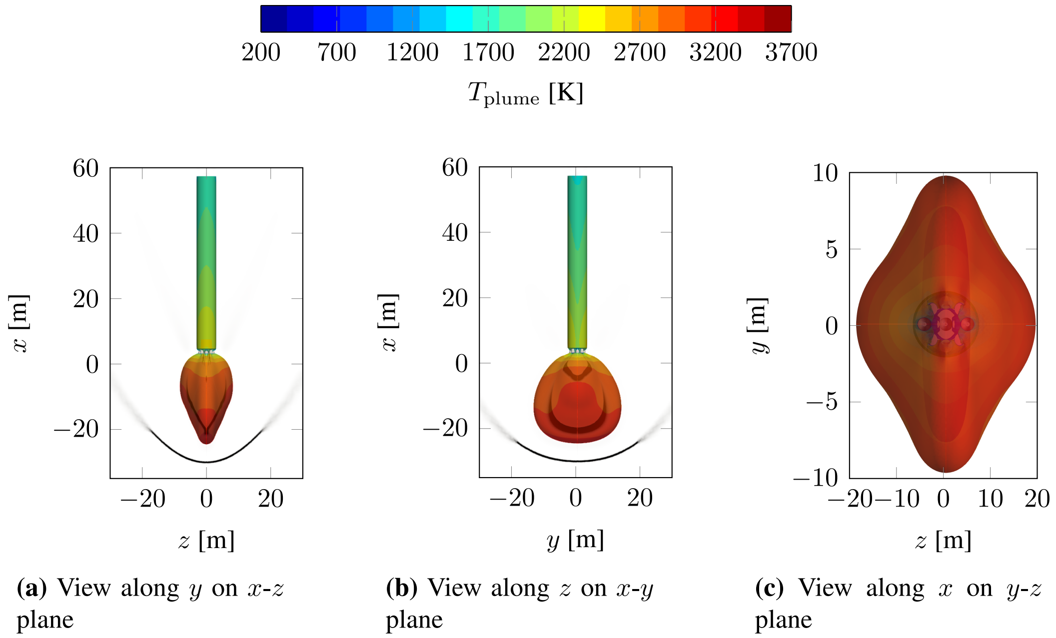

(a) View along y on x-z plane **(b)** View along z on x-y plane **(c)** View along x on y-z plane

Figure 5.8. Varying plume shape due to active engines along z axis (trajectory point 7, $T_{\text{w}} = 400$ K, $h = 37$ km, $M = 5.09$): plume contour at $w_{\text{exhaust}} = 0.6$. Plume and vehicle wall colored with T_{plume}. Shocks indicated via div$\vec{v}$ in grey scale .

Due to the in-line position of the three igniting engines, the plume flow expands unevenly, as shown in figure 5.8. The plume at trajectory point 7 is chosen as an example in figure 5.8, but the observations hold for the other trajectory points as well. The view on the x, z plane in figure 5.8a is parallel to the ignited engines. The plume and bow shock taper compared to the x, y plane, which is perpendicular to the ignited engines. In this plane, shown in figure 5.9b, the plume and shock are much broader. The view from the bottom up along the stage in figure 5.8c, shows the overall shape of the plume. The reason for this particular shape lies in the interacting plumes exhausting from the three nozzles (cf. sections 2.2.1, 2.2.3). They form oblique shocks on impingement as shown in gray scale in figure 5.9 (faintly in left figure). At the beginning of the SRP maneuver, when the atmosphere is thin, the plume expands past the shocks and accelerates up to $M = 12$ (figure 5.9a). Whereas at the end of the SRP trajectory, the plume is so contracted that the

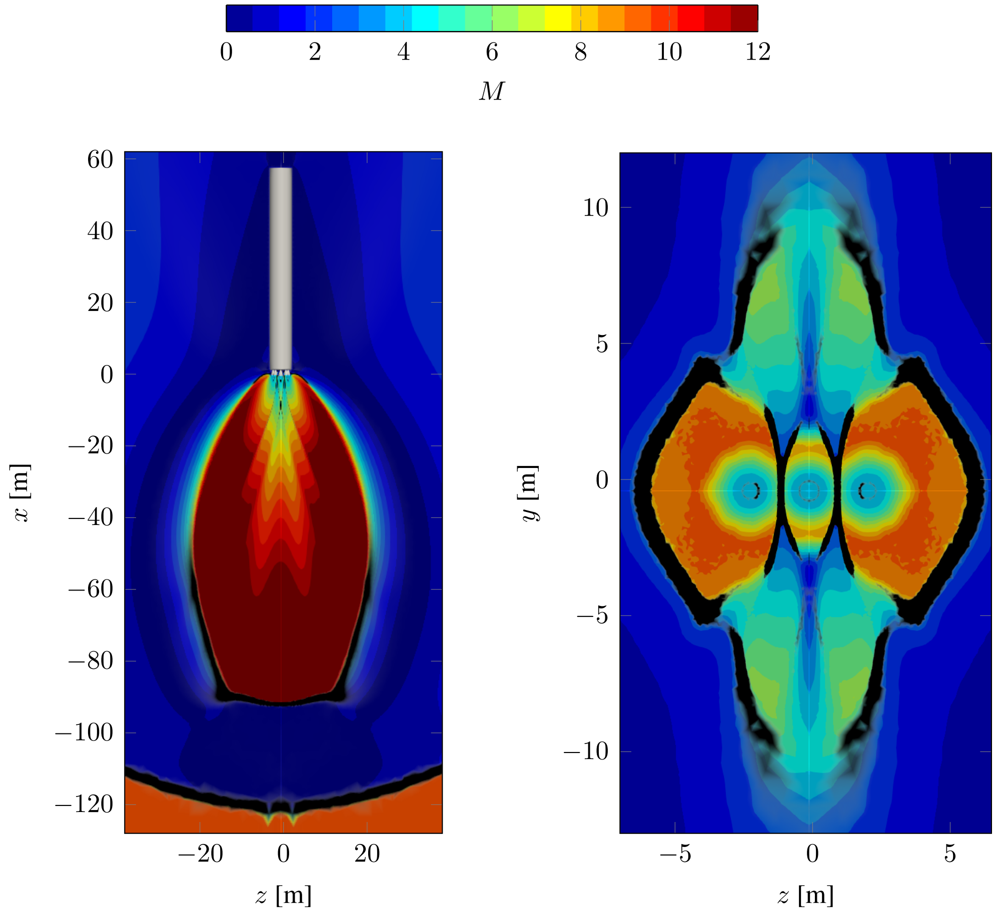

(a) M contours with shocks in gray scale.

(b) Plume interactions shocks and M contours 0.5 m downstream of nozzle exit at trajectory point 1.

Figure 5.9. Mach number distribution of plume-plume interaction at trajectory point 1 ($T_\mathrm{w} = 300$, $h = 68$ km, $M = 9.45$) with cut plane through plume 2 m downstream of the baseplate. Shocks indicated in grey scale.

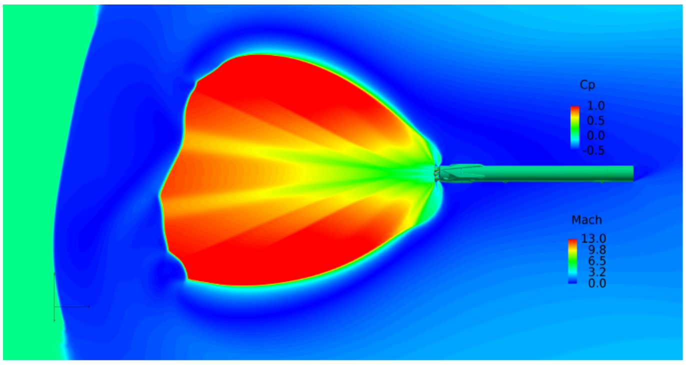

Figure 5.10. OVERFLOW sample pressure coefficient on surface and Mach number contours [46].

oblique shocks hit the barrel shock and the plume reaches only $M = 9$. The center plume is confined between the plumes of the outer nozzles as illustrated in figure 5.9a. The two outer plumes expand to their respective side parallel to the z axis. The center plume, however is likely to expand sideways parallel to the y axis over the interaction shocks, creating the bulge in y direction. This shape is also depicted in the exhaust contours in figure 5.8c.

The plume-plume interaction of the three ignited nozzles was also captured by Edquist et al. [46]. They compared several different flow solver results to flight data from SpaceX Falcon 9 to calibrate their computational methods. Unfortunately, they do not provide any information on boundary conditions or explicit results. Therefore, the comparison is only qualitatively. Figure 5.10 shows a URANS solution of OVERFLOW-solver. The plume flow within the barrel shock displays a similar behavior to the plume flow of the steady RANS simulations in figure 5.9a: The plumes form shocks on impingement and accelerate until reaching the barrel shock. The bow shock is displaced further upstream and adapts to the effective obstruction surface of the plume and the vehicle. Even though the boundary conditions are different in both simulations the general flowfield structure is captured similarly.

Plume-Surface Interaction

Having examined the plume flow structure, the investigation continues with the wall heat flux resulting from the interaction between the plume flow and the first stage's sidewall and baseplate.

Sidewall During the SRP maneuver the oncoming freestream forces the plume to flow back around the first stage. The overview plot of the SRP flowfield phenomena (figure 2.10) is now presented in figure 5.11 with color indications of w_{exhaust} and T_{plume}. The bow and barrel shock are characterized by the temperature jumps from around 200 K to over 3000 K in the flowfield. The freestream is heated over the bow shock up to 3700 K in the center and to over 2000 K on the sides. The plume exits the nozzles at a temperature of around 1600 K and continues to expand until 200 K. Depending on the

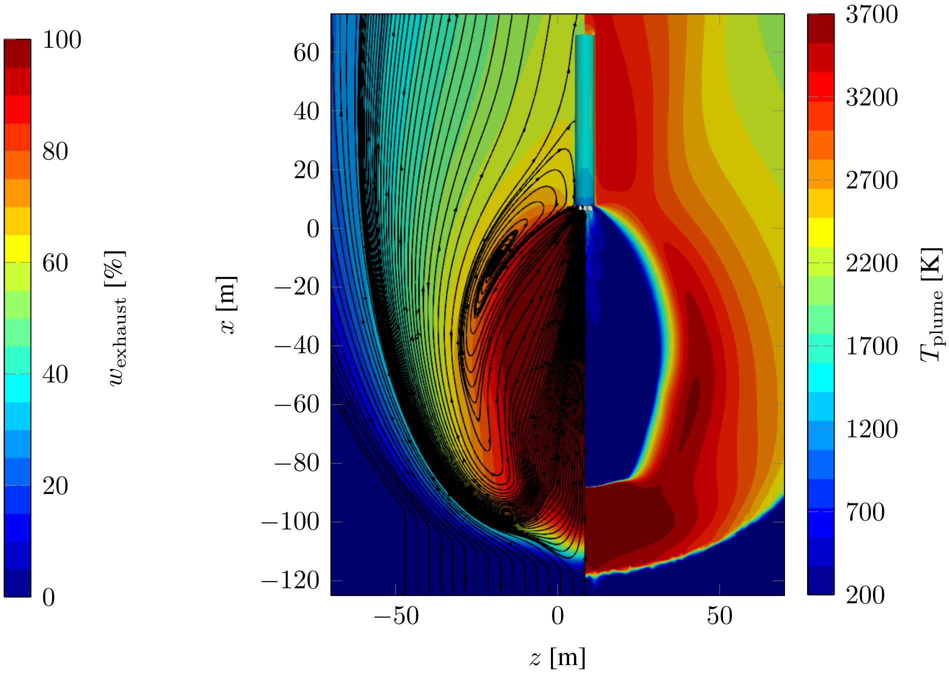

Figure 5.11. Nozzle streamline evolution at trajectory point 1: $T_{\text{w}} = 300$ K, $h = 68$ km, $M = 9.45$; left: w_{exhaust}; right: T_{plume}. Active engines along z axis

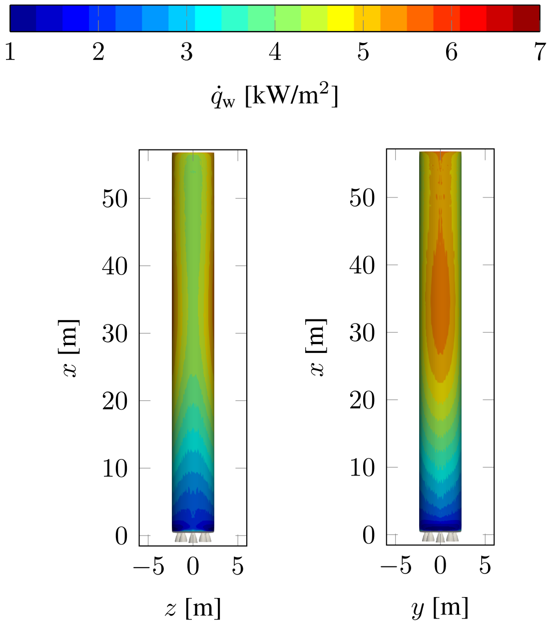

(a) View from figure 5.11

(b) View (a) rotated by 90°.

Figure 5.12. Sidewall heat flux due to plume flow impingement (stagnation area colored in orange) at trajectory point 1: $T_{\text{w}} = 300$ K, $h = 68$ km, $M = 9.45$; active engines along z axis.

nozzle, the plume either traverses the Mach Disk and is heated to around 3700 K or the barrel shock, where it reaches around 3200 K. The flow is forced to turn by the oncoming freestream and parts of it form the recirculation area, which impinges on the sidewall center, transporting hot gas to the sidewall surface (left). This leads to an increased convective heat flux to the walls in the area of impingement (cf. figure 5.12). Furthermore, the exhaust mass fraction on the right indicates the gradual mixing of the exhaust gas with the freestream air.

The resulting wall heat fluxes are depicted in figure 5.12. The varying distribution of the wall heat fluxes is clearly visible, suggesting that the recirculating plume does not impinge homogeneously on the sidewall, but only on parts of it. Figure 5.12b is the by 90° rotated view, which shows the heat fluxes from the recirculation zone (orange) more clearly. The highest heat fluxes are discovered at the edge connecting baseplate and sidewall. They are not necessary physical due to modeling issues on sharp corners or edges [68]. In general, the heat fluxes at the beginning of the breaking maneuver are low compared to heat fluxes as the first stage descends to denser atmosphere levels (cf. figure 5.14). Due to the thin atmosphere at this trajectory point the heat transport to the wall is still limited.

The plume flowfield at the end of the retro-propulsion trajectory is illustrated in figure 5.13. The plume is now significantly smaller and forms a different recirculation area spanning along the entire barrel shock. Its impingement could not be captured in this view, since it is in the x, y plane perpendicular to the current view. But the gas temperatures at the surface and the whole flow structure suggest, that the recirculating flow impinges near the aft of the body in the plane perpendicular to the active engines.

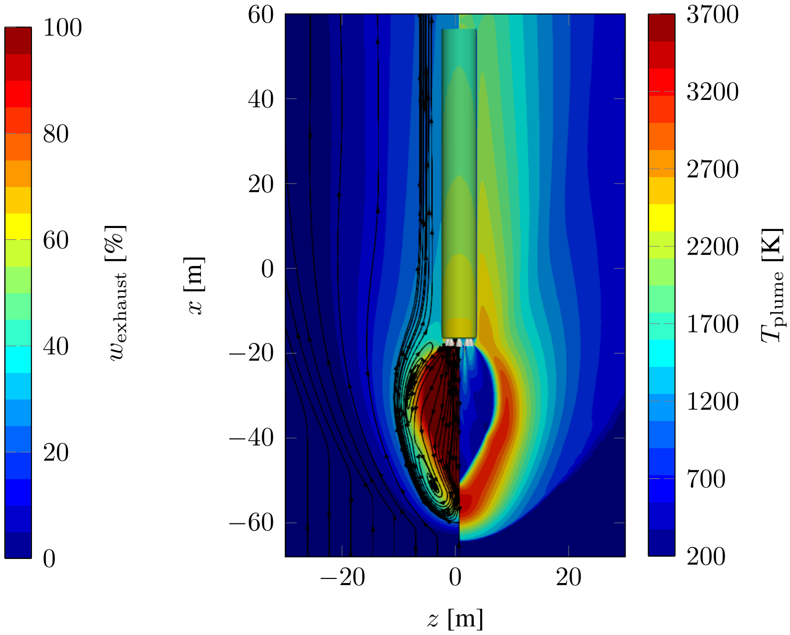

Figure 5.13. Nozzle streamline evolution; left: w_{exhaust}; right: T_{plume}; trajectory point 7: $T_{\mathrm{W}} = 400$ K, $h = 37$ km, $M = 5.09$; active engines along z axis.

The sidewall wall heat flux distribution in figure 5.14 reflects the above described phenomena. At the end of the breaking maneuver the impinging recirculation flow has moved up to 90° in circumferential direction compared to the beginning of the maneuver. This is likely caused by the contraction of the plume and thus the different development of the shear layer and recirculation area. Furthermore, the heat loads have tripled along the trajectory due to the denser atmosphere. Therefore the compression i.e. heating processes occur much closer to the walls. The maximums loads still appear at the edge between baseplate and sidewall.

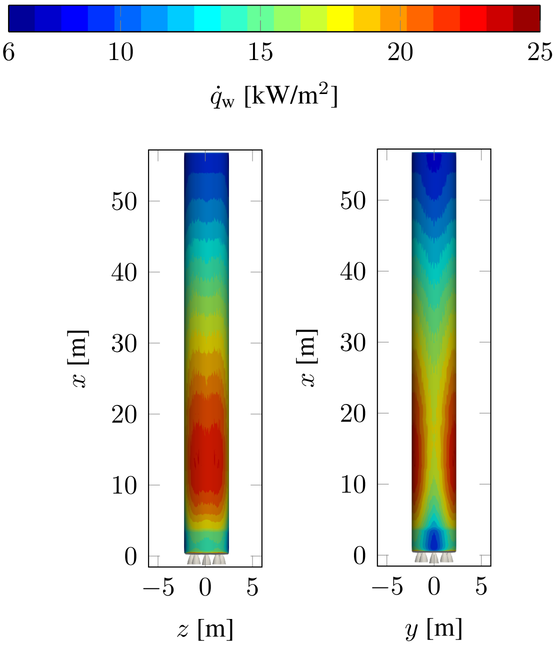

(a) View from figure 5.13

(b) View (a) rotated by 90°.

Figure 5.14. Sidewall heat flux due to plume flow impingement (stagnation area colored in orange) trajectory point 7: $T_\mathrm{w} = 400$ K, $h = 37$ km, $M = 5.09$; active engines along z axis.

Baseplate The heat flux to the baseplate strongly depends on the interacting plumes and thus on the nozzle pressure ratio. The plume flow impinging on the baseplate at trajectory point 1 is depicted in figure 5.15a. The same presentation mode is chosen as for the sidewall flowfield plots: the exhaust mass fraction on the left and the flowfield temperature on the right. The black lines indicate the streamlines from the active nozzles. The plume interaction shock is indicated by the temperature jump, where the streamlines from the two nozzles impinge on each other. The flowfield strongly suggests that the flow near the nozzle walls, i.e. the boundary layer flow, does not have enough energy to overcome the plume interaction shock and is forced to turn towards the baseplate, forming a base-impinging jet. The jet impinging on the base concentrates around the center nozzle and forms a recirculation area. From there it turns radially outward between the engines and re-accelerates and expands to ambient pressure forming a vortex tube. The exhaust mass fraction on the left shows the high level of under-expansion: The flow at the outer nozzle wall is bent over 90° towards the base, as the red color for 100 % exhaust indicates and the very faintly visible streamlines on the right. Thus, the nozzle pressure ratio is high enough, that the base-impinging plume jet has reached chocked conditions. The baseplate heat flux distributions in figure 6.5 suggests the same since the wall heat flux does not change over the first three trajectory points.

The baseplate heat flux is illustrated in figure 5.15b. The maximum heating occurs around the center nozzle where the plume impinges. The four distinct spots of maximum heat flux could be caused by uniting flow, accelerating outwards between the nozzles. The peak base heat flux is almost three times higher than the maximum sidewall heat flux.

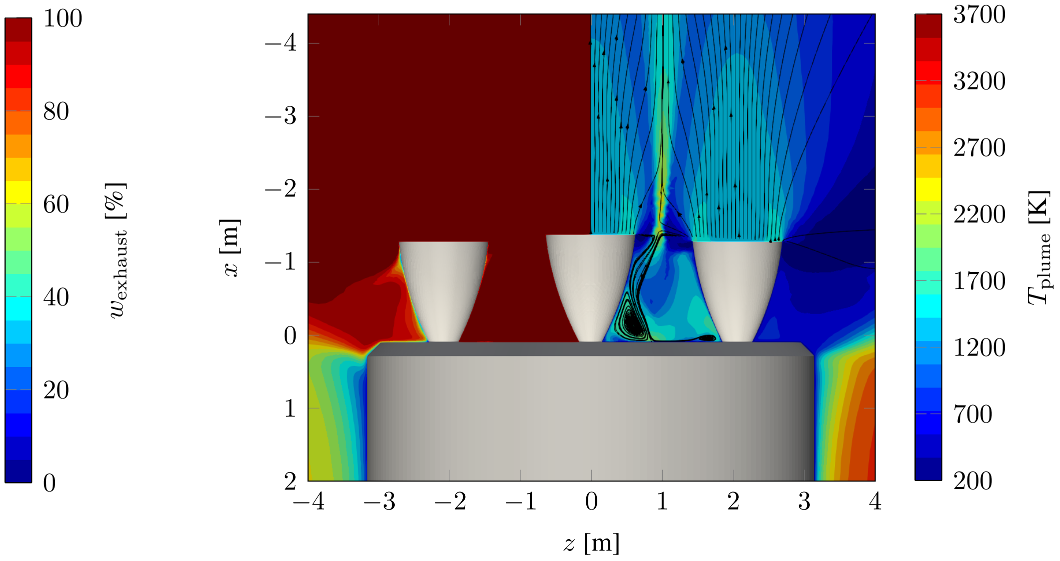

(a) Impinging plume on the baseplate (plume flow direction in $-x$). View on x, z plane at $y = 0$. Left: w_{exhaust}; right: T_{plume}. Active engines along z axis.

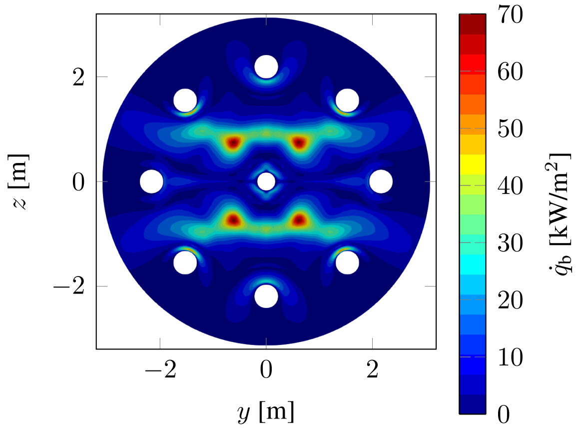

(b) Baseplate heat flux distribution, active engines along z centerline

Figure 5.15. Base plate heat flux due to impinging plume flow at trajectory point 1: $T_{\mathrm{w}} = 300$ K, $h = 68$ km, $M = 9.45$. Active engines along z axis.

With decreasing altitude along the retro-propulsion trajectory, the nozzle pressure ratio decreases. Thus, the plume expansion and therefore the interaction shocks become weaker compared to the beginning of the maneuver, as seen in figure 5.16. Here, the plume flowfield around the nozzles at the end of the breaking maneuver is shown. The exhaust mass fraction on the left still indicates an highly over-expanded flow, but now the flow at the outer nozzle walls is not bent over 90°, as the outer streamlines on the right suggest as well. The plume flow that is not able to traverse the plume interaction shock is significantly reduced compared to the beginning of the SRP maneuver in figure 5.15a. Thus, the impinging flow on the baseplate has left the choked conditions, leading to a

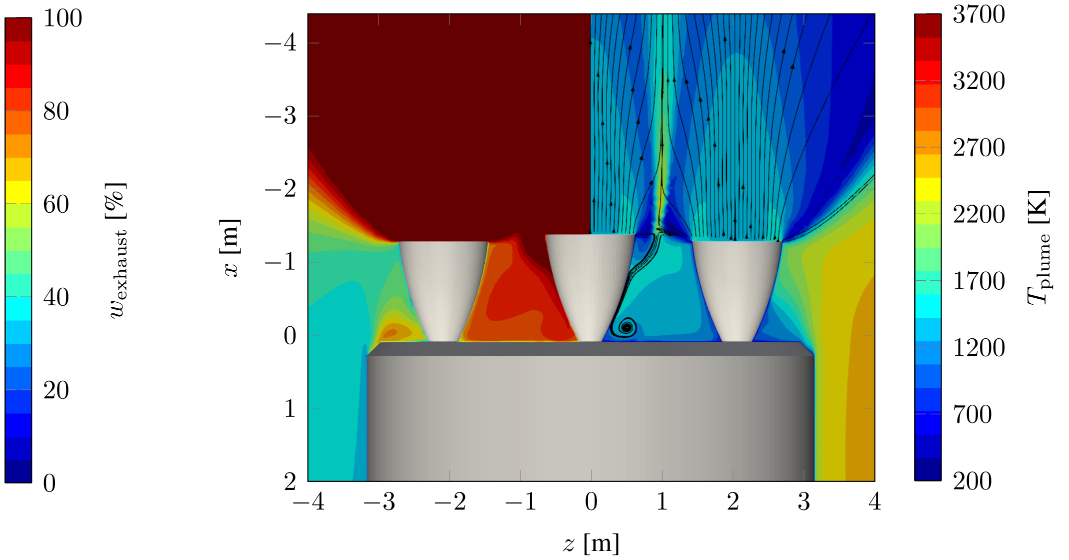

(a) Impinging plume on the baseplate. View on x-z plane at $y = 0$. Left: w_{exhaust}; right: T_{plume}. Active engines along z axis.

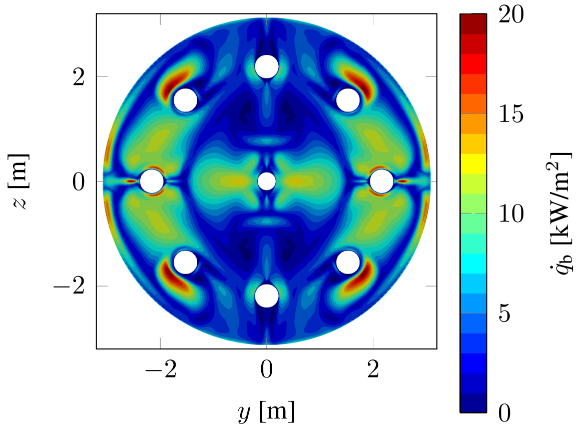

(b) Baseplate heat flux distribution, active engines along z centerline

Figure 5.16. Baseplate heat flux due to impinging plume flow at trajectory point 7: $T_{\text{w}} = 400$ K, $h = 37$ km, $M = 5.09$.

weaker impinging plume jet on the base and therefore a reduced heat flux to the baseplate. This is clearly visible in figure 5.16b where the maximum heating is only a third of the one observed in the beginning of the SRP maneuver. The base flow has changed its pattern. When re-accelerating towards the ambient pressure, it heats the baseplate more uniformly. The flow now concentrates at the outward facing nozzle walls causing the maximum heating there.

Examining the beginning and end of the retro-propulsion trajectory shows that the plume flowfield significantly influences the heat fluxes to the sidewall and baseplate. The sidewall is mostly affected by the impinging plume from the recirculation zone and the baseplate by the impinging plume jet. The evolution of the wall heat fluxes along the SRP maneuver is investigated in section 6.2.

5.3.3 Flow Angles (7aoa, 7ya)

The flow angle influence on the development of the plume flowfield were undertaken only at the end of the SRP trajectory (trajectory point 7). The angles are indicated in figure 5.4.

Angle of attack $\alpha = 5°$ (7aoa)

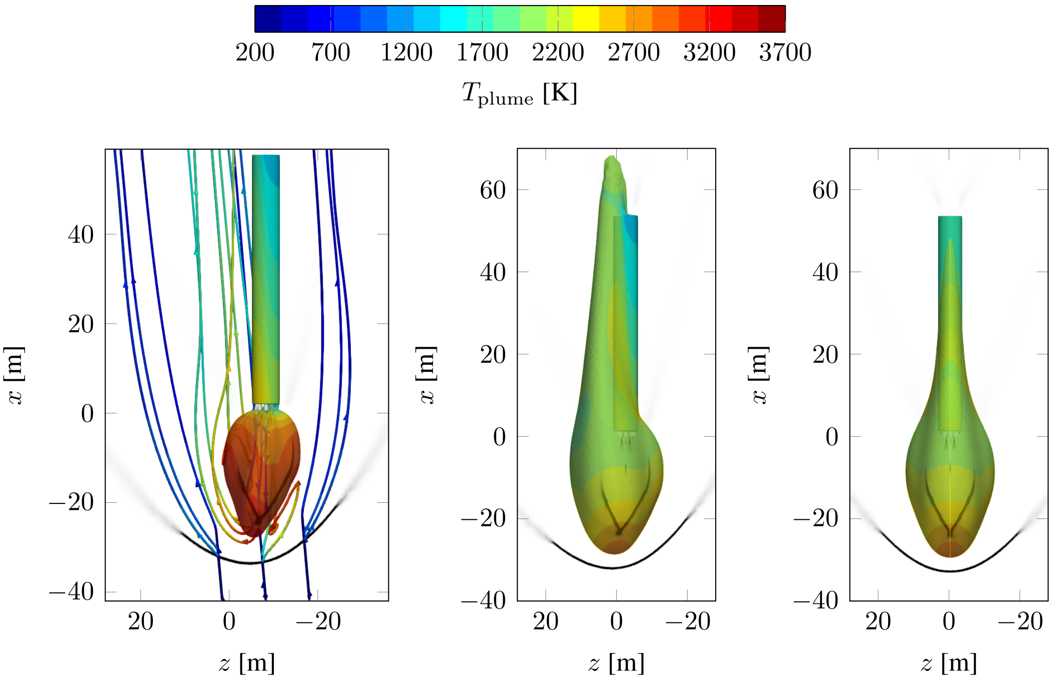

(a) Flowfield overview of $\alpha = 5°$. First stage sees freestream coming from left. Plume contour at $w_{\text{exhaust}} = 0.6$.

(b) $\alpha = 5°$, first stage sees freestream coming from left. Plume contour at $w_{\text{exhaust}} = 0.3$.

(c) $\alpha = 0°$. Plume contour at $w_{\text{exhaust}} = 0.3$

Figure 5.17. Angle of attack flowfield and comparison of the plume isosurfaces at $w_{\text{exhaust}} = 0.3$ for $\alpha = 5°$ and $\alpha = 0°$ at trajectory point 7: $T_{\text{w}} = 400$ K, $h = 37$ km, $M = 5.09$.

If the freestream is not aligned with the vehicle axis, the plume gets pushed away from the attack side and concentrates on the lee side as shown in figure 5.17 for plume contours of $w_{\text{exhaust}} = 0.6$ and $w_{\text{exhaust}} = 0.3$. The first stages sees the freestream coming from left, i.e. from negative z directions , which lies in the active engines plane (x-z plane). Comparing the flowfield to zero angle of attack, the freestream deforms the shocks, pushing parts of the bow shock closer to the vehicle. The plume follows this deformation becoming highly asymmetric, particular visible in figure 5.17b. The flow asymmetry was also observed by Daso et al. [19]. This asymmetry is also observable in the flow temperature near the vehicle wall and thereby in the heat flux distribution. For example the upper right corner is exposed to cooler flow than it is the case without a flow angle.

The resulting wall heat fluxes are illustrated in figure 5.18. Compared to the case of zero angle of attack in figure 5.18d, the impingement of the recirculation zone has moved by 90° to the lee side of the first stage (x-z plane, figure 5.18a), leading to an increased heat flux there. Whereas the windward side, figure 5.18c experiences less heat flux than in the zero angle of attack case (around 10 % less). The maximum heat flux to the sidewall is approximately 20 % higher due to the concentration of the plume on the lee side.

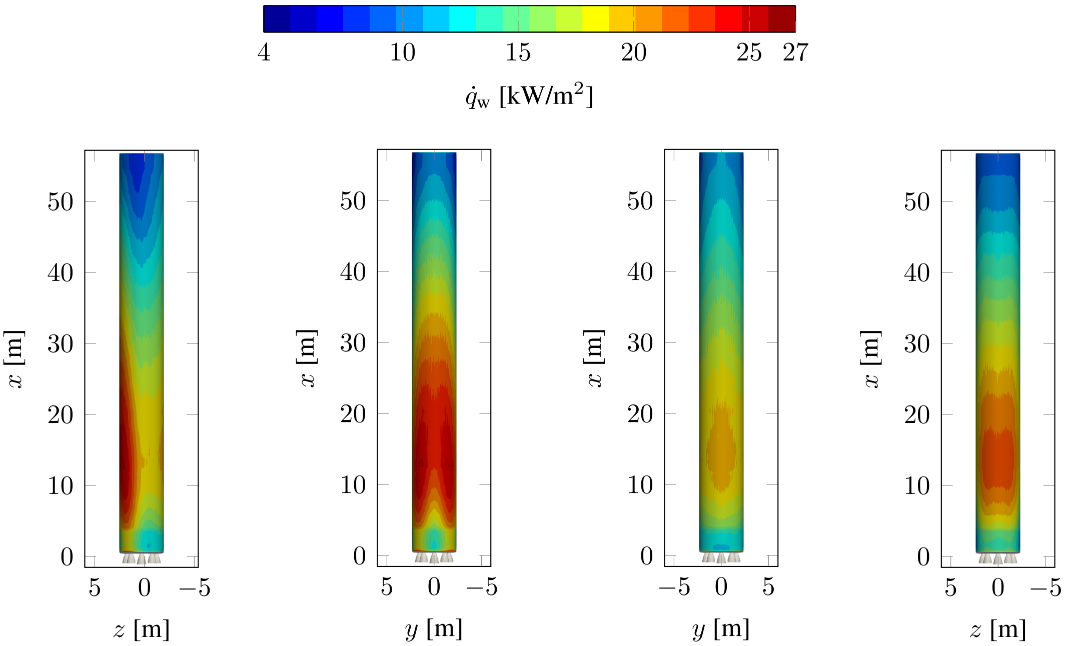

(a) View on x-z plane from figure 5.17b.

(b) View (a) rotated by 90°

(c) Backside of view (b).

(d) $\alpha = 0°$.

Figure 5.18. Sidewall heat flux for angle of attack $\alpha = 5°$, active engines along z, freestream from $-z$ direction and comparison with $\alpha = 0°$ at trajectory point 7: $T_w = 400$ K, $h = 37$ km, $M = 5.09$.

Yaw angle $\beta = 5°$ (7ya)

In the case of the yaw angle, the freestream is coming from the "side" as indicated in figure 5.4. The plume is deformed in the plane perpendicular to the engines as depicted in figure 5.19. This is the plane, where the plume spreads wider due to the central plume being forced to escape to the sides (figure 5.9b). However, the yaw angle causes the flowfield to evolve asymmetrically (as with the angle of attack). The plume at the windward side ($-y$ direction) is pushed closer to the vehicle wall (figure 5.19b), resulting in higher gas temperatures at the sidewall (bottom right of the vehicle in figure 5.19a).

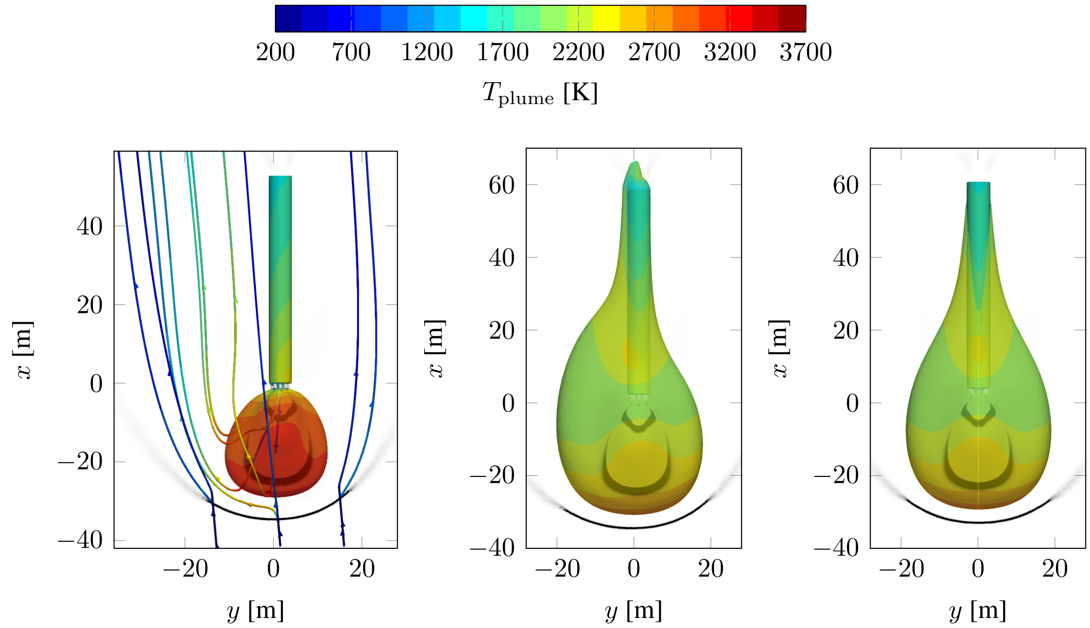

(a) Flowfield overview of $\beta = 5°$. First stage sees freestream coming from left. Plume contour at $w_{\text{exhaust}} = 0.6$.

(b) $\beta = 5°$, first stage sees freestream coming from left. Plume contour at $w_{\text{exhaust}} = 0.3$.

(c) $\beta = 0°$. Plume contour at $w_{\text{exhaust}} = 0.3$

Figure 5.19. Yaw angle flowfield and comparison of the plume isosurfaces at $w_{\text{exhaust}} = 0.3$ for $\beta = 5°$ and $\beta = 0°$ at trajectory point 7: $T_{\text{w}} = 400$ K, $h = 37$ km, $M = 5.09$.

The higher gas temperatures at the windward part of the sidewall lead to an increased heat flux as seen in figure 5.20a. Consequently, the yaw angle causes the opposite effect to the angle of attack: The windward side is exposed to higher heat loads. The angle of attack moved the hot plume to the lee side. Therefore, the maximum heating occurs in different planes depending on the flow angle.

For the yaw angle flow, the maximum heat flux is in the same plane as the one with zero angle, but about 20 % higher in magnitude (figure 5.20). Additionally, the area of maximum heat flux for the yaw angle is larger than in the angle of attack case (compare figures 5.18b and 5.20b) . The lee side of the first stage with yaw angle experiences a reduced heat flux of about 15 % (figure 5.20c) compared to the zero angle flow.

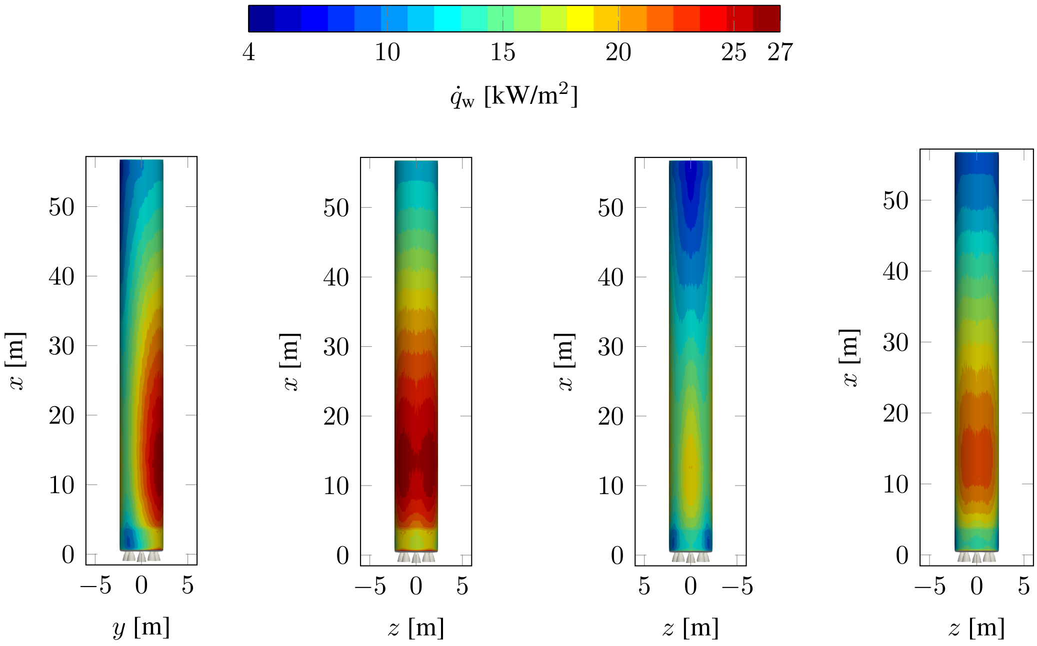

(a) View on x-y plane as in figure 5.19b.

(b) View (a) rotated by 90°

(c) Backside of view (b).

(d) $\beta = 0°$.

Figure 5.20. Sidewall heat flux for yaw angle $\beta = 5°$, active engines along z and comparison with $\beta = 0°$ at trajectory point 7: $T_\mathrm{w} = 400$ K, $h = 37$ km, $M = 5.09$.

Baseplate heat flux (7aoa, 7ya)

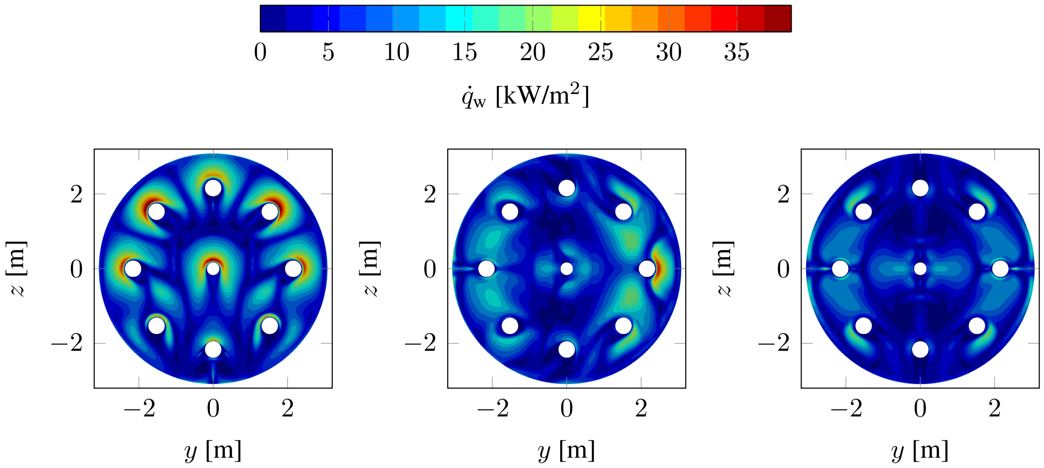

(a) $\alpha = 5°$ (flow is coming from bottom).

(b) $\beta = 5°$ (flow is coming from right)

(c) Zero flow angle

Figure 5.21. Baseplate heat flux of flow angles $\alpha = 5°$ and $\beta = 5°$ and zero flow angle at trajectory point 7: $T_\mathrm{w} = 400$ K, $h = 37$ km, $M = 5.09$. Active engines along z centerline

The baseplate heat fluxes for α, β and zero flow angle are compared in figure 5.21. The flow angles significantly effect the heat flux distribution compared to the zero angle in figure 5.21c: The heat flux to the baseplate doubled and its distribution follows the plume deformation due to the freestream. For the angle of attack in figure 5.21a, the plume is pushed along the baseplate by the freestream coming from the $-z$ direction. The maximum heat loads occur in the wake regions behind the nozzles, where the flow recirculates.

In the yaw angle case the in y direction expanding plume is forced closer to the vehicle by the freestream coming from positive y direction, thus leading to an increased heating at the windward side. This is especially true near the outer nozzle which is exposed to the oncoming plume. In contrast to the angle of attack, the lee side of the yaw angle is less affected by the freestream.

5.3.4 Combustion Chamber Parameters (Comparison of A and B)

The simulations of the returning first stage were conducted with two different total temperatures for the combustion process (table 5.2). This thesis used configuration B for the simulations. Comparing the nozzle exit profiles in figure 5.2 showed different exit temperatures (cf. also table 5.4). To examine whether the combustion temperature influences the occurring heat loads on the walls, the heat flux ratios of configuration A and B, $\dot{q}_{\mathrm{w,A}}/\dot{q}_{\mathrm{w,B}}$, of the sidewall and baseplate are compared for trajectory point 1 (figure 5.22).

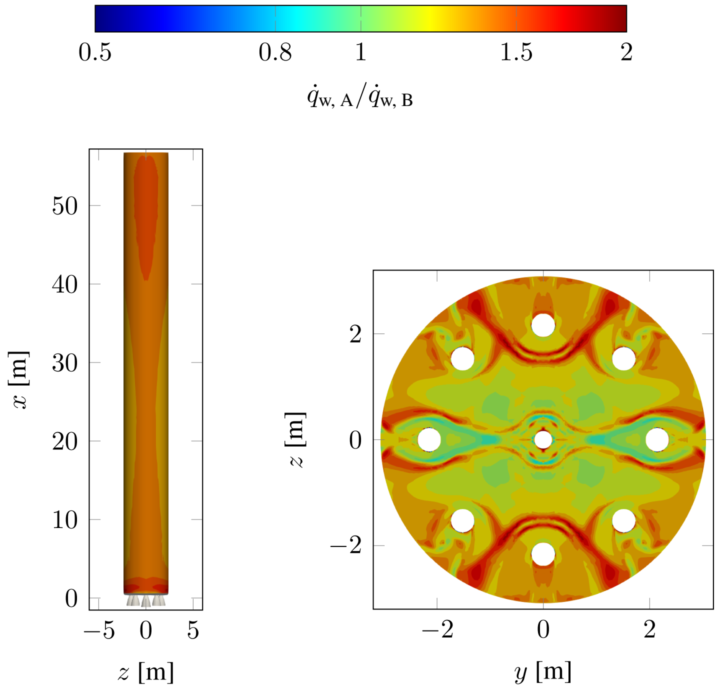

(a) Sidewall.
(b) Baseplate.

Figure 5.22. Sidewall and baseplate heat flux ratios for configurations A and B $\dot{q}_{\mathrm{w,\,A}}/\dot{q}_{\mathrm{w,\,B}}$ at trajectory point 1: $T_{\mathrm{w}} = 300$ K, $h = 68$ km, $M = 9.45$; active engines along z axis.

The heat flux ratio for the sidewall in figure 5.22a suggest an overall higher heat flux to the sidewall at configuration A (between 20 and 70 % higher than B), due to higher plume temperatures. The heat flux of A at the edge between the baseplate and sidewall is by 50 % smaller than B. This must be considered with caution due to the modeling issues at sharp corners. The highest difference between A and B occurs at the aft and the top of the stage. The difference at the aft is believed to come from the higher plume temperature at the nozzle exit. The maximum at the top of the stage suggests, that the impinging plume from the recirculation area extends further around and up along the stage and is hotter, thus leading to higher wall heat fluxes.

The ratio at the baseplate supports the assumption that the impinging plume jet is hotter at configuration A. The main impinging area around the central nozzle does not show a significant increase, due to the choked base flow on impinging. But the radial outflow between the nozzles shows higher wall heat fluxes for A.

5.3.5 Engines Deactivated (1Off, 7Off)

To get an idea of the heat loads to the first stage before the retro-propulsion maneuver starts and after the engines are switched off again, two simulations with deactivated engines were conducted at trajectory point 1 and 7. An overview of their flowfields is given in figure 5.23. Before the three engines are ignited at trajectory point 1, the first stage is

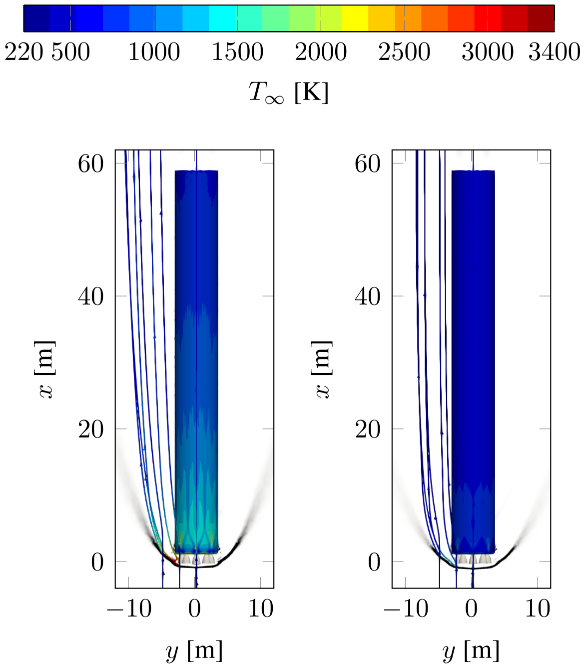

(a) Trajectory point 1 **(b)** Trajectory Point 7.

Figure 5.23. Flowfield of first stage before and after retro-propulsion, streamlines and vehicle wall colored in T_∞. Shock indicated via div$\vec{v}$ in gray scale. Streamlines originate from freestream.

flying with $M = 9.45$ at an altitude of $h = 68$ km. The bow shock forms directly in front of the nozzle, heating the freestream up to 3400 K, due to the high Mach number. Thus, the aft of the first stage sees most of the hot gas from the bow shock (figure 5.23a), particularly the sidewall area immediately after the edge. After the retro-propulsion maneuver, the first stage is decelerated to $M = 5.09$ at $h = 36.9$ km and the heating of the freestream over the shock is significantly reduced to 1400 K, therefore the gas temperature surrounding the first stage is also considerably lower (cf. figure 5.23b).

The heat flux ratio of the sidewall $\dot{q}_{\text{w, off}}/\dot{q}_{\text{w, on}}$ is presented in figure 5.24. It is clearly visible that the aft of the first stage is highly affected by hot freestream, that is heated over the shock. The wall heat fluxes at the aft of the first stage are up to eight times (respectively three times in figure 5.24b) higher than with ignited engines. The heat flux from the hot plume to the sidewall plays a role in the upper part of the first stage, where it is up to 90 % higher compared to deactivated engines, as seen in figure 5.24a. Thus, the hot plume is protecting the aft of the sidewall from the heated air over the shock, but in turn causes heating of the upper part of the first stage. However, the wall heat flux with ignited engines is small compared to the heat fluxes with deactivated engines.

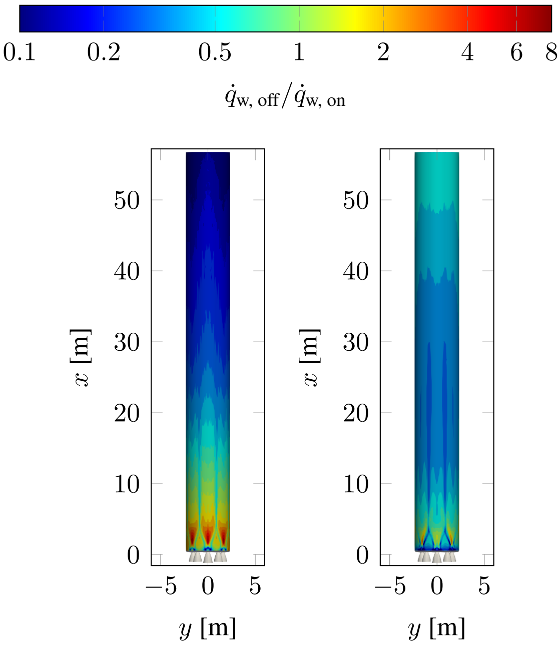

(a) Trajectory point 1

(b) Trajectory Point 7.

Figure 5.24. Heat flux ratio $\dot{q}_{\text{w, off}}/\dot{q}_{\text{w, on}}$ at sidewall before and after retro-propulsion.

At the end of the re-entry burn, the heat flux ratio has decreased and the freestream heating is reduced due to the significant deceleration of the vehicle (the plume wall heat flux however is increased at the end thus also contributing to the decreased ratio).

The heat flux ratio of the baseplate $\dot{q}_{\text{b, off}}/\dot{q}_{\text{b, on}}$ is illustrated in figure 5.25. At trajectory point 1 in figure 5.25a, the area around the central nozzle, where the hot plume jet is impinging and radially flowing out, sees a higher heat flux (up to 70 %) when the engines are firing, whereas the outer part is exposed up to a 100 times heat fluxes when the shock is directly sitting in front of the nozzles. Again, the heat flux from the impinging plume jet is negligible compared to the heated freestream impinging on the base. At the end at trajectory point 7 (figure 5.25b) the base heat flux from the heated freestream is dominating the base heating, thus the heat flux from the impinging plume jet is negligible all over the baseplate.

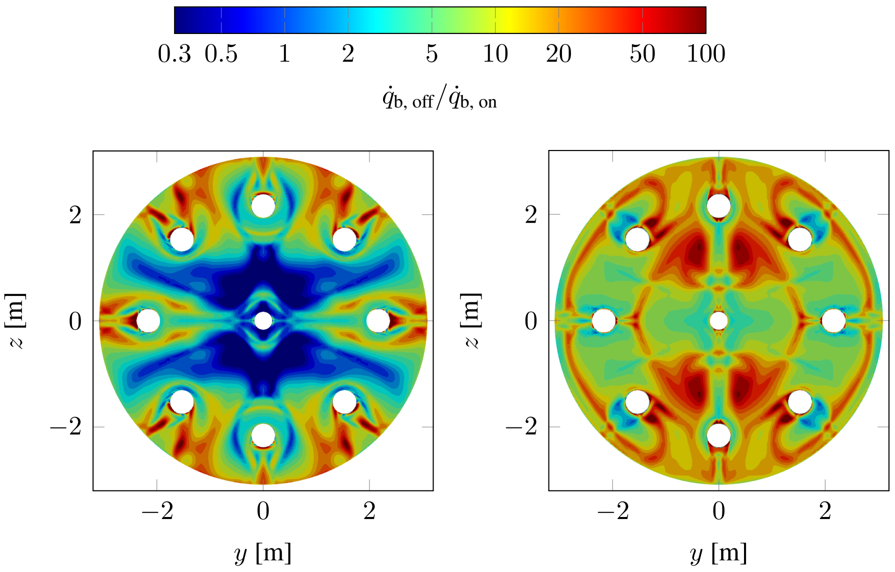

(a) Trajectory Point 1. **(b)** Trajectory Point 7.

Figure 5.25. Heat flux ratio $\dot{q}_{\text{b, off}}/\dot{q}_{\text{b, on}}$ at baseplate before and after retro-propulsion.

Table 5.7 shows the integral rate of heat flow to the first stage with activated and deactivated engines. At the beginning, when the engines are still switched off, the heat flux to the first stage is significantly elevated. However, the integral heat to the first stage is only half of the rate of the ignited engines. Thus, the hot plume flow protects the aft stage from the local heat flux peaks. The plume causes a redistribution of the heat fluxes with an increase in the upper part of the first stage.

	$\dot{Q}_{\text{w}}$ [MW]		
	Total	Sidewall	Baseplate
Trajectory point 1, engines off	2.9	2.4	**0.5**
Trajectory point 1, engines on	**5.0**	**4.8**	0.2
Trajectory point 7, engines off	8.9	7.5	**1.4**
Trajectory point 7, engines on	**18.4**	**18.2**	0.2

Table 5.7. Comparison of heat flow rates $\dot{Q}$ to sidewall and baseplate for trajectory points 1 and 7.

5.3.6 Thermal Nozzle Radiation (7Bnr)

The thermal radiation from the nozzle walls to the baseplate is investigated in this section. The gas radiation of the plume to the baseplate was not considered. Only the last trajectory point is considered, since there the convective heat flux to the baseplate is minimal. In order to estimate the thermal radiation from the nozzle walls to the baseplate, the temperature profile of Wang [67] (see figure 4.6b) was applied as nozzle wall temperature boundary condition to all nozzles of the quarter segment. The calculation of the radiative heat flux was done by the TAU-THETA radiation tool [64], which is also applicable for surface to surface radiation. Based on the emissivity of heavily oxidized aluminum $\epsilon = 0.31$ [71] the radiative heat flux to the baseplate is presented in figure 5.26a. The maximum radiative heat flux of 370 W/m^2 appears very close to the nozzle throats. This maximum is only 2 % of the maximum convective heat flux at trajectory point 7. Taking into account the distribution of the heat fluxes, the ratio of $\dot{q}_{\text{b, rad}}/\dot{q}_{\text{b, conv}}$ in figure 5.26b shows that the radiative heat flux at most reaches 20 % of the convective heat flux, thus being negligible for heating of the first stage. This becomes even more evident when comparing the convective and radiative heat rates from table 5.8. The radiative heat rate is by three orders of magnitude smaller than the convection rate. This stems also from the fact, that the baseplate is emitting radiation as it is indicated in dark blue in figure 5.26a. However, if we consider an $\epsilon = 1$ as a worst case scenario the radiative heat flux increases by an order of magnitude to around 3000 W/m^2, reaching values of up to $\dot{q}_{\text{b, rad}}/\dot{q}_{\text{b, conv}} = 3$ in the red indicated areas in figure 5.26b. Thus, the thermal radiation from the nozzle my be important to the base heating if either the nozzle material or the emissivity of the nozzle material changes or the nozzle temperature increases.

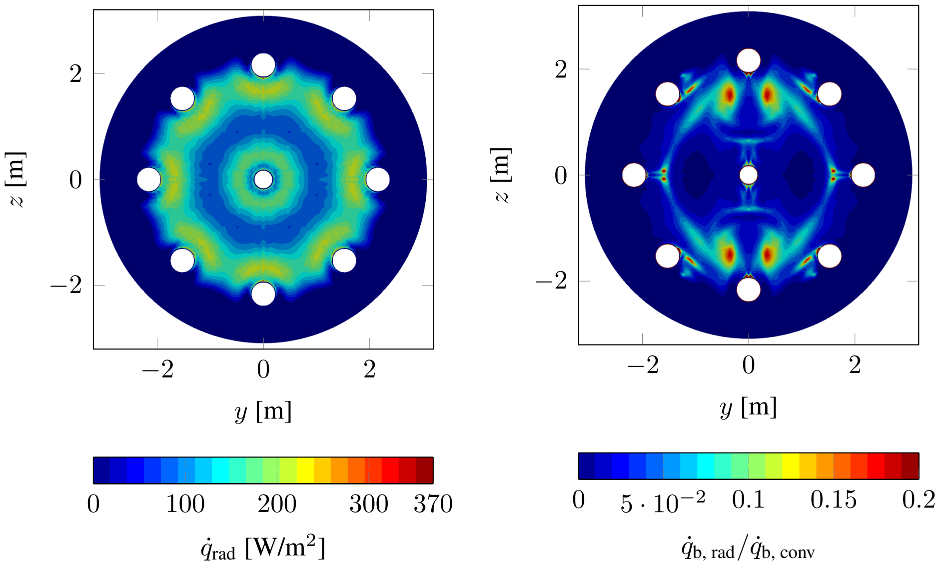

(a) Absolute heat flux values.

(b) Ratio of radiative to convective heat fluxes.

Figure 5.26. Overview of radiative heat flux from nozzle walls to baseplate at trajectory point 7 for $T_{\text{b}} = 400$ K.

	$\dot{Q}_\mathrm{b}$ [kW]
Radiation $\epsilon = 0.31$	$48 \cdot 10^{-2}$
Radiation $\epsilon = 1$	48.4
Convection	186

Table 5.8. Comparison of baseplate heat flow rate $\dot{Q}_\mathrm{b}$ for radiation and convection.

5.4 Landing Boost (8B)

The landing boost was simulated to get an idea of the impinging exhaust jet and plume distribution. One simulation was conducted with the central engine ignited, instants before the engine is switched off. Landing legs where not considered, but the distance between nozzle exit and ground was set to 5 m as if landing legs were attached, holding the first stage in place. The freestream boundary condition is set to sea-level static, cf. table 5.1. The evolution of the plume interacting with the ground is depicted in figure 5.27. The plume flowfield shows the behavior of a over-expanded impinging wall jet, with oblique, coalescing shock waves forming at the nozzle lip and a tail shock on impinging, as shown in figure 5.27a (faintly). The center plume ($w_\mathrm{exhaust} = 0.6$) reaches up to 3000 K on im-

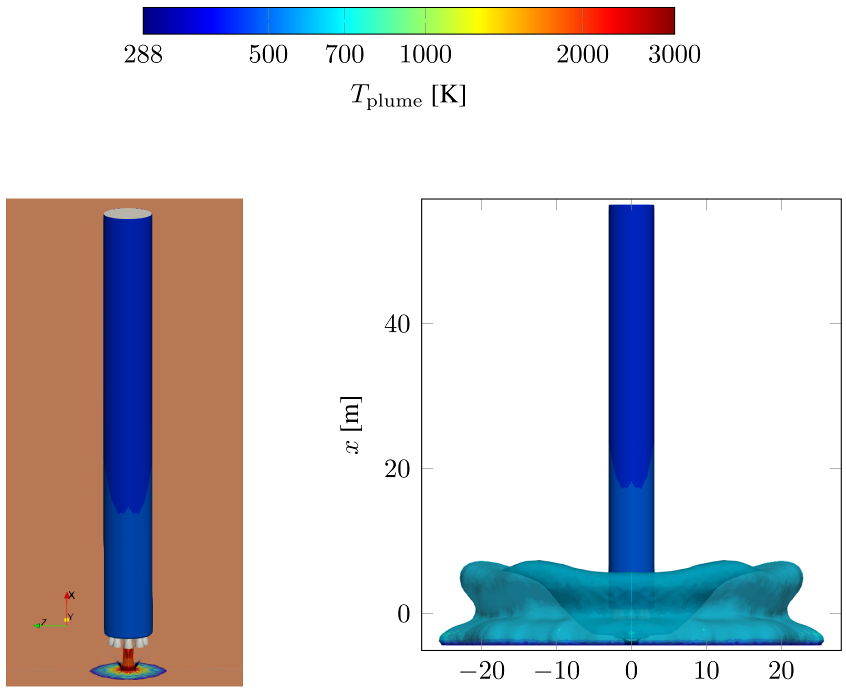

(a) Plume at $w_\mathrm{exhaust} = 0.6$.

(b) Plume at $w_\mathrm{exhaust} = 0.05$.

Figure 5.27. Plume temperature and extension during landing, only center engine active.

pinging. The plume continues to mix and extend up to 30 m circular around the first stage ($w_{\text{exhaust}} = 0.05$) still having a temperature of approximately 700 K (figure 5.27b). The first stage's sidewall is mildly affected by the hot plume: The lower part is exposed to near wall gas temperature of around 500 K leading to wall heat fluxes of maximum 10 W/m^2 (figure 5.28), whereas the baseplate is highly affected by the backflow of plume gases exiting the nozzle (figure 5.28b). Particularly, the area around the center nozzle sees the highest heat flux of 200 W/m^2. The heat flux distribution suggest that part of the plume exiting from the nozzle is reversed and impinges on the baseplate. After impingement, the hot gas flows out radially between the nozzles, leading to a second zone of increased heat flux in the wake region of the outer nozzles.

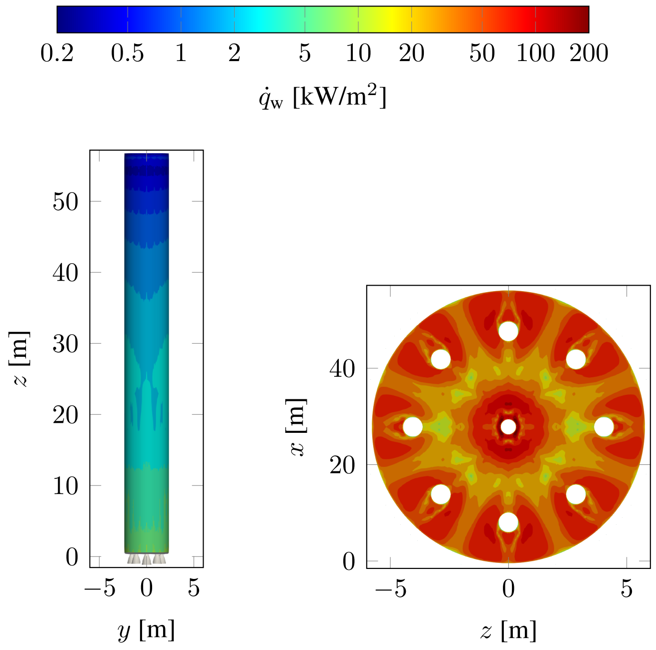

(a) Sidewall **(b)** Baseplate.

Figure 5.28. Wall heat fluxes at landing instants before engine shut down.

5.5 Modeling Drawbacks

As this study is part of the preliminary design process for evaluating the most efficient design approach for a re-usable first stage, simplifications and assumptions were made in order to minimize the computational efforts. Therefore, this section summarizes the major modeling assumptions and their implications.

5.5.1 Contiuum Mechanics at High Altitudes

The re-entry trajectory with SRP from 70 km to 36 km was completely simulated via the RANS approach using the continuum assumption. However, literature [56] suggests to use the continuum hypothesis for re-entry flows only up to 40 km and apply a slip wall boundary condition till 60 km due the decreasing density and thus particle number available for "property transport". The present re-entry with SRP does not represent a "classical" re-entry, but a re-entry where a high density exhaust plume interacts with the surrounding atmosphere. Due to the high plume density we are confident to maintain continuum mechanics near the stage at these altitudes. The Knudsen number calculation in appendix A supports the assumption as well.

5.5.2 Unsteady Flowfield

As indicated in the SRP literature section 2.2.3, the flowfield during retro-propulsion is highly unstable. Therefore, Ecker et al. [12] compared the flowfield properties of LES and RANS simulations of the first stage during the retro-boost maneuver. They concluded that RANS modeling is capable of sufficiently predicting the average flow properties near the first stage's sidewall. However, they did not assess the flowfield at the base of the first stage.

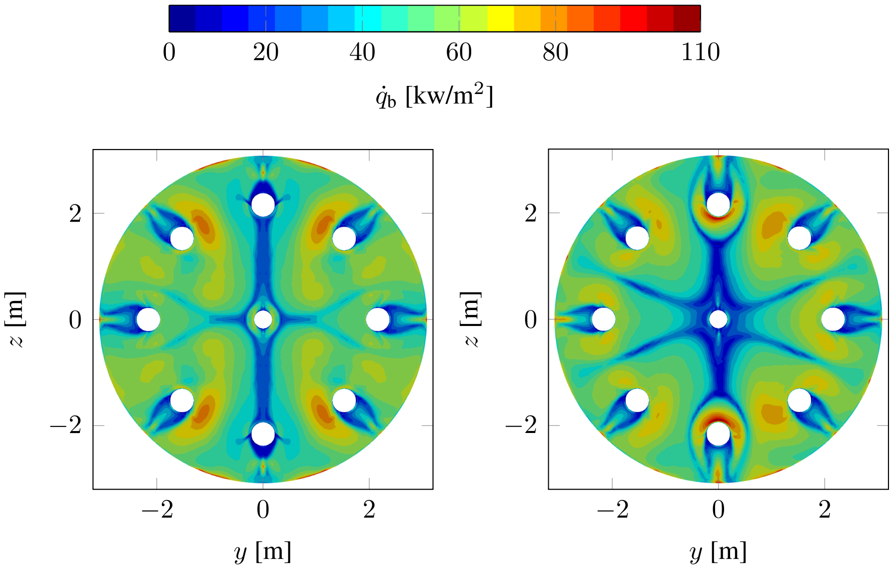

(a) Mirrored quarter segment.

(b) 360° simulation.

Figure 5.29. Comparison of baseplate heat fluxes for deactivated engines at trajectory point 7: $T_\mathrm{w} = 400$, $h = 37$ km, $M = 5.09$.

Aside from the SRP flowfield, the flowfield without retro-propulsion was found to be unstable in this simulation as well. When conducting the simulations for the deactivated engines, the resulting wall heat fluxes were expected to be axisymmetric (similar to figure 5.28b). However, particularly the baseplate showed a non-axisymmetric behavior as indicated in figure 5.29. Figure 5.29a showed deviations on the borders of the domain (which is the $+y$ and $+z$ axis). It was first assumed to be a grid-related or boundary condition issue, but after conducting a simulation with the full 360° computational domain, we concluded that the flowfield contains highly unsteady regions. The RANS simulation can only capture the averaged flow properties, which do not necessarily have to be symmetric in a highly unsteady flow [72]. During the SRP simulation the unsteadiness did not appear as prominent as with the deactivated engines, since the plume of the three in-line ignited engines causes a predominant direction of the flowfield.

However, the qualitative comparison of DLR first stage Mach number contours with NASA simulations of Falcon 9 in figures 5.9a and 5.10 shows that the major flow features are captured reasonably well.

5.5.3 Simplified Gas Model

Assuming the exhaust gases and mixture of exhaust gas and air to be thermally perfect and frozen is another simplification. The plume studies showed a qualitatively good agreement with experiments. However, calculating the exhaust nozzle flow as a reacting flow would lead to higher exit temperatures and thus to higher plume temperatures resulting in higher wall heat fluxes as studies from Ecker [73] suggest.

5.5.4 Temperature Profile at Nozzle Walls (7Bntp)

The first stage's wall temperature was set uniformly to 300 K and 400 K for the heat flux evaluation in the heat flux database. Since this is a huge simplification the error made by this simplification needs to be evaluated. Therefore, the heat flux from a more realistic temperature profile is compared to simulations with the 400 K uniform wall temperature. A simulation at trajectory point 7 is conducted, in which the (higher) nozzle wall temperature profile from Wang (figure 4.6b) is set as a Dirichlet boundary condition at the nozzle walls. The idea was to examine whether the heat flux increases, when the plume impinges on hotter nozzles and therefore looses less heat compared to the 400 K case.

The comparison of the wall heat fluxes showed no influence of the applied temperature profile on the resulting wall heat fluxes, neither on the sidewall nor on the baseplate.

5.6 Summery of Findings

It was found that the plume flow development along the retro-propulsion trajectory strongly influences the heat fluxes to the sidewall and baseplate. At the beginning of the trajectory the plume immerses the whole first stage and causes moderate heating on the upper part of the sidewall due to impinging flow from the recirculation area. The baseplate experiences a higher heat flux which is about ten times higher than the sidewall, caused by the impinging hot plume jet originating from the interacting plumes. The peak heat flux to the baseplate occurs around the center nozzle.

With decreasing altitude the plume contracts and retracts to the aft of the first stage. The heat flux to the sidewall triples and is concentrated at the lower part of the first stage. The area of impinging plume shifts from parallel to the active engines towards an area perpendicular to the active engines. In contrast to the increased heat flux on the sidewall, the baseplate heat flux reduces to a third of the heat flux at the beginning, due to weaker interactions of the plumes (level of plume under-expansion reduces with decreasing altitude). The maximum heat flux on the baseplate at this point originates from the radially outflowing plume and its interaction with the nozzle walls, thus the heat flux distribution becomes more evenly spread.

Investigations of an angle of attack and a yaw angle of 5 ° of the first stage revealed higher local heat fluxes on sidewall and baseplate due to the plume being "pushed" to the walls by the oncoming freestream flow. Thereby the direction from which the freestream is arriving with respect to the active engines plane plays a significant role in the heat flux distribution even at small flow angles. For the angle of attack, the lee side of the stage is more affected, in contrast to the yaw angle where the windward side experiences higher heat fluxes. The maximum sidewall heat flux is up to 20 % higher and the baseplate heat flux even doubled.

The comparison of combustion chamber configurations A and B revealed that a 5 % higher chamber temperature results in a higher plume temperature and thus in up to 70 % higher heat fluxes to the sidewall and more than two times higher heat fluxes at the baseplate.

Comparing the heat fluxes to the first stage's wall at ignited and deactivated engines, showed reduced heat fluxes to the aft of the first stage during SRP (especially the baseplate). However, the plume causes a higher overall heat rate to the wall, particularly to the upper part of the first stage.

Determining the thermal radiative heat flux from the nozzle walls to the baseplate showed a negligible contribution to the total wall heat flux for the applied material conditions.

Finally, the landing boost was examined, showing insignificant heat fluxes to the sidewall, but high loads to the baseplate. The plume impinging on the ground extends up to 60 m in diameter (at at $w_{\text{exhaust}} = 0.05$) having a temperature of around 700 K. These extension give an idea for safety and operation conditions at the landing site.

Chapter 6

Aerothermal Heating during the Supersonic Retro-propulsion Trajectory

Having evaluated the implications of the SRP flowfield on the wall heat fluxes in the previous chapter 5, the evolution of the thermal loads along the SRP trajectory in terms of design critical heat loads and heating is examined in this chapter.

From the simulated wall heat fluxes a database was constructed in order to estimate the heating over the retro-propulsion maneuver. Coupling the database together with a simple structural model gives the first stage's wall temperatures, as well as the integral heating over the entire retro-propulsion trajectory.

6.1 Coupling of Heat Flux Database with the Structural Model

The described procedure was introduced by two previous studies of the DLR, Ecker et al. [12] and Dumont et al. [9]. The studies estimated the wall heat flux evolution and the temperature rise of the sidewall of different first stage configurations over the retro-propulsion maneuver. The present study continues the work of Dumont et al. [9], who investigated the sidewall heat loads for engine conditions A of the DLR retro-propulsion configuration.

In this thesis the engine condition B is used for the simulations. The heat loads for condition B to the sidewall and baseplate are examined. Therefore this section shortly explains the generation of the heat flux database. Together with a basic structural coupling model, the wall heat fluxes are estimated along the retro-propulsion trajectory and the resulting wall temperatures of the first stage's sidewall and baseplate are calculated. Additionally, the database was validated with corresponding simulations and an overview of the database modeling simplifications is given.

6.1.1 Database generation

The idea of the database is to provide a computationally efficient and simple, as well as easily extendible procedure to estimate the evolution of the thermal loads along the retro-propulsion trajectory. Through the database the thermal loads can be evaluated independent of the simulations (i.e. no coupling of simulations with each other; no history effects considered). The simulations were conducted at the specific trajectory points, indicated in figure 6.1 with a prescribed set of boundary conditions (see table 5.1). The database is derived from the heat flux of these simulations and provides the heat fluxes for the whole 3D geometry.

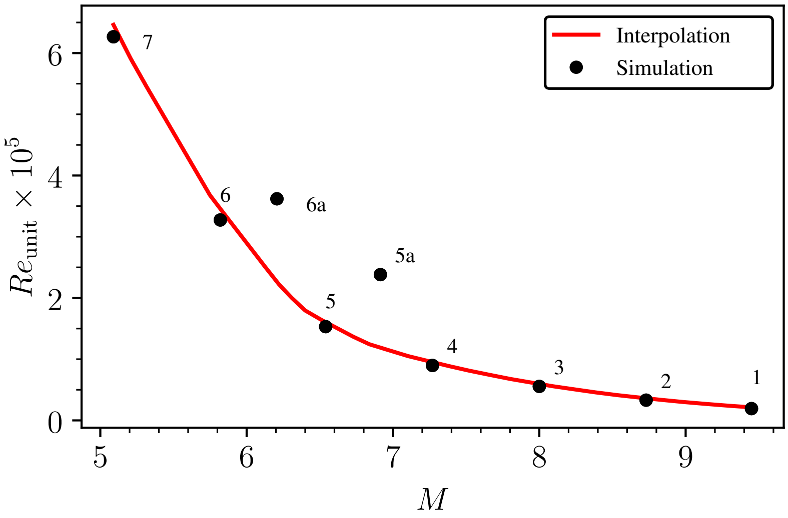

Figure 6.1. Supersonic retro-propulsion trajectory in M-Re_{unit} space with support points.

Since this aerothermal analysis is part of a preliminary design process, Ecker et al. [12] generated the database in the Mach and Reynolds number space. Using this approach, the trajectory could easily be adapted if demanded from the system engineering side. The current trajectory is in the Mach number range from 9.5 to 5.1 and in the unit Reynolds number range from 20,000 to 600,000. Re_{unit} was chosen to be independent of changes in the first stage's dimensions. Additionally, to the seven points on the trajectory, two extra points were added outside the trajectory to support the linear interpolation in non-linear areas of the trajectory and to make trajectory adaption easier [9].

At each point two simulations were carried out with uniform wall temperatures of 300 K and 400 K. This temperature range was found by Ecker et al. [12], when conducting investigations of the thermal loads during supersonic retro-propulsion of a SpaceX Falcon-9-like configuration. They observed a surface heating from 300 K to 400 K over the maneuver. Their finding is supported by a NASA publication of infrared imaging of the Falcon 9 during re-entry [13].

From the two simulations at each trajectory point we obtain two sets of wall heat fluxes to the first stage. This temperature interval from 300 K to 400 K is divided into sub-ranges with temperature steps of 10 K, i.e. 300, 310, 320, ..., 400 K. The distance between the simulation points in the M-Re_{unit} space was similarly divided into linear sub-intervals, indicated as a red line in figure 6.1. The support points outside the trajectory helped to maintain linearity in the curved part of the SRP trajectory between 6 and 4. The wall heat flux from the distinct simulations points is interpolated linearly along the red line for the temperature steps between 300 K and 400 K. As the result the heat flux database is obtained that provides the wall heat flux for the temperature interval at each point along the red line in M-Re_{unit} space. Thus, the wall heat flux evolution is determined by assuming a linear dependence of M, Re and T_{w}.

6.1.2 Structural Heat Transfer Model

Dumont et al. [9] estimate the evolution of the sidewall heat flux (as a function of the sidewall temperature) and the sidewall temperature for configuration A along the retro-propulsion trajectory. Therefore, they applied a simple structural heat transfer model: They considered the sidewall material to be aluminum and divided the surface into evenly spaced elements, to which the lumped mass model is applicable. In each surface element, they calculated the surface temperature via a simple energy balance equation, which is coupled with the heat flux database (figure 6.2). Neither heat conduction between elements or into the adjacent structure nor radiation were taken into account.

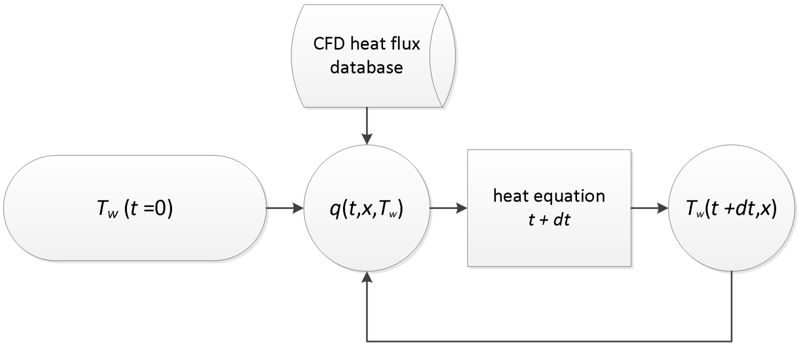

Figure 6.2. Coupling of the aerothermal database and the energy balance equation after [9].

This thesis extends the sidewall heat load estimation to configuration B and creates a new database for the baseplate. Finding a viable surface element distribution for the baseplate is also part of this thesis. For the simulations the baseplate surface is discretized with a unstructured triangular grid. Due to the fine triangulation of the surface, the simulation grid elements are chosen for the lumped mass model. Since the heat flux to the sidewall and to the baseplate are considered in this thesis, two databases are generated to be able to asses the heat loads to the sidewall and baseplate separately.

Lumped Mass Model

The lumped mass model assumes that there exist no temperature gradients inside a body, i.e. heat applied at the body's surface instantly distributes homogeneously inside the body. Thus, the body is heated to a uniform temperature. This assumption is valid for materials that conduct heat very good. An indicator whether a body conducts the heat sufficiently well is the Biot number, Bi. For $Bi < 0.1$ the body is able to distribute the heat fast enough in such a way that the homogeneous temperature assumption is valid [74]. A sample calculation in appendix B showed $Bi = 4.4 \cdot 10^{-4}$ meeting the requirements of $Bi < 0.1$.

Structural Heat Transfer

The database contains the CFD simulation outputs of the convective wall heat fluxes $\dot{q}_{\mathrm{w}}$ as a function of the wall temperature at each surface element grid node. Since the lumped mass model is assumed, each grid node represents a surface element, in which the applied heat flux is distributed instantly and homogeneously. The resulting temperature rise is calculated from the following energy balance equation [9]:

$$T_{\mathrm{w}}(t+dt,\, \vec{x}) = \frac{\rho\, b\, c_p\, T_{\mathrm{w}}(t,\, \vec{x}) + \dot{q}_{\mathrm{w}}(t,\, \vec{x},\, T_{\mathrm{w}}(t,\, \vec{x}))\, dt}{\rho\, b\, c_p} \tag{6.1}$$

The wall element at position $\vec{x}$ and temperature $T_w(t,\, \vec{x})$ is exposed to the wall heat flux $\dot{q}_{\mathrm{w}}(t,\, \vec{x}, T_{\mathrm{w}}(t,\, \vec{x}))$ over the time dt and heats up to the temperature $T_w(t+dt,\, \vec{x})$. ρ, b and c_p stand for the density, thickness, and specific heat capacity at constant pressure of the wall material aluminum (cf. table 6.1 and figure 6.4a for the thickness distribution of the sidewall).

Property	
c_p [J/kg K]	864
ρ [kg/m^3]	2840
b [mm]	1.8 - 3.4

Table 6.1. Aluminum properties for baseplate and sidewall material [9].

The wall heat flux and temperature evolution along the trajectory is estimated as follows: Starting at the first trajectory point, assuming $T_w(t=0,\, \vec{x}) = 300$ K, the wall heat flux is looked up in the database corresponding to this temperature. Then the resulting wall temperature of the wall element is calculated from equation (6.1) assuming that the heat flux was applied for $dt = 1$ s. Having the new wall temperature $T_{\mathrm{w}}(t+dt,\, \vec{x})$, the heat flux corresponding to the new wall temperature $\dot{q}_{\mathrm{w}}(t+dt,\, \vec{x}, T_{\mathrm{w}}(t+dt,\, \vec{x}))$ is looked up in the database and the resulting wall temperature is determined. This loop continues till the end of the retro-propulsion trajectory is reached. These steps are visually summarized in figure 6.2.

6.2 Heat Loads during Supersonic Retro-propulsion

This section analyzes the sidewall and baseplate heat flux and temperature evolution along the retro-propulsion trajectory from the structural heat transfer analysis. Additionally, the effects of engine configurations A and B on the wall temperature are compared. The heat flow rate at every trajectory point and the integral heating over the retro-propulsion maneuver are presented as well.

6.2.1 Sidewall

The evolution of the sidewall heat flux over the seven trajectory points is illustrated in figure 6.3. The effects of the plume surface interaction (cf. section 5.3.2) have a noticable influence on the wall heat flux and temperature evolution during the SRP maneuver. The heat flux to the sidewall is continuously increasing with decreasing altitude, ranging from around 5 kW/m^2 at the beginning to up to 20 kW/m^2 at the end. The maximum heat flux of every trajectory point occurs at the area on which the plume is impinging. This impinging

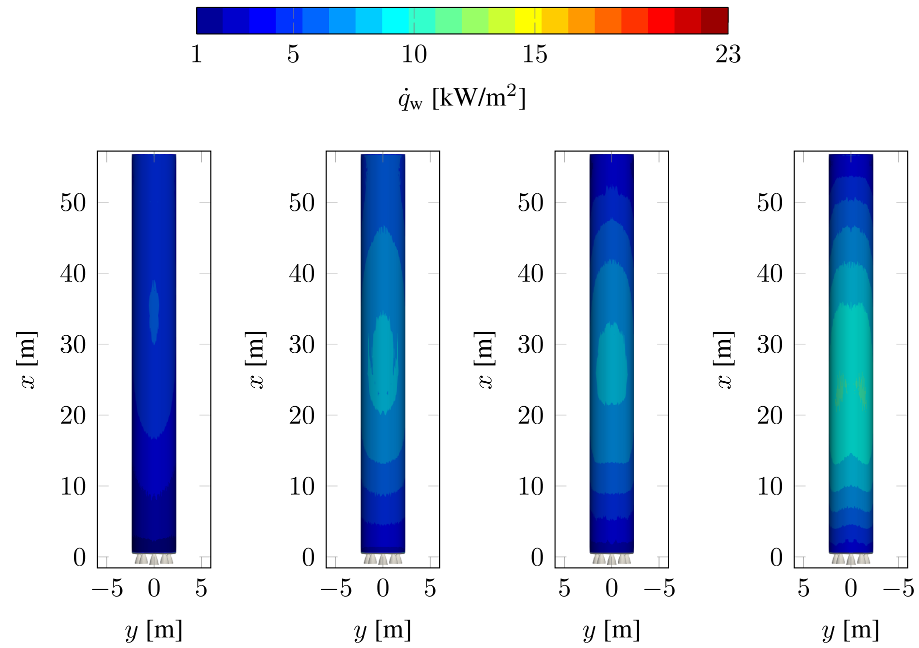

(a) Trajectory point 1.

(b) Trajectory point 2.

(c) Trajectory point 3.

(d) Trajectory point 4.

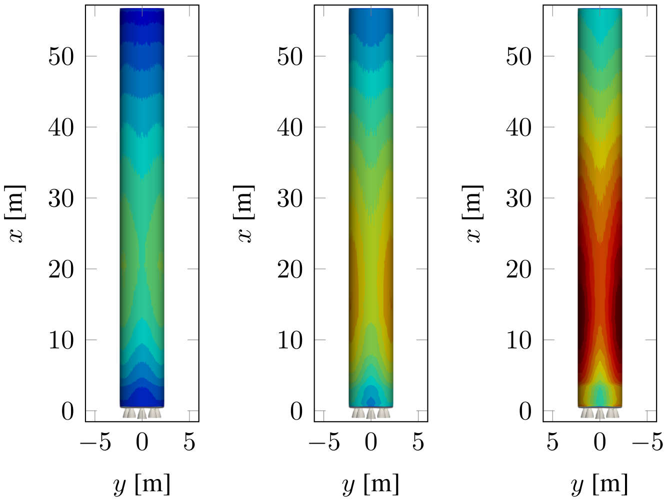

(a) Trajectory point 5.

(b) Trajectory point 6.

(c) Trajectory point 7.

Figure 6.3. Sidewall heat flux evolution along SRP trajectory, active engines along z (normal to viewing plane).

area moves towards the aft of the first stage as the plume contracts with decreasing altitude (see also figures 5.11 to 5.14). At trajectory point 4 the impinging area starts to shift from parallel to the active engine axis (z) to a plane normal to the active engines axis (y). Probably a result of the weaker plume-plume interaction, that also affects the baseplate.

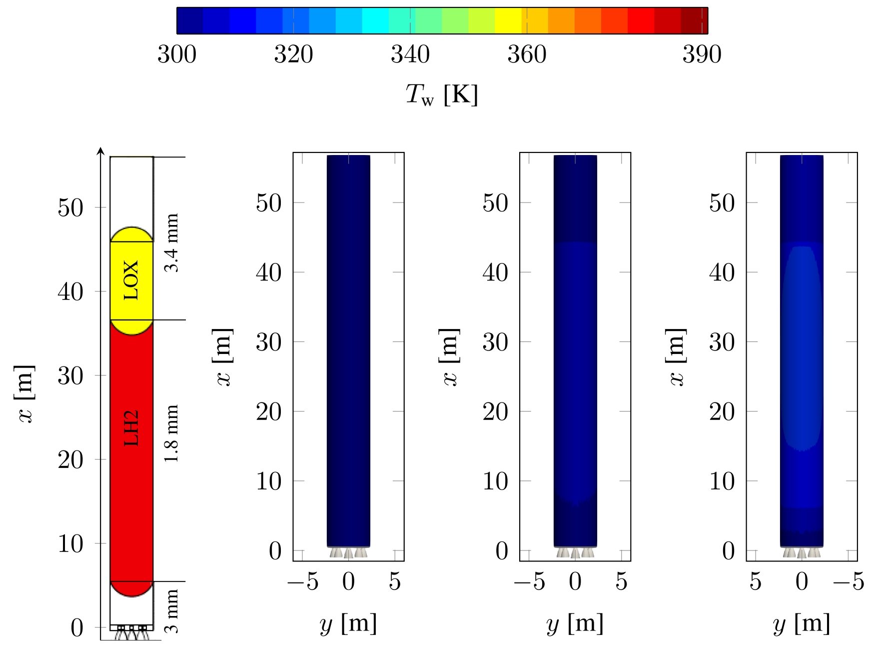

(a) Thickness distribution.

(b) Trajectory point 1.

(c) Trajectory point 2.

(d) Trajectory point 3.

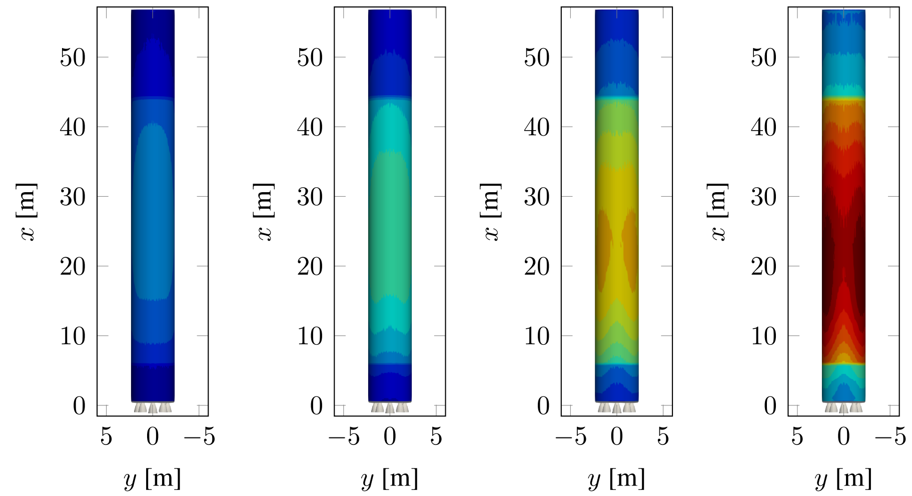

(a) Trajectory point 4.

(b) Trajectory point 5.

(c) Trajectory point 6.

(d) Trajectory point 7.

Figure 6.4. Sidewall temperature evolution along SRP trajectory, active engines along z (normal to viewing plane).

The sidewall temperatures for the the same trajectory points are illustrated in figure 6.4. At the beginning of the re-entry burn, the first stage's walls are assumed to be at uniformly 300 K. The wall thickness distribution, indicated in figure 6.4a, leads to higher temperatures at the LH2 tank, which has the thinnest wall thickness. With the impinging hot plume the sidewall heats up to almost 400 K at the thin LH2 tank. Note that the maximum temperature follows the plume impinging area. Infrared measurements conducted by NASA of the sidewall temperature of SpaceX Falcon 9's first stage before and after the re-entry burn [13] revealed a maximum wall temperature of 450 K after the re-entry burn. Given the differences between the DLR configuration and Falcon 9 (cf. table 1.1) and the errors NASA estimated on their temperature measurements, the prediction of the maximum temperature from the simulation seems reasonable.

6.2.2 Baseplate

The heat flux to the baseplate along the retro-propulsion trajectory is presented in figure 6.5. At the beginning of the maneuver the heat flux to the baseplate reaches its maximum of 70 kW/m^2 and decreases with decreasing altitude. Over the first three

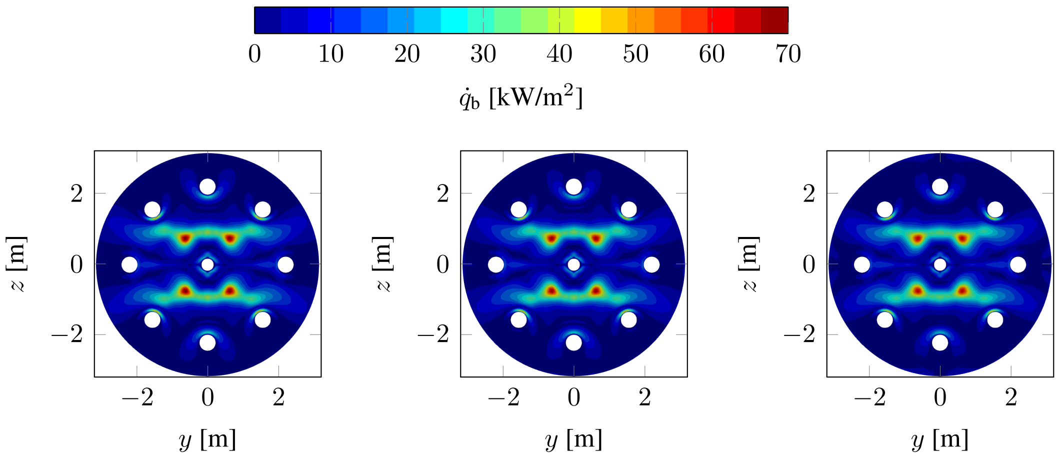

(a) Trajectory point 1 **(b)** Trajectory point 2. **(c)** Trajectory point 3

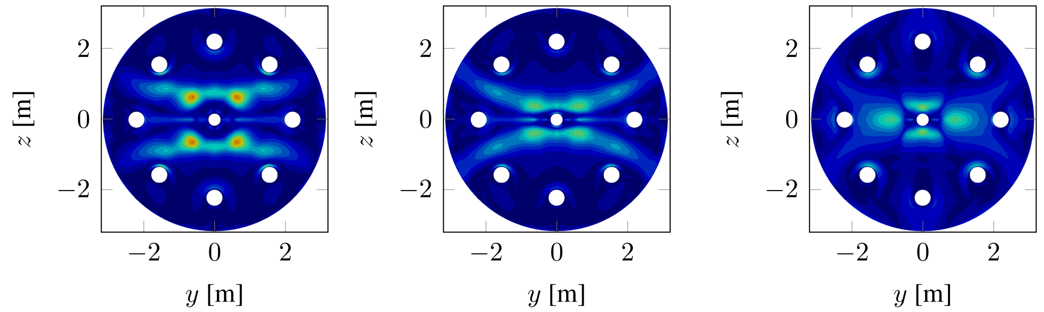

(a) Trajectory point 4. **(b)** Trajectory point 5 **(c)** Trajectory point 6.

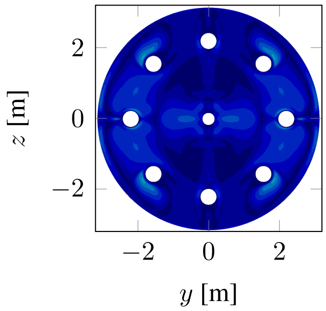

(a) Trajectory point 7

Figure 6.5. Baseplate heat flux evolution along SRP trajectory, active engines along z centerline.

points the heat flux distribution does not change at all, which is believed to stem from the choked flow conditions at the base due to the plume-plume interaction at the nozzle exits (cf. sections 2.2.1, 2.2.4 and figures 5.9b, 5.15a). The location of the maximum heat flux left and right of the centerline could come from the sideways extending center-nozzle plume (figure 5.9b) entraining most of the plume to the sides. With decreasing altitude the level of jet under-expansion reduces and therefore the impinging plume jet become weaker, resulting in lower baseplate heat fluxes. The distribution changes its pattern from the maximum at the center nozzle to a more evenly distributed heat flux at the end of the trajectory.

For comparison, the DLR winged first stage reaches peak heat fluxes of 3 MW/m^2 during its passive re-entry (h = 30 km M = 8.8) [75]. Thus, the peak heat fluxes of the sidewall 20 kW/m^2 and baseplate 70 kW/m^2 occurring during the SRP maneuver are significantly (two orders of magnitude) reduced compared to the winged stage and pose marginal heat loads to the wall materials.

The baseplate temperature evolution along the trajectory for a uniform baseplate thickness of 3 mm is depicted in figure 6.4. The wall material is assumed to be aluminum,

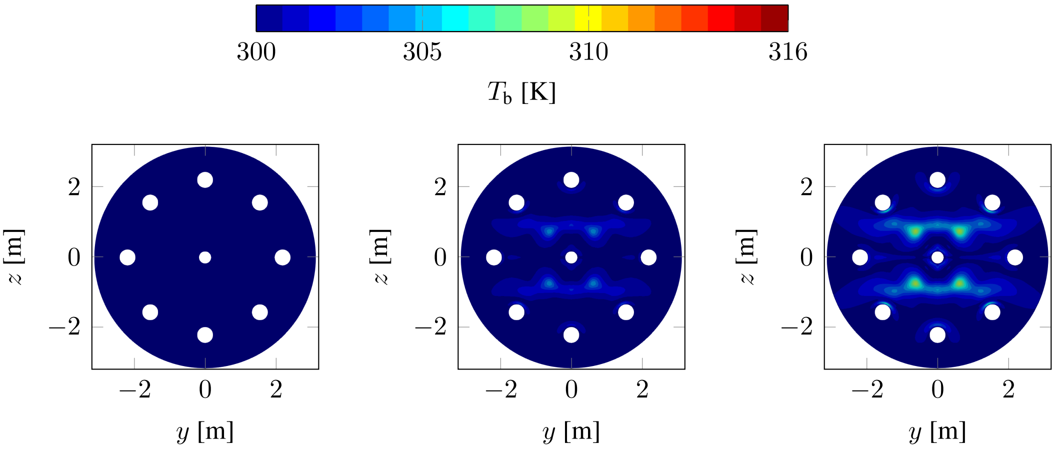

(a) Trajectory point 1 **(b)** Trajectory point 2. **(c)** Trajectory point 3

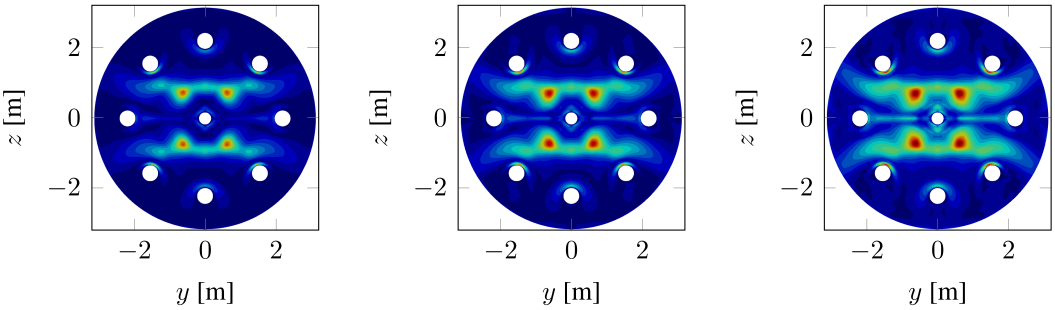

(d) Trajectory point 4. **(e)** Trajectory point 5 **(f)** Trajectory point 6.

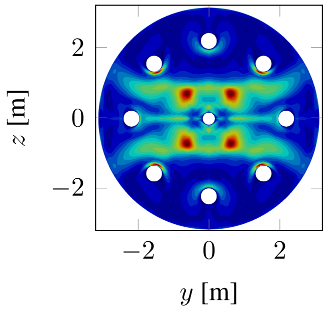

(g) Trajectory point 7

Figure 6.4. Baseplate temperature evolution along SRP trajectory for baseplate thickness of 3 mm along retro-propulsion trajectory, active engines along z centerline.

similar to the sidewall. At the beginning of the trajectory the baseplate temperature is also assumed to be at 300 K rising up to 316 K at the end. The highest temperatures are reached in the regions of the impinging plume jets around the center nozzle and the path the plume jet takes when radially flowing out between the nozzles.

Further, baseplate thicknesses from 1.8 to 5 mm were investigated. They all reveal the same temperature distribution pattern which mainly varies in magnitude and temporal development. The maximum temperature of the different thicknesses is indicated in table 6.2, for the actual distributions see appendix C.1.

b [mm]	$T_{\mathrm{b,max}}$ [K]
1.8	326
3	316
5	309

Table 6.2. Maximum baseplate temperatures $T_{\mathrm{b,max}}$ for different baseplate thicknesses b.

Overall, the temperature rise at the baseplate by around 20 K for $b = 3$ mm is negligible compared to the temperature rise of the sidewall.

6.2.3 Influence of Combustion Chamber Parameters

As found in section 5.3.4, the combustion chamber temperature influences the plume temperature and thus the wall heat flux. The present section examines the impacts on the wall temperatures of sidewall and baseplate. A comparison of the sidewall temperatures for the two configurations A and B is given in figure 6.5. There the maximum, mean and minimum sidewall temperature evolution along the trajectory is displayed. Configuration B leads to an overall lower wall temperature. The maximum temperature at the end is slightly under 400 K (392 K) thus by about 3 % lower than configuration A (402 K) with a 5 % difference in chamber temperatures (see table 5.2). Given that the combustion chamber conditions were only slightly modified, the reduction in temperature would become more considerable, when the combustion parameters change significantly i.e. when the engines are throttled to reduce the thrust level. This figure reveals further, that the mean temperature rise of around 70 K is in manageable orders for the sidewall material. Thus, a further thermal protection for the sidewall will likely not be necessary.

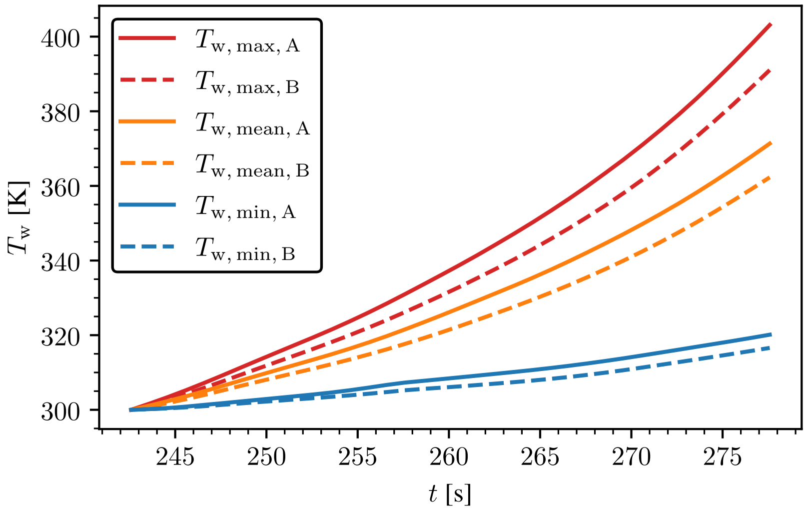

Figure 6.5. Influence of combustion chamber temperature on sidewall temperature evolution.

The evolution of the baseplate temperatures is shown in figure 6.6 for a baseplate thickness of 3 mm (further thicknesses in appendix C.2). The same influence of the combustion chamber temperature is visible here as well. However, as already stated in section 6.2.2 the temperature increase along the re-entry burn is negligible. At $t \approx 257$ s the slope of the maximum temperature reduces indicating lower heating from thereon. This time corresponds to trajectory point 4, where the decrease in heat flux was observed due to leaving the choked baseflow condition.

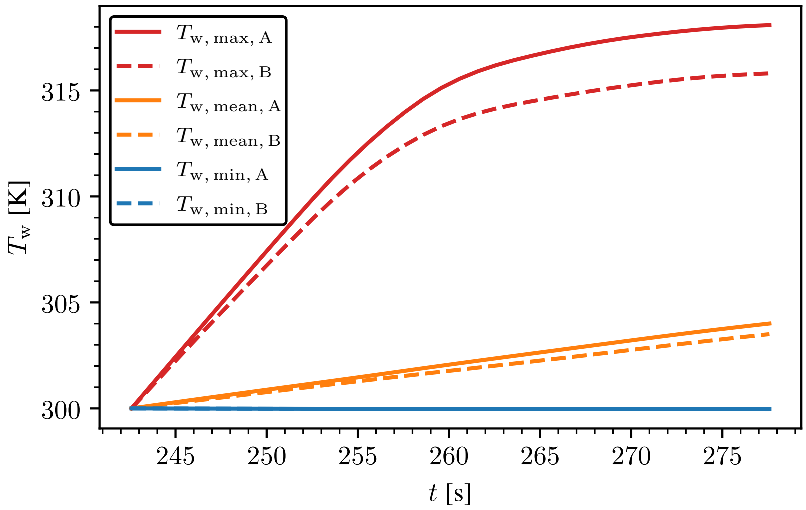

Figure 6.6. Influence of combustion chamber temperature on baseplate temperature evolution for $b = 3$ mm.

6.2.4 Integral Heating

This section shows the overall rate of heat flow to the baseplate, as well as to the baseplate and sidewall together with the rate of heat flow before and after the SRP maneuver when engines are deactivated.

The overall rate of heat flow to the baseplate is shown in figure 6.7a. The maximum rate of heat flow of around 210 kW is reached at the beginning of the trajectory due to the choked base flow conditions. The oscillating behavior is explained with the unsteady flow behavior at the base. The heat flow rate should be constant until the base leaves the choked flow conditions between trajectory points 3 and 4 (between 253 and 257 s) and should decrease afterwards due to the reduction in plume interaction. The heat flow rate

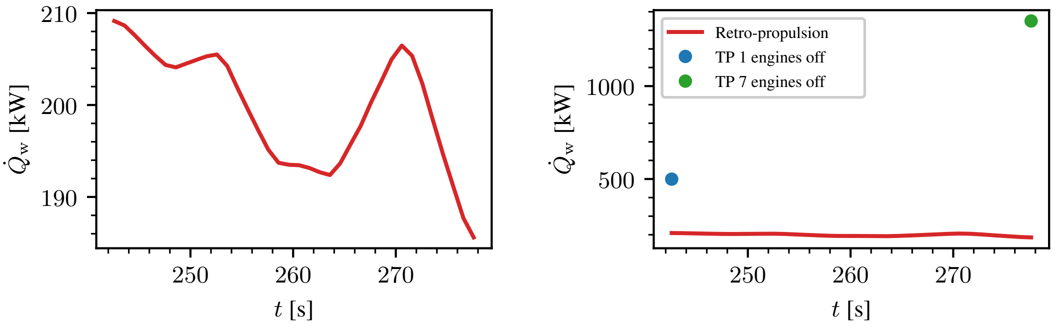

(a) Baseplate rate of heat flow along SRP trajectory.

(b) Baseplate rate of heat flow along SRP trajectory compared to deactivated engines.

Figure 6.7. Rate of heat flow to baseplate along SRP trajectory compared to deactivated engines.

of configuration A follows this trend more closely (cf. appendix D). Comparing the heat flow rate of the ignited engines to the deactivated engines in figure 6.7b shows that the heat flow rate to the baseplate at deactivated engines is two times higher in the beginning and seven times higher at the end compared to the ignited engines. Consequently, the baseplate is protected by the hot plume during the retro-propulsion maneuver from the enormous heat loads occurring over the bow shock.

The overall heat flow rate to the sidewall and baseplate, together with the heat flow rate of the deactivated engines, is illustrated in figure 6.8. The maximum rate of heat flow reaches 18.5 MW, suggesting that the sidewall heat flow is predominant compared to the baseplate ($\dot{Q}_{\mathrm{max,b}} = 210\,\mathrm{kW}$). The overall heat flow rate to the first stage with deactivated engines is considerably smaller, not even half the of heat flow rate with active engines (2.3 MW in the beginning and 7.5 MW at the end). But as already stated in section 5.3.5 the heating at deactivated engines is concentrated around the aft of the first stage, whereas the heat flow rate is distributed over the entire stage when engines are ignited.

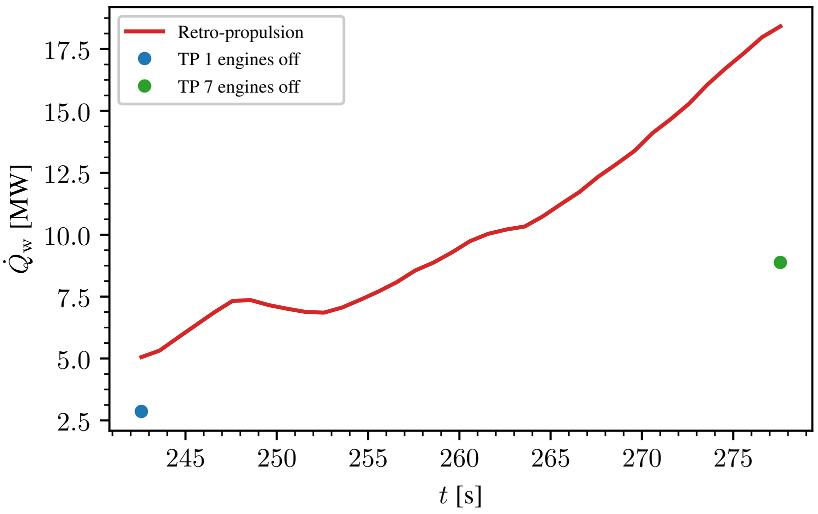

Figure 6.8. Rate of heat flow to sidwall and baseplate along trajectory compared deactivated engines.

The integral heating of the wall Q_{w} over the retro-propulsion trajectory is given in table 6.3, reaching 372.2 MJ for baseplate and sidewall together.

	Q_{w} [MJ]
Sidewall	365.0
Baseplate	7.2
Total	372.2

Table 6.3. Integral heating Q_{w} over the SRP trajectory.

6.3 Database Validation and Modeling Issues

6.3.1 Database Validation (2dbv, 4dbv, 7dbv)

The simple modeling approach with the database and the energy balance equation does take neither flow history effects nor history effects of the wall temperature evolution during the simulations into account. Forcing the wall temperatures to uniform levels during the simulation excludes any influences of the heating surfaces to the wall heat flux, since the wall heat flux is a function of the temperature difference between wall and fluid.

In order to estimate the error that is made by this modeling approach, trajectory points 2, 4 and 7 were chosen for the database validation. The sidewall temperature profiles obtained from the database at these points, were taken and applied as isothermal wall temperature boundary conditions in the simulations. The temperature profiles are displayed in figures 6.4c, 6.4a and 6.4d. These simulations provide the wall heat flux $\dot{q}_{\mathrm{w,sim}}$ resulting from the inhomogeneous temperature distribution. The obtained wall heat fluxes are compared to the heat fluxes from the database at the corresponding trajectory point.

The ratio of database to simulation heat flux for all cases are presented in figure 6.9. The sidewall of the quarter segment is visualized as a plane, in which the edge $\zeta = 90°$ is parallel to the active engine axis and $\zeta = 0°$ corresponds to the edge perpendicular to the active engines. At the beginning of the retro-propulsion maneuver (trajectory point 2) the database over-predicts the heat flux to the side wall by up to 35 % as indicated in figure 6.9a. Especially, the heat flux to the upper part on the active engine side, where the plume is impinging is elevated. It was expected, that the difference between simulation and database would be rather small, since it is not so far away from the initial temperature distribution. The deviation is therefore assumed to stem from a not fully converged solution used for the database. At trajectory point 4 in figure 6.9b the database under-predicts the heat flux by up to 20 %. A deviation of simulation and database was expected since point 4 is furthest away from the two set temperature boundary conditions. Trajectory point 7 shows little deviation between (2 to 5 %) the simulation and the database. This was also expected, since the surface temperature has reached up to 400 K in the simulation and the database. The influence of the sidewall thickness is visible where the straight lines of darker blue appear.

In table 6.4 the relative root mean square error between simulation and database $(\dot{q}_{\mathrm{w,sim}} - \dot{q}_{\mathrm{w,db}})/\dot{q}_{\mathrm{w,sim}}$ is presented. It supports the differences pointed out in figure 6.9. The largest error appears at trajectory point 2 due to the over-prediction and the lowest at point 7 where the simulation and database coincide.

	RMS [%]
Trajectory point 2	17
Trajectory point 4	8
Trajectory point 7	3

Table 6.4. Relative root mean square error of $(\dot{q}_{\mathrm{w,sim}} - \dot{q}_{\mathrm{w,db}})/\dot{q}_{\mathrm{w,sim}}$ in [%].

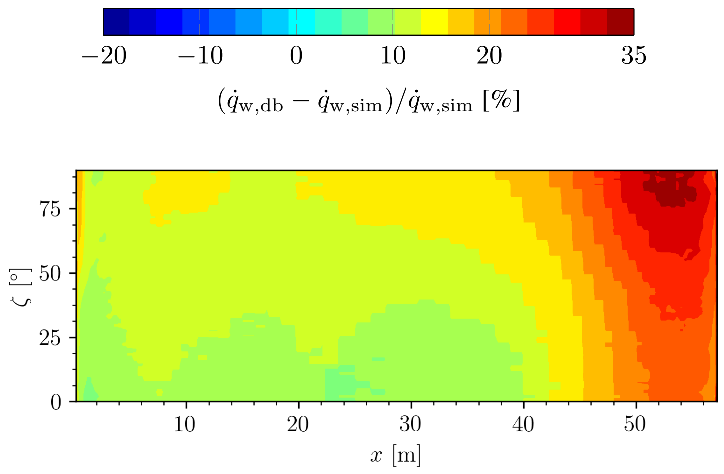

(a) Trajectory Point 2.

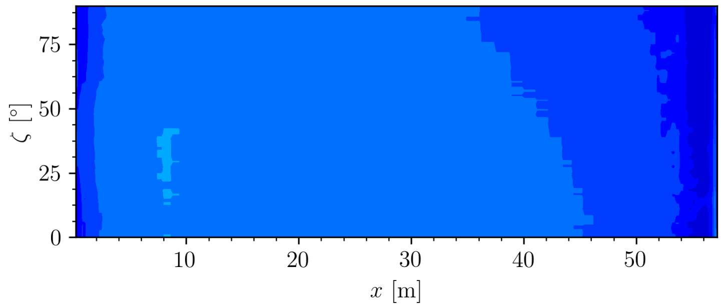

(b) Trajectory Point 4.

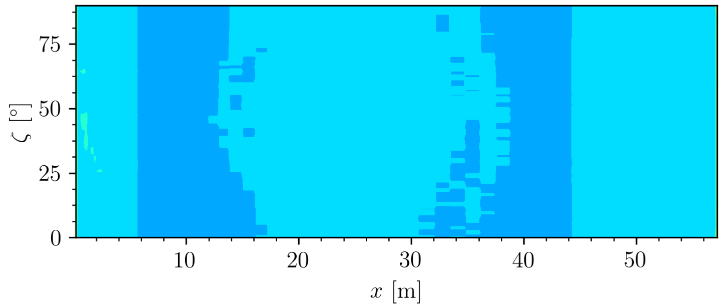

(c) Trajectory Point 7.

Figure 6.9. Comparison of heat flux from database with heat flux from simulation, when applying database wall temperature profile at corresponding trajectory point; $\zeta = 0°$: inactive engines axis; $\zeta = 90°$: active engines axis.

6.3.2 Database Modeling Issues

The database is constructed by linearly interpolating the heat flux between the trajectory points in the M-Re_{unit} space. However, as described in section 6.1.1 support points were needed to maintain the linear interpolation procedure in the non-linear parts of the trajectory. Ecker et al. [12] estimated the error of the linear reconstruction by the support points to around 10 % for the database.

Furthermore, the linear dependence of the wall heat flux from M, Re and T_{w} is an additional simplification necessary in the preliminary design process. The evolution of the sidewall heat flux follows a linear trend (cf. slopes in figure 6.5). However, the baseplate heat flux spreads more around the linear trend. This is due to the higher instabilities of the flowfield in this area. A further time-dependent investigation of the baseplate flowfield is therefore necessary. Furthermore, the baseplate heat flux is at choked conditions (i.e. constant) over the first three trajectory points (see figures 6.3a to 6.3c) and then reduces with decreasing altitude (see also slope of maximum temperature in figure 6.6 or heat flow rate in figure 6.7a). Thus, the linearity of the baseplate heat flux is not inherently given for the baseplate flowfield. A different interpolation approach could therefore be considered in the future.

6.4 Summary of Observations

In this chapter the thermal loads on the sidewall and baseplate of the first stage along the re-entry burn trajectory were investigated. Therefore, a heat flux database was constructed and coupled with a simple structural model to estimate the heat flux evolution and wall temperature increase. The modeling approach simplifies the time-dependent estimation of the heat flux evolution and wall temperature estimation, thus introducing errors up to 20 %. These errors are acceptable in the course of a preliminary design study as other uncertainties will likely be of similar magnitude.

The sidewall heat flux constantly increases along the trajectory ($\dot{q}_{\mathrm{w,max}} = 20$ kW/m^2), following the described flow patterns in section 5.3.2. The overall heating and temperature increases by around 100 K to an absolute temperature of 400 K. This increase is in a temperature range that that should be manageable by the wall material aluminum without an additional TPS.

The baseplate heat flux shows the opposite development. Starting at choked base flow conditions, which continue until the first third of the trajectory, the heat flux remains constant ($\dot{q}_{\mathrm{b,max}} = 70$ kW/m^2). It then decreases with decreasing altitude. The lower under-expansion of the nozzle and thus weaker plume interaction is responsible for this development. The overall heating and temperature increase, however are far from being a threat to the baseplate material. Therefore, the retro-propulsion maneuver does not demand any further protection. This finding is reinforced by the peak heat flux of the winged gliding stage, which reaches 3 MW/m^2 during its passive re-entry.

The influence of the combustion chamber configuration on the wall temperature was evaluated, showing a direct link between the combustion temperature and the wall temperature: A 5% lower combustion temperature results in a maximum 3 % lower wall temperatures at the sidewall. The influence on the baseplate was again negligible.

The rate of heat flow to the sidewall and baseplate over the retro-propulsion trajectory revealed an integral heating of 372 MJ over the 35 s.

Chapter 7

Conclusions and Outlook

Re-usable launch vehicles have a potential to significantly change the launch service market once low refurbishment costs and high reliability are guaranteed. Therefore, DLR conducted a system analysis testing a re-usable launch system capable of bringing 7 t to GTO. One concept is a retro-propulsion decelerated vertical landing vehicle. The idea is to decelerate the returning first stage by providing thrust in the opposite direction of motion. The retro-propulsion maneuver is carried out between 70 and 36 km and covers a Mach number range from 9.5 to 5.1. The thrust is provided by re-igniting three of the nine main engines that run on a propellant combination of LH2 and LOx.

The objective of this thesis is to investigate the thermal loads of a re-usable first stage during the retro-propulsion maneuver and the final landing approach using RANS simulations. The focus is on the impact of the flowfield phenomena on the thermal loads of the first stage's sidewall and baseplate.

Steady RANS simulations are conducted at specific points along the retro-propulsion trajectory. The influence of different flow and vehicle conditions (flow angles, combustion chamber configurations, deactivated engines, thermal nozzle radiation) is investigated. The evolution of the thermal loads over the retro-propulsion maneuver is determined by creating a heat flux database from the trajectory point simulations. The database is coupled with a simple structural model to estimate the wall temperature and the integral heating. The database is validated at selected points and showed an uncertainty of approximately 20 % for the heat flux estimation.

7.1 Conclusions

The thermal loads on the first stage's wall strongly depend on the supersonic retro-propulsion flowfield. The flowfield is characterized by a highly under-expanded plume flow exhausting into an opposing supersonic freestream. The sidewall loads are mainly affected by the interaction of the hot exhaust plumes with the oncoming freestream. The opposing freestream forces the plume flow to turn, immersing the whole first stage in its own hot exhaust gas. Parts of the plume impinge on the sidewall. At these impingement areas the thermal loads are highest. With decreasing altitude the maximum thermal loads increase up to 20 $\mathrm{kW/m^2}$ and move to the aft of the first stage, as the plume contracts due to the denser atmosphere. The maximum heat loads increase locally up to 20 % on the sidewall, when the first stage is flying under an angle of 5° towards the freestream. The thermal loads can be reduced by 3 % when decreasing the combustion temperature by 5 %. Over the retro-propulsion maneuver the sidewall temperature rises by about 100 K to a maximum temperature of 400 K depending on the sidewall thickness distribution. This temperature increase is also supported by NASA infrared images of SpaceX Falcon 9 that show a maximum sidewall temperature of 450 K after the retro-propulsion maneuver.

The baseplate heat loads are highly influenced by the level of under-expansion of the exhaust plumes. The plumes impinge on each other, forming oblique shocks that drive parts of the plume towards the baseplate. This phenomenon causes the formation of an "impinging plume jet". The maximum heat load (70 kW/m^2) occurs where the plume jet impinges on the base. The maximum heat load remains constant, as long as the level of plume under-expansion causes choked conditions at the base. The maximum therefore decreases with decreasing altitude, i.e. lower plume under-expansion levels. The flight angle (200 % higher heat flux) and combustion temperature have the same effect on the maximum loads on the baseplate. The contribution of thermal radiation of the nozzle walls to the baseplate heat flux is negligible. The temperature evolution on the baseplate along the SRP trajectory revealed only a minor increase by about 20 K depending on the baseplate thickness.

The landing boost shows insignificant heat loads to the sidewall but heat fluxes up to 200 kW/m^2 at the baseplate. The plume extends circular around the first stage reaching 60 m in diameter. The plume is still at temperatures of approximately 700 K, which should be considered for the safety and operation conditions at the landing site.

The results show that during the supersonic retro-propulsion maneuver the heat loads are redistributed compared to the non-propulsive phase before and after. With deactivated engines the heat loads are concentrated around the aft of the first stage and are increase by up to eight times. During the retro-propulsion maneuver the baseplate and aft are protected by the plume, which in turn causes 80 % higher thermal loads on the upper part. The integral heating of the first stage sidewall and baseplate over the retro-propulsion maneuver is 370 MJ, showing only a small contribution of the baseplate. Comparing the peak heat fluxes of the retro-propulsion configuration to the winged gliding stage (3 MW/m^2), shows that the retro-propulsion configuration experiences heat fluxes that are reduced by two orders of magnitude. Overall, the retro-propulsion maneuver does not demand any further thermal protection system, neither for the sidewall nor the baseplate and is not of significance for the design critical heat loads.

7.2 Outlook

Future studies should incorporate landing legs and grid fins in the CFD simulations. Furthermore, an approximation of the wall temperature at the beginning of the retro-propulsion maneuver would help to improve the heat load modeling from the database. Using a detailed chemical reaction mechanism for the nozzle and plume flow could reveal the impacts of chemical processes on the heating, like post-combustion in the plume.

Additionally, the baseplate flowfield requires further studies in order to better understand the unsteadiness of the flowfield in this region.

Bibliography

[1] L. David. Mars via Musk - Building Blocks. `http://www.leonarddavid.com/wp-content/uploads/2016/05/25787998624_e1cb7b812f_b.jpg`, 2016. Accessed on 25-September-2017.

[2] K. Dismukes . Deorbit. `https://spaceflight.nasa.gov/shuttle/reference/shutref/events/deorbit/`, 2002. Accessed on 21-November-2017.

[3] A. Korzun. *Aerodynamic and Performance Characterization of Supersonic Retropropulsion for Application to Planetary Entry and Descent*. PhD thesis, Georgia Institute of Technology, School of Aerospace Engineering, 2012.

[4] Jet Propulsion Laboratory. Mars Science Laboratory - Entry, Descent and Landing. `https://mars.jpl.nasa.gov/msl/mission/spacecraft/edlconfig/`, 2017. Accessed on 20-November-2017.

[5] NASA. Soyuz Landing. `https://www.nasa.gov/mission_pages/station/structure/elements/soyuz/landing.html`, 2017. Accessed on 20-November-2017.

[6] `https://forum.kerbalspaceprogram.com/index.php?/topic/129790-image-spacex-falcon-9-launch-profile/`. Accessed on 04-October-2017.

[7] M. Ragab, F. Cheatwood, S. Hughes and A. Lowry. Launch Vehicle Recovery and Reuse. *American Institute of Aeronautics and Astronautics (AIAA)*, 2015.

[8] M. Sippel, S. Stappert, L. Bussler and E. Dumont. Systematic Assessment of Reusable First-Stage Return Options. In *68*$^{\text{th}}$ *International Astronautical Congress (IAC)*, 2017.

[9] E. Dumont, S. Stappert, T. Ecker , J. Wilken, S. Karl, S. Krummen and M. Sippel. Evaluation of Future Ariane Reusable VTOL Booster Stages. 68th *International Austronautical Congress (IAC)*, 2017.

[10] Leonid Bussler. Status Vorauslegung RLV. DLR Institut für Raumfahrtsysteme, Systemanalyse Raumtransport (SART), Bremen.

[11] M. Sippel, C. Manfletti and H. Burkhardt. Long-Term/Strategic Scenario for Reusable Booster Stages. In *12th International Space Planes and Hypersonic Systems and Technologies Conference*, 2003.

[12] T. Ecker, S. Karl, E. Dumont, S. Stappert and D. Krause. A Numerical Study on the Thermal Loads During a Supersonic Rocket Retro-Propulsion Maneuver. In *53rd AIAA/SAE/ASEE Joint Propulsion Conference*, 2017.

[13] T. Horvath, V. Aubuchon, S. Rufer, C. Champbell, R. Schwartz, C. Mercer, S. Tack, T. Spisz, J. Taylor, D.Gibson, K. Osei-Wusu, S. Kennerly, G. Scriven, T. Pottebaum and M. Ross. Advancing Supersonic Retro-Propulsion Technology Readiness: Infrared Observations of the SpaceX Falcon 9 First Stage. *AIAA*, 2017.

[14] R. Launius and D. Jenkins . *Coming home : Reentry and Recovery from Space*. NASA, 2011.

[15] Insitute for Space Systems, University of Stuttgart. Atmospheric Entry Technology. Lecture Notes to "Atmospheric Entry Technology", Master of Science Aerospace Engineering at the University of Stuttgart, 2016.

[16] E. Hirschel. *Bascis of Aerothermodynamics*. Springer, 2005.

[17] P. Gnoffo. Planetar-entry Gas Dynamics. *Annual Review of Fluid Mechanics*, 31(1): 459–494, 1999.

[18] NASA Content Administrator. Expedition 23 Returns to Earth. `https://www.nasa.gov/multimedia/imagegallery/image_feature_1681.html`, 2010. Accessed on 19-September-2017.

[19] E. Darso, V. Pritchett , T. Wang, D. Ota, I. Blankson and A. Auslender. The Dynamics of Shock Dispersion and Interactions in Supersonic Freestreams with Counterflowing Jets. In *45th AIAA Aerospace Sciences Meeting and Exhibit*, 2007.

[20] Space Exploration Technologies Corp. Advancing The Future. `http://www.spacex.com/about`, 2017. Accessed on 26-September-2017.

[21] E. Love. The Effects of a Small Jet of Air Exhausting from the Nose of a Body of Revolution in Supersonic Flow. Technical report, NACA, 1952.

[22] B. Venkatachari, M. Mullane, G. Cheng and C. Chang. Numerical Study of Counterflowing Jet Effects on Supersonic Slender-Body Configurations. In *33rd AIAA Applied Aerodynamics Conference*, 2015.

[23] J. D. Anderson. *Fundamentals of Aerosdynamics*. McGraw-Hill, 2nd edition, 1991.

[24] E. Krämer. Strömungslehre 2. Lecture Notes to "Strömungslehre 2", Bachelor of Science Aerospace Engineering at the University of Stuttgart, 2012.

[25] G. Sutton and O. Biblarz. *Rocket Propulsion Elements*. Springer, 2015.

[26] C. Baille and G. Comte-Bellot. *Turbulence*. John Wiley & Sons, 7 edition, 2001.

[27] J. Seiner, M. Ponton, B. Jansen and N. Lagen. The Effects of Temperature on Supersonic Jet Noise Emission. In *DGLR/AIAA 14th Aeroacoustic Conference*, May 1992.

[28] M. Abbett. Mach Disk in Underexpanded Exhaust Plumes. Technical report, AIAA Journal, 1971.

[29] E. Brewer and C. Craven. Base Flow Field at High Altitude for Four-Engine Clustered Nozzle Configuration . Technical report, NASA, 1969.

[30] N. Musial and J. Ward. Base Flow Characteristics for Several Four-Clustered Rocket Configurations at Mach Numbers from 2.0 to 3.5. Technical report, NASA, 1961.

[31] T. Wang. Grid-Resolved Analysis of Base Flowfield for Four-Engine Clustered Nozzle Configuration. *Journal of Spacecraft and Rockets*, 33(1):22–29, Januar - Feburary 1996.

[32] R. Nallasamy , M. Kandula , L. Duncil and P. Schallhorn. Numerical Simulation of the Base Flow and Heat Transfer Characteristics of a Four-Nozzle Clustered Rocket Engine. *AIAA*, 2008.

[33] How does the Falcon 9 first stage avoid burning up on re-entry? `https://space.stackexchange.com/questions/13935/how-does-the-falcon-9-first-stage-avoid-burning-up-on-re-entry`, 2017. Accessed on 12-October-2017.

[34] H. Ebrahimi , J. Levine , A. Kawasaki and P. Schallhorn. Numerical Investigation of Twin-Nozzle Rocket Plume Phenomenology. *Journal of Spacecraft and Rockets*, 16(2):178–186, March - April 2000.

[35] F. Alvi, J. Ladd and W. Bower. Experimental and Computational Investigation of Supersonic Impinging Jets. *AIAA*, 40(4), April 2002.

[36] J. Inman, P. Danehy, R. Nowak, and D. Alderfer. The Effect of Impingement on Transitional Behavior in Underexpanded Jets. In *47*$^{\text{th}}$ *AIAA Aerospace Sciences Meeting and Exhibit*, 2009.

[37] M. Mehta, A. Sengupta, M. Pokora, L. Hall and N. Rennó. Mars Landing Engine Plume Impingement Ground Interaction. In *12*$^{\text{th}}$ *Event International Conference on Engineering, Science, Construction, and Operations in Challenging Environments - Earth and Space 2010*, pages 143–157, March 2010.

[38] A. Morris, D. Goldstein, P. Varghese and L. Trafton. Modeling the Interaction between a Rocket Plume, Scoured Regolith, and a Plume Deflection Fence. In *Earth and Space*, 2012.

[39] W. Hill and R. Jenkins. Ground Jet Impingement of a Fan Jet Exhaust Plume. Technical report, Grumman Aerospace Corporation, 1978.

[40] R. Jenkins and W. Hill. Investigation of VTOL Upwash Flows Formed by Two Impinging Jets. Technical report, Grumman Aerospace Corporation, 1977.

[41] C. Cordell. *Computational Fluid Dynamics and Analytical Modeling of Supersonic Retropropulsion Flowfield Structures across a Wide Range of Potential Vehicle Configurations*. PhD thesis, Georgia Institute of Technology, 2013.

[42] S. Berry , M. Rhode , K. Edquist and C. Player. Supersonic Retropropulsion Experimental Results from the NASA Langley Unitary Plan Wind Tunnel. In *42*nd *AIAA Thermophysics Conference*, 2011.

[43] S. Berry , M. Rhode and K. Edquist. Supersonic Retropropulsion Experimental Results from NASA Ames 9x7 Foot Supersonic Wind Tunnel. *Journal of Spacecraft and Rockets*, 51(3):724–734, May - June 2014.

[44] S. Gilles and J. Kallis. Penetration Distance of Retrorocket Exhaust Plumes Into an Oncoming Stream. Technical report, Aerospace Corporation, 1964.

[45] D. Schauerhamer, K. Trumble, B. Kleb, J. Carlson and K. Edquist. Continuing Validation of Computational Fluid Dynamics for Supersonic Retropropulsion. In *50*th *AIAA Aerospace Sciences Meeting*, 2012.

[46] K. Edquist, A. Korzun, K. Bibb, D. Schauerhamer and E. Ma, P. McCloud, G. Palmer and J. Monk. Comparison of Navier-Stokes Flow Solvers to Falcon 9 Supersonic Retropropulsion Flight Data. In *AIAA SPACE and Astronautics Forum and Exposition*, September 2017.

[47] J. Stalder and M. Inouye. A Method of Reducing Heat Transfer to Blunt Bodies by Air Injection. Technical report, NASA, 1956.

[48] L. Roberts. Mass Transfer Cooling Near The Stagnation Point. Technical report, NASA, 1959.

[49] G. Cheng, K. Neroorkar, Y. Chen, T. Wang and E. Daso. Numerical Study of Flow Augmented Thermal Management for Entry and Re-Entry Environments. In *39*th *AIAA Thermophysics Conference*, 2007.

[50] C. Chang, B. Venkatachari and G. Cheng. Effect of Counterflow Jet on a Supersonic Reentry Capsule. In *42*nd *AIAA/ASME/SAE/ASEE Joint Propulsion Conference and Exhibit*, 2006.

[51] K. Hayashi, S. Aso and Y. Tani. Numerical Study on Aerodynamic Heating Reduction by Opposing Jet. Memoirs of the Faculty of Engineering, Kyushu University, 2006.

[52] E. Krämer. Strömungslehre 1. Lecture Notes to "Strömungslehre 1", Bachelor of Science Aerospace Engineering at the University of Stuttgart, 2012.

[53] G. Lamanna and S. Winkler. Convective Heat Transfer - The Basic with Selected Examples. Lecture Notes to "Selected Problems of Convective Heat Transfer", Master of Science Aerospace Engineering at the University of Stuttgart.

[54] D. Wilcox. *Turbulence Modeling for CFD.* DCW Industries. Inc, 2006.

[55] S. Gordon and B. McBride. Computer Program for Calculation of Complex Chemical Equilibrium Compositions and Applications. Technical report, NASA Reference Publication 1311, 1996.

[56] Institute for Space Systems, University of Stuttgart. Aerothermodynamik. Lecture Notes to "Aerothermodynamik", Master of Science Aerospace Engineering at the University of Stuttgart, 2014.

[57] P. Spalart and S. Allmaras. A One-Equation Turbulence Model for Aerodynamic Flows. *La Recherce Aerospatial*, (1):5–21, 1994.

[58] F. R. Menter. Two-Equation Eddy-Viscosity Turbulence Models for Engineering Applications. *AIAA*, August 1994.

[59] H. Versteeg and W. Malalasekera. *An Introduction to Computational Fluid Dynamics - The Finite Volume Method.* Pearson Education Limited, 2007.

[60] Insitute for Aerospace Thermodynamics, University of Stuttgart. Fundamentals of Turbulence Modelling. Lecture notes to "Fundamentals of Turbulence Modeling", Master of Science Aerospace Engineering at the University of Stuttgart, 2016.

[61] C-D. Munz and T. Westermann. *Numerische Behandlung gewöhnlicher und partieller Differenzialgleichungen.* Springer, 3^{rd} edition, 2012.

[62] S. Karl. *Numerical Investigation of a Generic Scramjet Configuration.* PhD thesis, Fakultät Maschinenwesen, Technischen Universität Dresden, 2011.

[63] *TAU-Code User Guide*, 2013.

[64] S. Karl, D. Potter, M. Lamber and K. Hannemann. Computational Analysis of Radiative Heat Loading on Hypervelocity Reentry Vehicles. *Journal of Spacecraft and Rockets*, 52(1):63–75, 2015.

[65] V. Dippold. Seiner Nozzle with Mach 2.0, Heated Jet Flow. `https://www.grc.nasa.gov/WWW/wind/valid/seiner/Seiner.html`, 2012. Accessed on 05-July-2017.

[66] D. Yoder, N. Georgiadis and M. O'Gara. Frozen Chemistry Effects on Nozzle Performance Simulations. In *38^{th} Fluid Dynmamics Conference and Exhibit*, June 2008.

[67] T. Wang. Multidimnesional Unstructured-Grid Liquid Rocket-Engine Nozzle Performance and Heat Transfer Analysis. *Journal of Propuslion and Power*, 22(1): 78–84, January-February 2006.

[68] T. Ecker. Oral information on DLR TAU convergence and sharp edge modeling. 2017.

[69] S. Karl. Oral information on DLR TAU convergence. 2017.

[70] Cantera. `http://cantera.org/docs/sphinx/html/index.html`. Accessed on 2-January-2018.

[71] Engineeringtoolbox. Emissivity Coefficients of some common Materials. `https://www.engineeringtoolbox.com/emissivity-coefficients-d_447.html`, 2017. Accessed on 17-November-2017.

[72] V. Hannemann. Oral information on boundary conditions, grids and RANS for unsteady flowfields. 2017.

[73] T. Ecker. Internal studies on gas modeling in nozzle flows. 2017.

[74] F. Incropera, D. DeWitt and A. Lavine. *Fundamentals of Heat and Mass Transfer*. John Wiley & Sons, 6th edition, 2006.

[75] S. Karl. RLV: Aerodynamische Datenbank: CFD. DLR internal study, 2017.

[76] Engineeringtoolbox. Thermal Conductivity of common Materials and Gases. `https://www.engineeringtoolbox.com/thermal-conductivity-d_429.html`, 2017. Accessed on 17-November-2017.

Appendix A

Knudsen Number

The Knudsen number Kn describes the ratio of the mean free path, that a gas particle travels between two collisions λ, to the characteristic flowfield length D [16]:

$$Kn = \frac{\lambda}{D} \tag{A.1}$$

According to the Knudsen number the following flow regimes are discerned [16]:

- $Kn \leq 0.01$ continuous regime
- $0.01 < Kn \leq 0.1$ slip flow regime
- $0.1 < Kn \leq 10$ transitional regime
- $Kn > 10$ free molecular flow regime

.

The Navier-Stokes equations are only applicable in the continuous regime. To verify, whether the first stage SRP simulations are still in the continuous regime, the Knudsen number at the beginning of the retro-propulsion maneuver is calculated. The mean free path λ of air molecules at the altitude of $h = 70$ km is $\lambda = 9.285 \cdot 10^{-4}$ [16]. The first stage diameter, $D = 6.4$ m, is chosen as the characteristic flowfield length D. For the Knudsen number at this altitude follows

$$Kn = \frac{\lambda}{D} = 1,45 \cdot 10^{-4} \tag{A.2}$$

and thus smaller than 0.01. Therefore the air flow around the first stage can still be assumed as continuum.

Plume flows up to diameters of 1 km are still considered to be in the continuous regime [25]. The exhausting plume from the first stage only stretches up to over a 100 m at the beginning of the retro-propulsion maneuver ($h = 69$ km) and can therefore also be considered in the continuous regime.

Appendix B

Sample Calculation of Biot Number for Lumped Mass Model

The Biot number characterizes the ratio of heat conduction resistances inside a body to the resistance of heat transfer at the body surface. It indicates whether the temperatures inside a body will vary significantly in space, while the body heats over time from a thermal gradient applied to its surface [74].

$$Bi = \frac{h\, b_{\text{element}}}{k_{\text{alu}}} \tag{B.1}$$

h refers to the convective heat transfer coefficient, b_{element} the characteristic length of a surface element for the heat transfer and k_{alu} to the thermal conductivity of aluminum [76].

The heat transfer coefficient h is calculated from the convective heat transfer $\dot{q}_{\text{conv}}$ and the temperature difference between the vehicle's surface temperature and the temperature at the boundary layer edge. Trajectory point 7 with $T_{\text{w}} = 400$ K was chosen for the calculation. The temperature difference between the gas temperature 5 mm away from the baseplate and the baseplate at the chosen point (0 m, 1.98 m, 0.8 m) was $\Delta T = 1062 - 400 = 662$ K. With the heat flux of $\dot{q} = 12.525$ kW at this point, the heat transfer coefficient yields $h = \dot{q}/\Delta T = 18.9$ W/(K m^2).

The baseplate case with 5 mm wall thickness consists of the highest wall thickness investigated in this thesis. Therefore, the Biot number with $k_{\text{alu}} = 215$ W/(K m) [76] and b_{element} yields

$$Bi = \frac{h\, b_{\text{element}}}{k_{\text{alu}}} = 4.4 \cdot 10^{-4} \tag{B.2}$$

Thus, the baseplate and sidewall meet the requirements of $Bi < 0.1$ for the lumped mass model.

Appendix C

Baseplate Temperature Distributions

The evolution of the baseplate temperature over the trajectory for different thicknesses 1.8 and 5 mm (figure C.2) are presented, as well as the comparison of baseplate temperature evolution of configurations A and B.

C.1 Temperature Evolution

The baseplate temperature distributions along the retro-propulsion trajectory for wall thicknesses 1.8 (figure C.1) and 5 mm (figure C.2) are visualized below.

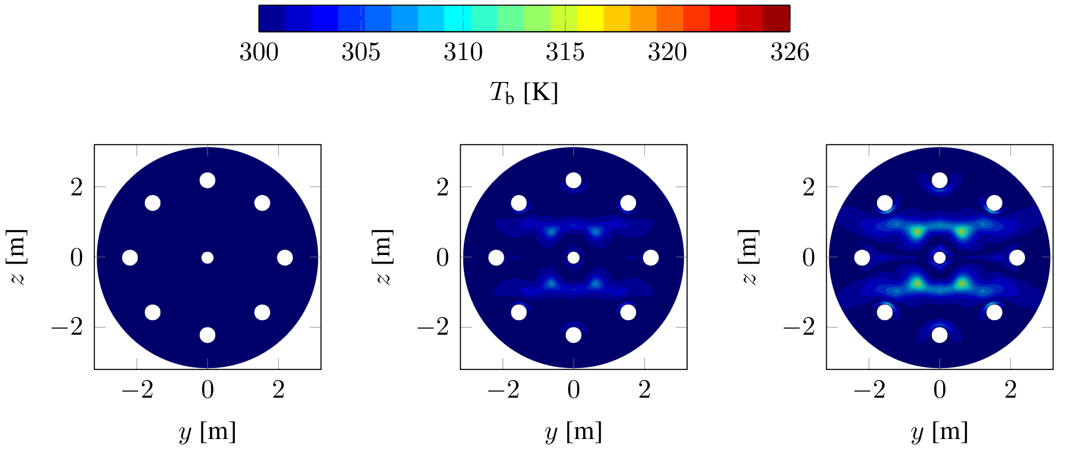

(a) Trajectory point 1 **(b)** Trajectory point 2. **(c)** Trajectory point 3

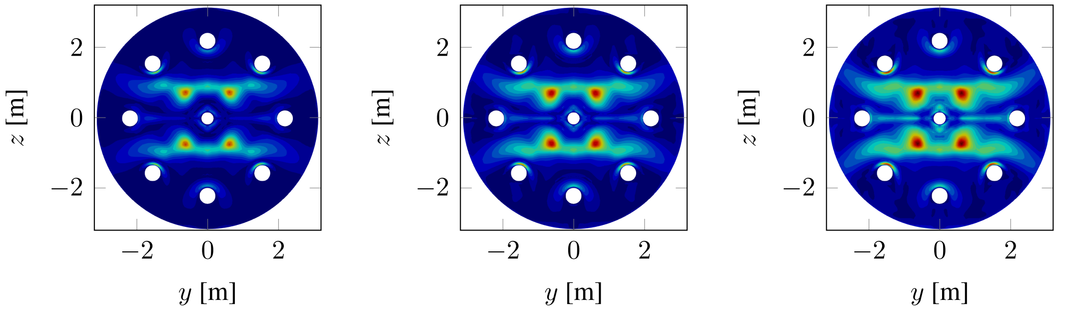

(d) Trajectory point 4. **(e)** Trajectory point 5 **(f)** Trajectory point 6.

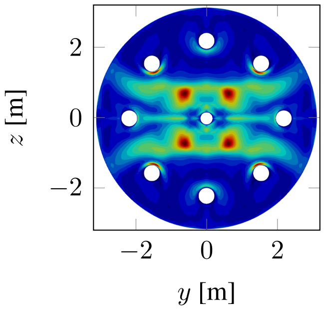

(g) Trajectory point 7

Figure C.1. Baseplate temperature evolution for baseplate thickness of 1.8 mm along SRP trajectory, active engines along z centerline.

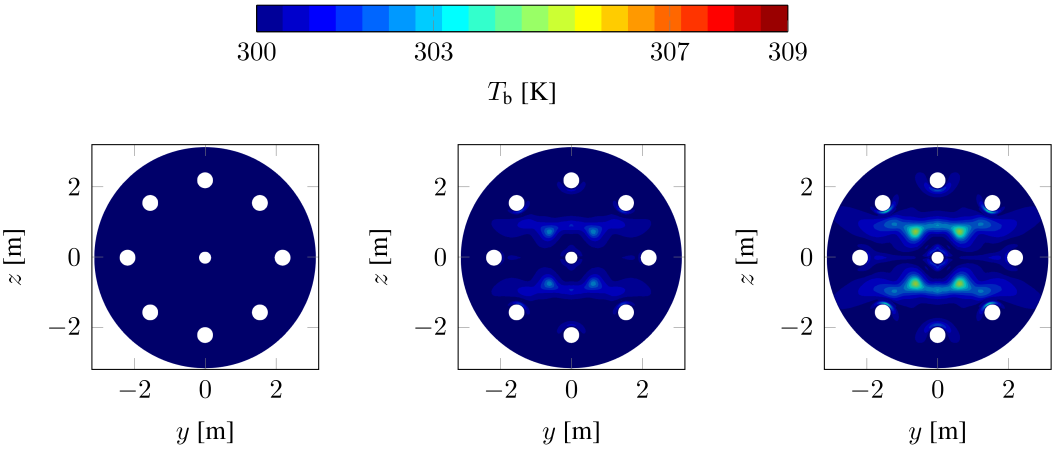

(a) Trajectory point 1 **(b)** Trajectory point 2. **(c)** Trajectory point 3

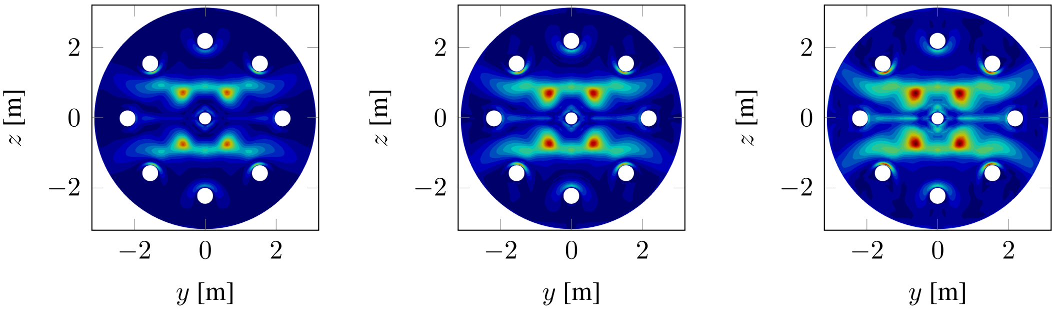

(d) Trajectory point 4. **(e)** Trajectory point 5 **(f)** Trajectory point 6.

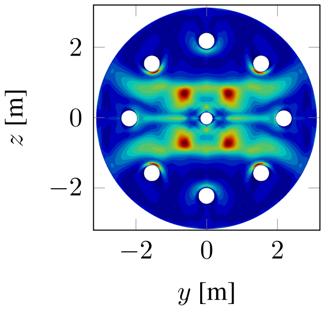

(g) Trajectory point 7

Figure C.2. Baseplate temperature evolution for baseplate thickness of 5 mm along SRP trajectory, active engines along z centerline.

C.2 Comparison of A and B

The comparison of A and B for thickness 1.8 mm is shown in figure C.3 and for 5 mm in figure C.4.

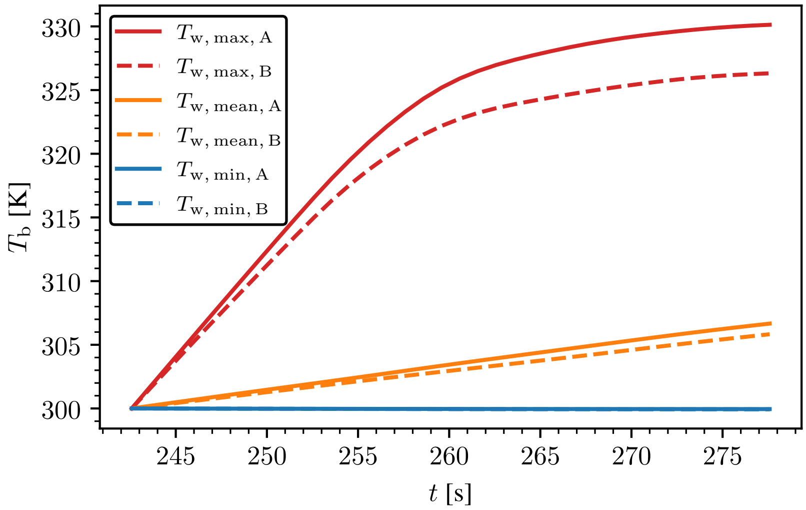

Figure C.3. Influence of combustion chamber temperature on baseplate temperature evolution for $b = 1.8$ mm.

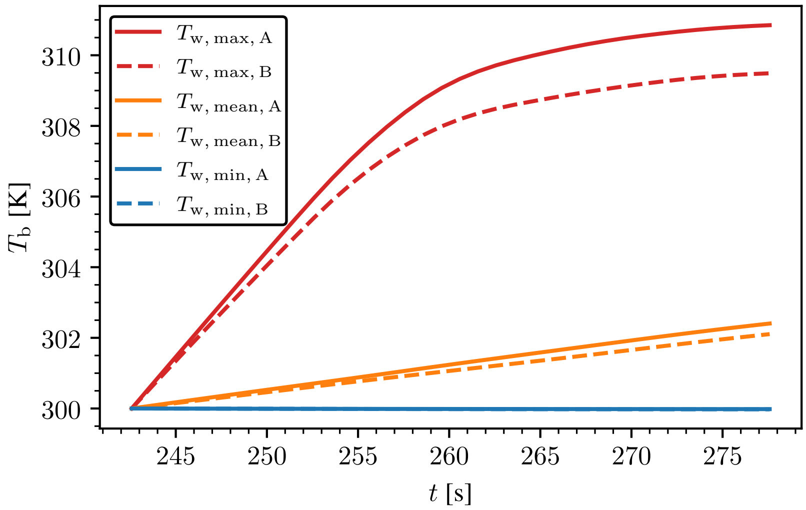

Figure C.4. Influence of combustion chamber temperature on baseplate temperature evolution for $b = 5$ mm.

Appendix D

Heat Flow Rate to Baseplate over SRP Trajectory

The rate of heat flow follows the linear trend "better" than configuration B.

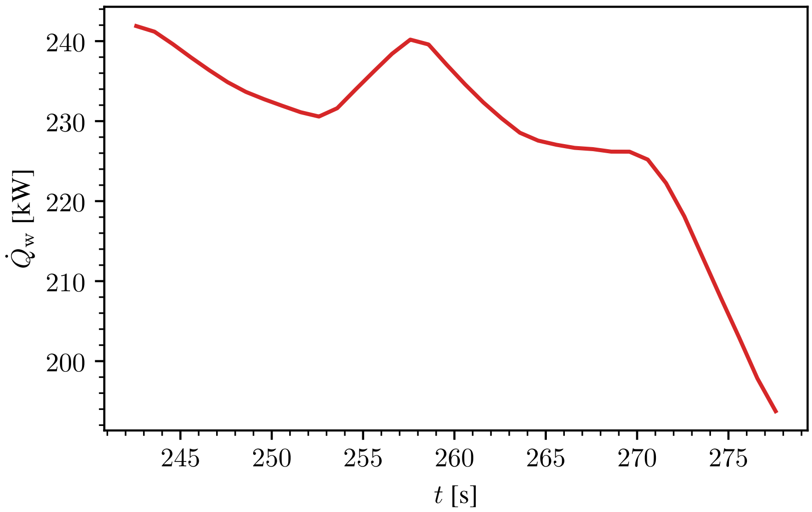

Figure D.1. Rate of heat flow to baseplate along SRP trajectory for configuration A.